1-1-2012

Gapped cantilever for the enhancement of strain sensitivity and energy efficiency

Qinglong Zheng
Wayne State University,

GAPPED CANTILEVER FOR THE ENHANCEMENT OF STRAIN SENSITIVITY AND ENERGY EFFICIENCY

by

QINGLONG ZHENG

DISSERTATON

Submitted to the Graduate School

of Wayne State University,

Detroit, Michigan

in partial fulfillment of the requirements

for the degree of

DOCTOR OF PHILOSOPHY

2012

MAJOR: ELECTRICAL ENGINEERING

Approved By:

_____
Advisor   Date

_____

_____

_____

_____

ACKNOWLEDGEMENT

First of all, I would like to express my deeply-felt thanks to my advisor Prof. Yong Xu for his thoughtful guidance, warm encouragement and enormous help during my PhD study. Especially, I owe him a heartfelt appreciation for not giving me up and keeping supporting me during the hardest time in my life until the end of the program. I could not imagine having a better advisor and mentor for my Ph.D. study.

I would also like to express my sincere gratitude to other members of the dissertation committee, Prof. Mark Cheng, Prof. Amar Basu and Prof. Wen Li for their support, guidance and helpful suggestions.

I would like to gratefully acknowledge my fellow lab mates Dr. Zhuo Wang for leading me into the field and teaching me analytical model derivation and finite element simulation; Dr. Yuefa Li for guiding and helping me during all of the micro fabrication process; Hong'en Tu for the help in developing and testing of meso-scale vibration energy harvester and resonant mass sensor; Yating Hu for the characterization of piezoresistive accelerometer; and Jessin John for aid in micro fabrication.

I am forever indebted to my parents Bingguo Zheng/Baoyu Liu and my wife Yan Fang for their understanding, endless patience and encouragement when it was most required. My special thanks also go to my cousin Lin Li and his wife Ling Zhu for looking after me for the last several months to overcome the most difficult period in my life.

Finally, I thank the national science foundation for their generous support and the SSIM cleanroom at Wayne State University for providing the facility for micro fabrication.

TABLE OF CONTENTS

LIST OF TABLES

LIST OF FIGURES

xii

CHAPTER I. INTRODUCTION

1.1 Motivation

Cantilever structures have been widely used in numerous applications in Micro-Electro-Mechanical Systems (MEMS) due to its simplicity. MEMS is a technology that can generally be defined as miniaturized electro-mechanical devices which are made by microfabrication. The physical dimensions of MEMS devices can vary from well below one micron all the way to several millimeters. In the last several decades, due to the tremendous possibility of MEMS applications, many researchers have spent an extremely large amount of efforts on developing microsensors, microactuators and microsystems such as lab-on-a-chip. As a result, nowadays, a large number of MEMS products have been developed and are playing an important role in consumer, industrial, military as well as medical areas.

The basic idea of cantilever sensor is to convert input stimuli (inertial, temperature, pressure, chemical etc.) into the bending of the cantilever and detect the amount of the bending to backtrack the magnitude of the input. Piezoresistive, piezoelectric and optical detections are the major approaches to measure the bending of the cantilever. Comparing with optical method, piezoresistive/piezoelectric mechanism has generally been the more popular choice due to the advantages of being low cost, small foot-print as well as having a simple structure and a simple readout circuitry[1-22]. However, compared with optical method, low strain sensitivity is recognized as a major disadvantage of piezoresistive/piezoelectric sensors, and it limits the applications of this type of sensors.

There are several approaches to address this issue. For instance, the sensitivity can be increased by selecting the proper geometric dimensions of the cantilever and proof mass.

Furthermore, the sensor performance can be improved by optimizing the piezoresistive/piezoelectric elements on the cantilever. Alternatively, the performance can be improved by employing some novel configurations. In this research, a gapped cantilever structure is proposed to potentially increase the sensitivity by orders of magnitude.
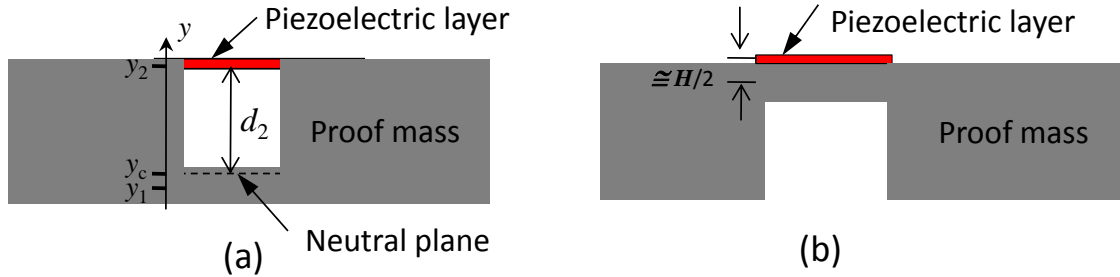
Figure.1.1 Illustraion of the comparison between asymmetric gapped cantilever and conventional cantilever. (a) piezoelectric gapped cantilever, (b) piezoelectric conventional cantilever.

For this new design, the supporting beam of the proof mass is an asymmetric gapped cantilever, consisting of a bottom mechanical layer and a top piezoelectric/piezoresistive layer separated by a gap as shown in Fig. 1.1(a). The main idea behind asymmetric gapped cantilever is that the mechanical strain experienced by the piezoelectric/piezoresistive layer, is proportional to the distance between the piezoelectric/piezoresistive layer and the neutral plane. For conventional cantilever as shown in Fig. 1.1(b), this distance is approximately half of the cantilever thickness, e.g., 20 μm. For the asymmetric gapped cantilever, this distance is about the gap height, which is very close to the wafer thickness, e.g., 500 μm. Therefore, the strain sensitivity is significantly higher.

Furthermore, it is worth noting that the new design allows the majority of the bending energy to be used to strain the sensing layer. But for the conventional cantilever, a large percentage of the energy is wasted to strain the non-active layer because the thickness of the

piezoelectric/piezoresistive layer is only a small portion of the total cantilever thickness. For example, a conventional Aluminum Nitride (AlN) cantilever such as the one reported in [23], with a 45 μm thick cantilever and 0.4 μm think AlN, has only ~5% of the vibration energy allocated to AlN. In comparison, the design based on asymmetric gapped cantilevers can concentrate more than 80% of bending energy to the sensing layer as shown in later chapters. Therefore, from energy point of view, the asymmetric gapped cantilever is a much more efficient design. Due to the enhanced energy efficiency, gapped cantilever structure has a great potential in the applications of energy harvesting as well.

1.2 Objective

Although there have been some previous study presented similar structure by other researchers [24-29], the potential of this structure has not been fully realized due to the lack of a comprehensive study. Actually the performance can even be degraded if not properly designed. Therefore, it is necessary to have systematical study to fully dig out the potential of gapped cantilever. The main objectives of this work are:

1. To develop an advanced theoretical model for gapped cantilever in order to guide the design of gapped cantilever based sensor and energy harvester.

2. To verify the analytical model using finite element simulation.

3. To optimize the design of gapped cantilever transducer using the analytical model that developed in this work.

4. To implement the gapped cantilever structure for several different applications, which include but are not limited to

1) Piezoresistive accelerometer.

2) Vibration energy harvester.

3) Resonant mass sensor.

1.3 Thesis Organization

In chapter 2, the development of the analytical model for gapped cantilever will be presented. Optimization of the design from energy point of view will also be discussed in chapter 2. In chapter 3, finite element simulation will be introduced and utilized to verify the analytical model developed in chapter 2. In the following chapters, three specific applications of the gapped cantilever will be presented, including piezoresistive accelerometer in chapter 4, vibration energy harvester in chapter 5 and resonant mass sensor in chapter 6. The extents of the research progress for these applications vary. For piezoresistive accelerometer in chapter 4, the design and optimization taking into account for both sensitivity and noise have been completed, and the accelerometers have been micro-fabricated and characterized. In chapter 5, vibration energy harvester targeting on powering tire pressure monitoring system has been designed, developed and tested both in the lab and on the road. In chapter 6, the design, fabrication and a preliminary characterization of both meso-scale and micro-scale resonant mass sensors will be presented. Chapter 7 will conclude with a summary of the main contributions of the dissertation and potential future work.

CHAPTER 2. ANALYTICAL MODEL

Since the models for conventional cantilevers may not be directly applied to gapped cantilever structure because of the gap between sensing layer and mechanical layer, it is necessary to develop a new model to describe the mechanical properties of the new structure, facilitating to different applications.

2.1 mechanics of material method

Mechanics of material method is a subject that is used to analyze the behavior of a material or a mechanical structure under certain loads[30]. With this method, engineers are able to theoretically calculate the reacts (deformation, strain, vibration, etc.) of certain type of structure under specific conditions (load, boundary, etc.). Once the theory and analytical model for the structure are established, one can easily use it to analyze, model and verify similar structures in any kinds of engineering applications. Therefore, mechanics of material method has long been a powerful tool for engineers and researchers in a large variety of areas, such as mechanical, civil, mining engineering, biomechanics, etc. In his section, the basics and fundamental concepts of mechanics of material theory will be presented in order to develop the analytical model for gapped cantilever.

2.1.1 Stress and strain

Stress is the ratio of applied force F and cross section A, defined as "force per unit area". The stress caused by normal force applied to the plane is denoted as normal stress, which is

$$\sigma_n = F_n / A \tag{2.1}$$

where F_n is normal force to the plane as shown in Fig. 2.1(a).

Whereas stress caused by shear force (force parallel to the plane) applied to the plane is denoted as sheer stress, which is expressed as

$$\sigma_p = F_p / A \tag{2.2}$$

where F_p is sheer force to the plane.
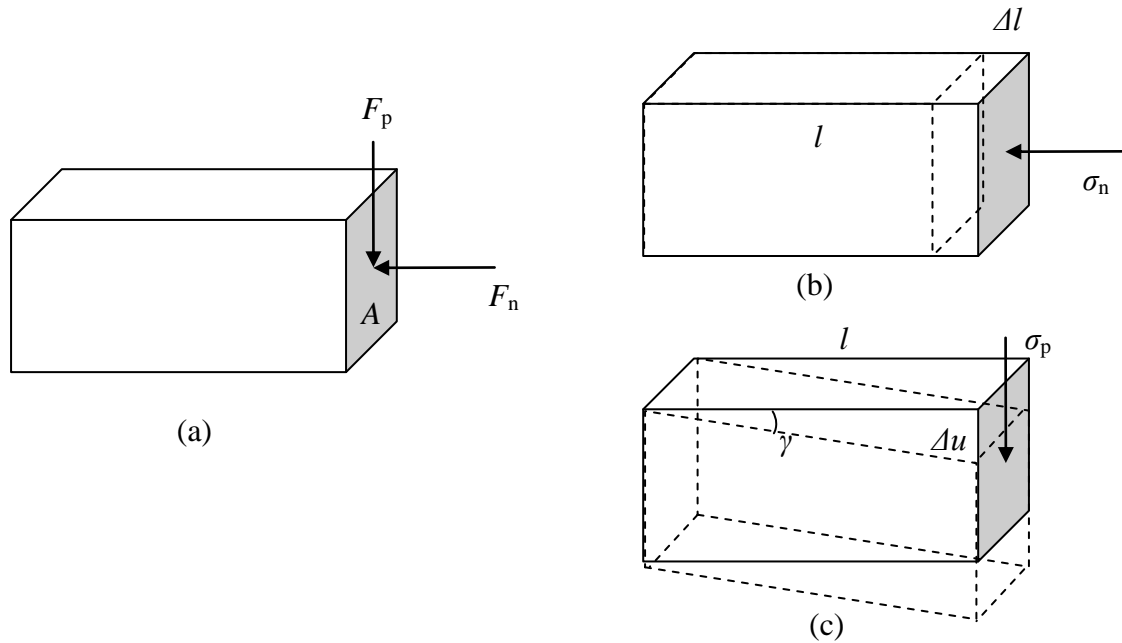
Figure 2.1 A rectangle block subject to normal and sheer forces on one of the surface plane.

Deformation of a solid due to stress can be defined using strain. Similar to the classification of normal and sheer stresses, there are normal strain and sheer strain corresponding to the two types of stresses as well. Mathematically, normal strain can be denoted as the ratio of change of length to the initial length, which is

$$\varepsilon = \Delta l / l \tag{2.3}$$

where Δl is the change of length due to normal stress, and l is the initial length as shown in Fig. 2.1(b).

Meanwhile, sheer strain is the ratio of the sheer displacement due to sheer stress to the length of the block, which is

$$\gamma = \Delta u / l \tag{2.4}$$

where Δu is sheer displacement as shown in Fig. 2.1(c). When the displacement is small enough compared to the length, sheer strain is simply equal to the sheered angle.

Most metals have deformations that are proportional with the induced loads within a range. The ratio between normal stress and normal strain is defined as Young's modulus, which is

$$E = \sigma / \varepsilon \tag{2.5}$$

2.1.2 Euler–Bernoulli beam theory

In order to understand the behavior of a cantilever subject to bending, infinitesimal imaginary cut of the cantilever will be analyzed using the well-known Euler-Bernoulli beam theory in the following.

An infinitesimal cut of the cantilever subject to bending due to a bending moment M is shown in Fig. 2.2 (a). If we assume the surface of the cutting edge remain plane after bending, the displacement in x direction of the points on the surface can be simply expressed as

$$u_x = -z\psi(x) \tag{2.6}$$

where z is the vertical axis from neutral plane, $\psi(x)$ is the bending angle of the cut plane as shown in Fig 2.2 (b).
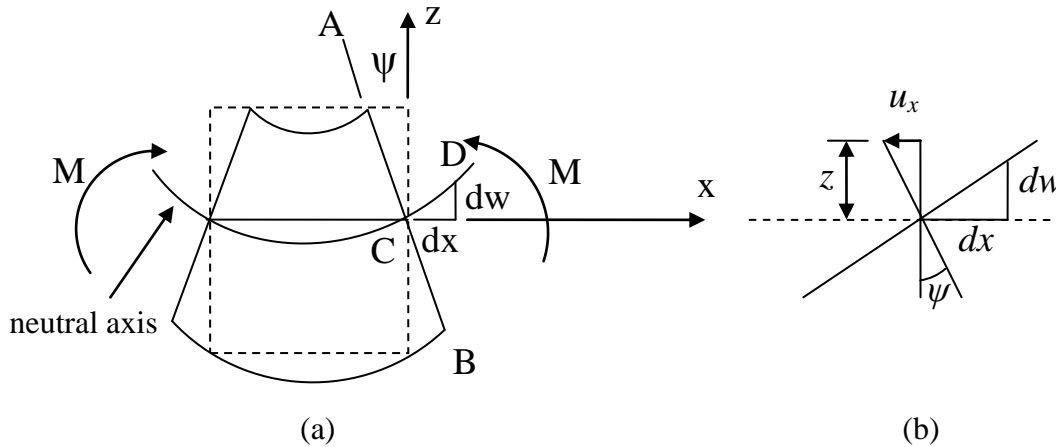
Figure 2.2. (a) Infinitesimal cut of the cantilever which is subject to bending. (b) Relation of the bending angle and the beam and displacement of the cutting plane in x direction.

If the plane AB remains perpendicular to CD, we have

$$\psi = \frac{dw}{dx} \tag{2.7}$$

where dw is the infinitesimal vertical deflection of the beam, and dx is the infinitesimal distance in x direction.

Therefore, displacement in x direction can be expressed as

$$u_x = -z\frac{dw}{dx} \tag{2.8}$$

Normal strain (strain in x direction) is the ratio of change in length to original length, which can be expressed using infinitesimal term as

$$\varepsilon_{xx} = \frac{\partial u_x}{\partial x} \tag{2.9}$$

Combining Eqs. (2.8) and (2.9), we have

$$\varepsilon_{xx} = \frac{\partial u_x}{\partial x} = -z \frac{d^2 w}{dx^2} \tag{2.10}$$

Therefore the normal stress is

$$\sigma_{xx} = -Ez \frac{d^2 w}{dx^2} \tag{2.11}$$
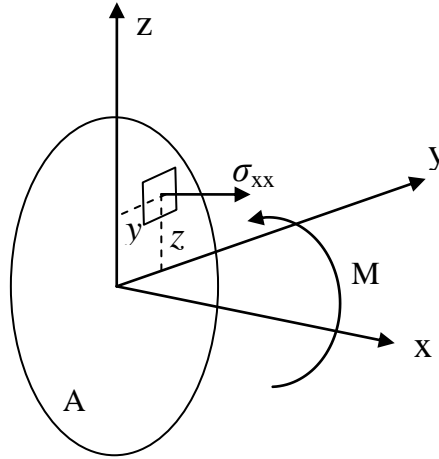
Figure 2.3. illustration of normal stress and bending moment on the imaginary cutting surface of the beam.

Because the bending moment on the cutting surface can be calculated as the integral of bending monent caused by normal stress over the cross-sectional area as illustrated in Fig. 2.3, we have

$$M = -\int_A \sigma_{xx} z \, dA = E \frac{d^2 w}{dx^2} \int_A z^2 \, dA = EI \frac{d^2 w}{dx^2} \tag{2.12}$$

where *I* is the second moment of area.

Combining Eqs. (2.11) and (2.12), the normal stress can be simplified to

$$\sigma_{xx} = -\frac{Mz}{I} \tag{2.13}$$

Noting that the first derivative of bending monent over x axis is sheer force, we have

$$\frac{dM}{dx} = V(x) \tag{2.14}$$

In addition the first derivative of sheer force is distributed force which is force per unit length.

$$\frac{dV}{dx} = q_z(x) \tag{2.15}$$

Therefore, from Eqs. (2.13), (2.14) and (2.15), we can derive

$$EI\frac{d^4w}{dx^4} = q_z(x) \tag{2.16}$$

This equation is called Euler-Bernoulli equation [30].

2.1.3.beding of cantilever

Let's consider a cantilever with one end fixed and the other end subject to a vertical force as shown in Fig. 2.4.
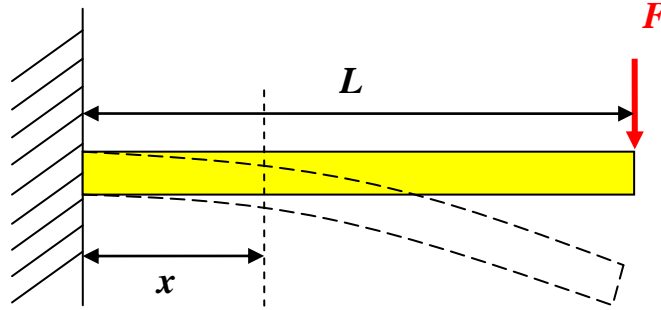
Figure 2.4. Bending of a conventional cantilever with one end fixed and the other end free.

At position x, the bending moment is

$$M(x) = F(L-x) \qquad (2.17)$$

Based on eq. (2.12), we have

$$\frac{d^2 w(x)}{dx^2} = \frac{M(x)}{EI} = \frac{F(L-x)}{EI} \qquad (2.18)$$

Integrating it over the length from 0 to x, the slope of the cantilever at position x can be calculated, which is

$$\frac{dw(x)}{dx} = \int_0^x \frac{F(L-s)}{EI} = \frac{F(Lx-x^2/2)}{EI} \text{ (Boundary condition } \frac{dw(0)}{dx} = 0 \text{)} \qquad (2.19)$$

Integrating the slope over the length from 0 to x once again, the vertical deflection of the cantilever at position x can be calculated, which is

$$w(x) = \int_0^x \frac{F(Lx-x^2/2)}{EI} = \frac{F(Lx^2/2-x^3/6)}{EI} \text{ (Boundary condition } w(0) = 0 \text{)} \qquad (2.20)$$

Therefore, by substituting $x=L$ into Eqs.(2.19) and (2.20), we can calculate the slope and vertical deflection of the cantilever at the free end, which are

$$\frac{dw(L)}{dx} = \frac{FL^2}{2EI} \qquad (2.21)$$

$$w(L) = \frac{FL^3}{3EI} \qquad (2.22)$$

So far, the fundamental concepts of mechanics of material method and basic equations have been presented, which are necessary for developing the theoretical model for gapped cantilever structure.

2.2 Gapped cantilever structure

Figure 2.5 schematically shows a general form of an asymmetric gapped cantilever, which is far more advantageous than conventional cantilever for sensing applications. This structure includes a base, a proof mass, a bottom mechanical beam and a top sensing beam, and two wider rigid beams which connect top sensing beam to the base and the proof mass respectively. Note that the supporting beam of the proof mass is a composite cantilever, consisting of a bottom mechanical layer and a top sensing layer separated by a gap, namely gapped-cantilever.
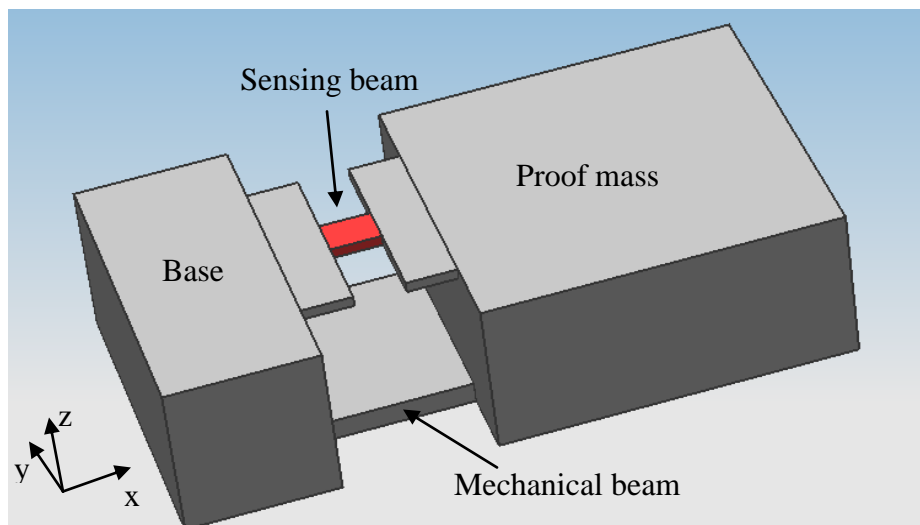
Figure 2.5. Schematic structure of an asymmetric gapped cantilever. The structure includes a base, a proof mass, a bottom mechanical beam and a top sensing beam, and two wider beams connecting top sensing beam to base and proof mass respectively.

The symbols for dimensions of the structure are listed in Table 2.1. It's also important to note that we assume that 1) the deformation of the proof mass is neglected; 2) mass of the beams are neglected; 3) deflection is small; in the following derivations.

Table 2.1 Symbols for dimensions of the bottom mechanical beam, top sensing beam and proof mass.

	Length (x)	Width (y)	Thickness (z)
Bottom mechanical beam	l_1	w_1	t_1
Top sensing beam	l_2	w_2	t_2
Proof mass	l_m	w_m	t_m

2.3 Force and bending moment equilibriums

When a force is applied to the proof mass in z direction, the cantilever beams are subject to deformation resulting in a displacement and rotation of the proof mass. If we assume an imaginary cut between cantilever beams and proof mass, there will be several forces and bending moments applied to each of the separated parts as shown in Fig. 2.6.
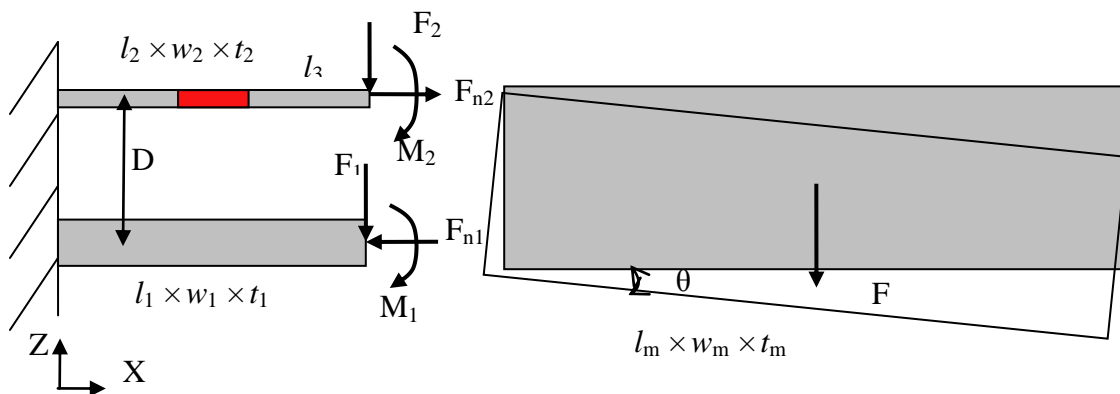
Figure 2.6. Forces and bending moments applied to the cantilever in a discrete component model. F_{n1}, F_{n2}, F_1, F_2, M_1 and M_2 are normal forces, shear forces and bending moments on bottom and top beams respectively, F is the total force applied on proof mass, and D is the distance between top and bottom beams.

Based on force and bending moment equilibriums, the following equations can be derived:

Force balance in x-axis: $F_{n1} - F_{n2} = 0$ (2.23)

Force balance in z-axis: $F_1 + F_2 - F = 0$ (2.24)

Bending moment balance by y-axis: $M_1 + M_2 + F_{n1}\dfrac{D}{2} + F_{n2}\dfrac{D}{2} - F\dfrac{l_{pm}}{2} = 0$ (2.25)

where F_{n1}, F_{n2}, F_1, F_2, M_1 and M_2 are normal forces shear forces and bending moments on bottom and top beams respectively, F is the total force applied on proof mass, and D is the distance between the two middle planes of the top and bottom beams.

If we assume the proof mass is rigid, the following conditions need to be satisfied at the free ends of the two beams:

$$\theta_1 = \theta_2$$ (2.26)

$$\Delta z_1 = \Delta z_2$$ (2.27)

where θ_1, θ_2, Δz_1 and Δz_2 are the bending angle and displacement in z direction of bottom and top beams at the free ends, respectively.

2.4 Two bending shapes

For a conventional cantilever, we usually assume that the transverse section of the beam remain plane after bending according to plain assumption[30]. Then the deformation and strain

experienced by the cantilever can be obtained based on the well-known classical beam theory. However, for the gapped cantilever, the plane assumption is not necessarily valid. In practice, we usually observe two deformation shapes of the gapped cantilever. The first shape is the rotational bending of the composite gapped cantilever as shown in Fig. 2.7(a). The second one is translational bending as shown in Fig. 2.7(b). In fact, the true bending of the gapped cantilever is a linear sum of these two shapes. Which shape will the bending close to mainly depends on the geometric parameters [21, 22].

| (a) | (b) |
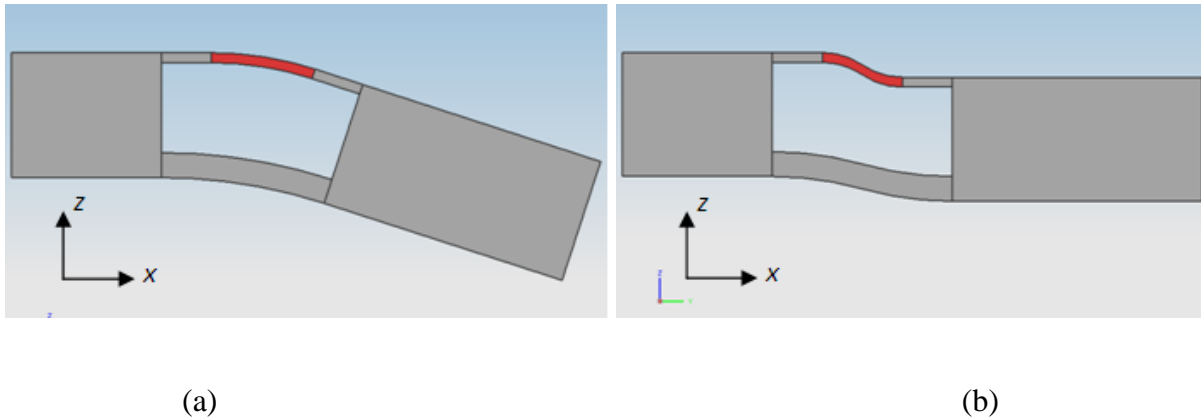
Figure 2.7. Side view of the two bending shapes of the gapped cantilever: (a) rotational bending; (b) translational bending.

2.5 Derivations

2.5.1 Decomposition of force and bending moment

If zero damping is assumed, the system can be treated as linear. Therefore, the forces and bending moments can also be decomposed into two sets corresponding to the two bending shapes respectively. For rotational bending, there should be a bending moment along with a normal force applied on each of the bottom and top beams as shown in Fig. 2.8 (a). On the other hand, for translational bending, each beam is experienced by a shear force and a bending

moment as shown in Fig. 2.8 (b). Note that for the following derivation, subscripts T and R are

used to distinguish parameters for translational bending and rotational bending respectively.
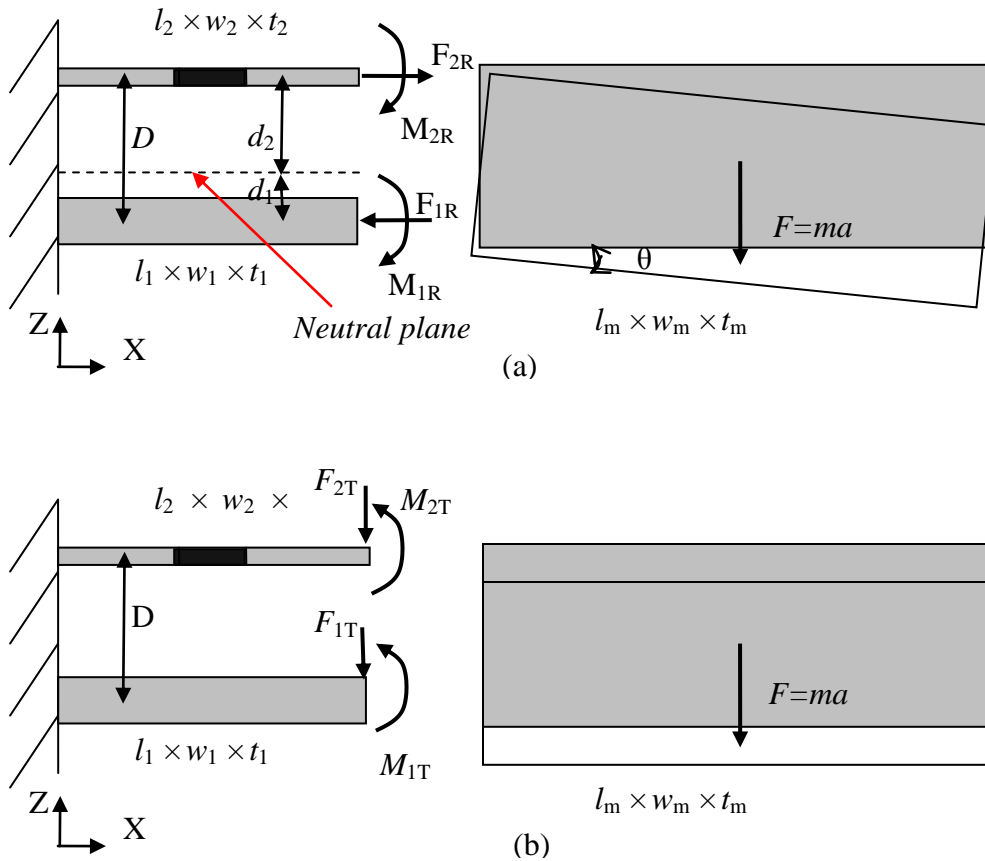
Figure 2.8. (a) Force and bending moment distribution for rotational bending. F_{1R}, F_{2R}, M_{1R}, M_{2R}, d_1 and d_2 are normal forces, bending moments and distance to neutral plane for bottom and top beams, respectively. Note that there are no shear forces in this bending mode. (b) Force and bending moment distribution for translational bending. F_{1T}, F_{2T}, M_{1T} and M_{2T} are shear forces and bending moments for bottom and top beams, respectively. Note that there are no normal forces in this bending mode.

2.5.2 Equations for rotational bending

For rotational bending, the bending angle of the proof mass is equal to the slope at the

free end of the bottom and top beams and therefore can be expressed as:

$$\theta = \frac{M_{1R}l_1}{E_1 I_1} \tag{2.28}$$

$$\theta = \frac{M_{2R}l_2}{E_2 I_2} \tag{2.29}$$

where I_1 and I_2 are moments of inertia of bottom and top beams respectively.

The displacements in x-axis of the bottom and top beams at the free end can be expressed as:

$$\Delta x_1 = \frac{F_{1R}l_1}{E_1 A_1} \tag{2.30}$$

$$\Delta x_2 = \frac{F_{2R}l_2}{E_2 A_2} \tag{2.31}$$

where $A_1 = w_1 t_1$ and $A_2 = w_2 t_2$ are cross sectional area of bottom and top beams respectively.

Since the neutral plane has zero x-displacement in rotational bending shape, the bending angle can be calculated with respect to either bottom or top beams (under small displacement assumption) as:

$$\theta = \frac{\Delta x_1}{d_1} = \frac{F_{1R}l_1}{E_1 A_1 d_1} \tag{2.32}$$

$$\theta = \frac{\Delta x_2}{d_2} = \frac{F_{2R}l_2}{E_2 A_2 d_2} \tag{2.33}$$

The total bending moments applied to the whole gapped cantilever is

$$M_R = M_{1R} + M_{2R} + F_{1R}d_1 + F_{2R}d_2 \tag{2.34}$$

By substituting F_{1R}, F_{2R}, M_{1R}, M_{2R} derived from Eqs. (2.28), (2.29), (2.32) and (2.33) into Eq. (2.34), the bending angle can be calculated and expressed by the following equation:

$$\theta = \frac{M_R l_1}{E_1 I_1 + E_2 I_2 l_1 / l_2 + E_1 A_1 d_1^{\,2} + E_2 A_2 d_2^{\,2} l_1 / l_2} \tag{2.35}$$

Define an equivalent bending rigidity for rotational bending R_R as

$$R_R = E_1 I_1 + E_2 I_2 l_1 / l_2 + E_1 A_1 d_1^{\,2} + E_2 A_2 d_2^{\,2} l_1 / l_2 \tag{2.36}$$

Then, the bending angle can be simplified to

$$\theta = \frac{M_R l_1}{R_R} \tag{2.37}$$

Using the equivalent bending rigidity, it is straightforward to calculate the z-displacement of the proof mass (center) for rotational bending as well:

$$\Delta z_R = \Delta z_{R0} + \theta \frac{l_m}{2} = \frac{M_R l_1^{\,2}}{2R_R} + \frac{M_R l_1}{R_R} \frac{l_m}{2} = \frac{M_R l_1 (l_1 + l_m)}{2R_R} \tag{2.38}$$

where z_{R0} is z-displacement of the beams at the free ends.

It is interesting to note that the total bending moment is

$$M = M_R + M_T = \frac{F l_m}{2} \tag{2.39}$$

In addition, the bending moment for Translational bending can be easily derived based on the relationship to the total shear force in this mode, and that is

$$M_T = -\frac{Fl_1}{2} \tag{2.40}$$

Therefore, the bending moment for rotational bending mode is

$$M_R = M - M_T = \frac{F(l_1 + l_m)}{2} \tag{2.41}$$

By substituting Eq. (2.41) into Eq. (2.38), the z-displacement of the proof mass can be expressed as

$$\Delta z_R = \frac{Fl_1(l_1 + l_m)^2}{4R_R} \tag{2.42}$$

Therefore, the spring constant for rotational bending can be derived as

$$k_R = \frac{F}{\Delta z_R} = \frac{4R_R}{l_1(l_1 + l_m)^2} \tag{2.43}$$

2.5.3 Equations for translational bending

For translational bending shape, the displacement of the proof mass in z-direction is equal to the z-displacements of bottom and top beams at the free end, which can be expressed as

$$\Delta z_T = \frac{F_{1T}l_1^3}{12E_1I_1} \tag{2.44}$$

$$\Delta z_T = \frac{F_{2T}l_2^3}{12E_2I_2} \tag{2.45}$$

Since the total shear force is

$$F = F_{1T} + F_{2T} \tag{2.46}$$

Eqs. (2.44) and (2.45) together can be re-arranged as

$$\Delta z_T = \frac{F l_1^{\ 3}}{12(E_1 I_1 + E_2 I_2 l_1^{\ 3} / l_2^{\ 3})} \tag{2.47}$$

Define an equivalent bending rigidity for translational bending R_T as

$$R_T = E_1 I_1 + E_2 I_2 l_1^{\ 3} / l_2^{\ 3} \tag{2.48}$$

Then, the z-displacement for translational bending can be simplified to

$$\Delta z_T = \frac{F l_1^{\ 3}}{12 R_T} \tag{2.49}$$

Therefore, the spring constant for translational bending can be derived as

$$k_T = \frac{F}{\Delta z_T} = \frac{12 R_T}{l_1^{\ 3}} \tag{2.50}$$

2.5.4 Simplification and total spring constant

To simplify the expressions and discussion, two dimensionless parameters are introduced:

$$\alpha = \frac{l_1 + l_{\mathrm{m}}}{l_1} \tag{2.51}$$

$$\beta = \frac{R_T}{R_R} \tag{2.52}$$

Then, the spring constants for rotational bending and translational bending presented in Eqs. (2.43) and (2.50) can be simplified to

$$k_R = \frac{4 R_R}{l_1^3 \alpha^2} \tag{2.53}$$

$$k_{\mathrm{T}} = \frac{12R_{\mathrm{T}}}{l_1^{\ 3}} \tag{2.54}$$

The total equivalent spring constant can be derived as

$$k_{\mathrm{E}} = (k_{\mathrm{R}}^{\ -1} + k_{\mathrm{T}}^{\ -1})^{-1} = \frac{R_{\mathrm{T}}}{l_1^{\ 3}} \frac{12}{3\alpha^2\beta + 1} \tag{2.55}$$

2.5.5 Resonant frequency and normal strain in top sensing beam

The resonant frequency based on the concentrated mass model is

$$f_0 = \frac{1}{2\pi} \sqrt{\frac{k_{\mathrm{E}}}{m}} = \frac{1}{2\pi} \sqrt{\frac{12R_{\mathrm{T}}}{ml_1^3(3\alpha^2\beta + 1)}} \tag{2.56}$$

From Eqs. (2.33), (2.37) and (2.41), the average normal strain experienced by the top sensing beam can be derived as

$$\varepsilon_2 = \frac{\Delta x_2}{l_2} = \frac{Fl_1(l_1 + l_{\mathrm{m}})d_2}{2R_{\mathrm{R}}l_2} \tag{2.57}$$

A more accurate resonant frequency can be calculated based on Rayleigh-Ritz method [2]. As well known, the total mechanical energy, which is the sum of potential and kinetic energy, is reserved in a vibrating system if damping is neglected. Therefore, the maximum potential energy should be equal to maximum kinetic energy during each cycle of vibration. Maximum potential energy occurs when the velocity is zero, and can be easily calculated using the aforementioned spring constant equation as

$$U_{\mathrm{max}} = \frac{F^2}{2k_E} = \frac{F^2 l_1^3}{24R_T}(3\alpha^2\beta + 1) \tag{2.58}$$

Meanwhile, maximum kinetic energy (maximum velocity) occurs when displacement is zero. If a sinusoidal vibration is assumed, the maximum velocity and maximum displacement has the following relationship.

$$v(x) = \omega \Delta z(x) \qquad (2.59)$$

where ω is the radian frequency of the vibration, and $\Delta z(x)$ is the maximum z-displacement at position x.

By setting the origin at the centre of the proof mass, eq. (2.59) can be expressed as

$$v(x) = \omega(\Delta z + \theta x), \quad \frac{-l_m}{2} \le x \le \frac{l_m}{2} \qquad (2.60)$$

Where Δz is the z-displacement at the center of the proof mass, which can be calculated directly using the total spring constant eq. (2.55).

$$\Delta z = \frac{F}{k_E} \qquad (2.61)$$

Therefore, the maximum kinetic energy can be calculated as

$$T_{max} = \int_{-l_m/2}^{l_m/2} \frac{v^2(x)}{2} dm = \frac{\rho A_m \omega^2}{2} \int_{-l_m/2}^{l_m/2} (\Delta z + \theta x)^2 dx$$
$$= \omega^2 \frac{m}{288} \frac{F^2 l_1^6}{R_S^2}[(3\alpha^2 \beta + 1)^2 + 3\alpha^2 \beta^2 (\alpha - 1)^2] \qquad (2.62)$$

where $A_m = w_m t_m$ is the cross sectional area of the proof mass. By letting maximum potential energy eq. (2.58) equal to maximum kinetic energy eq. (2.62), the resonant frequency can be calculated as

$$f_0' = \frac{\omega}{2\pi} = \frac{1}{2\pi}\sqrt{\frac{R_T}{ml_1^3}\frac{12(3\alpha^2\beta+1)}{(3\alpha^2\beta+1)^2+3\alpha^2\beta^2(\alpha-1)^2}} \tag{2.63}$$

2.5 Optimization

2.5.1 Energy conversion efficiency

For any kind of applications, the universal figure of merit of gapped cantilever is energy conversion efficiency. That's because we always require as much energy as possible to be used to stretch/compress the sensing layer which is the only component that contribute to the output signal. Here we define the energy conversion efficiency η as the ratio of the energy stored by pure-stretching/compression of the top sensing layer to the total mechanical energy, which can be calculated in two steps. First, the ratio from the energy stored by rotational bending to the total energy can be easily derived from spring constant equations, and that is

$$\eta_1 = \frac{k_T}{k_R+k_T} = \frac{1}{1/3\alpha^2\beta+1} \tag{2.64}$$

Second, when the gapped cantilever is subject to rotational bending, the potential energy is distributed in bottom and top beams. For each of the beams, the energy can be further decomposed into two different forms: bending energy and normal stretching/compression energy. These energies can be calculated as [30]:

$$U_{1-bending} = \frac{M_{1R}\theta}{2} \tag{2.65}$$

$$U_{2-bending} = \frac{M_{2R}\theta}{2} \tag{2.66}$$

$$U_{1-compression} = \frac{F_{1R}\Delta x_1}{2} \tag{2.67}$$

$$U_{2-stretching} = \frac{F_{2R}\Delta x_2}{2} \tag{2.68}$$

By substituting Eqs. (2.28) ~ (2.33) into Eqs. (2.65) ~ (2.68), we can find the ratios of each form of the potential energy:

$$\begin{aligned}
U_{1-bending} &: U_{2-bending} : U_{1-compression} : U_{2-stretching} \\
= \quad E_1 I_1 &: E_2 I_2 l_1 / l_2 : \quad E_1 A_1 d_1^{\,2} \quad : E_2 A_2 d_2^{\,2} l_1 / l_2
\end{aligned} \tag{2.69}$$

It can be observed from this equation that the distribution of the energy from rotational bending can be exactly described using the four terms that compose rotational bending rigidity R_R as shown in Eq. (2.36). Therefore, the percentage of the total rotational energy stored in the top sensing beam in the form of normal stretching/compression can be expressed as

$$\eta_2 = \frac{\mu E_2 A_2 d_2^{\,2}}{R_R} = (1-\beta)(1-\gamma) \tag{2.70}$$

where $\mu = l_1/l_2$ and $\gamma = d_1/D$.

Therefore, the total energy conversion efficiency is

$$\eta = \eta_1 \eta_2 = \frac{(1-\beta)(1-\gamma)}{1/3\alpha^2 \beta + 1} \tag{2.71}$$

To find an optimized design, t_1 and D are first fixed. Then, β can be simplified to

$$\beta = \frac{R_T}{R_R} = \frac{E_1 I_1 + \mu^3 E_2 I_2}{E_1 I_1 + \mu E_2 I_2 + E_1 A_1 d_1^{\,2} + \mu E_2 A_2 d_2^{\,2}} \approx \frac{E_1 I_1}{E_1 I_1 + \mu E_2 I_2 + E_1 A_1 d_1^{\,2} + \mu E_2 A_2 d_2^{\,2}} = \frac{C}{C+\gamma} \tag{2.72}$$

where

$$C = \frac{t_1^2}{12D^2} \tag{2.73}$$

Substituting Eq. (2.73) into the energy conversion efficiency equation Eq. (2.72), we get

$$\eta = \frac{3\alpha^2 C\gamma(1-\gamma)}{C^2(3\alpha^2+1)+C(3\alpha^2+2)\gamma+\gamma^2} \tag{2.74}$$

By taking derivation $\partial\eta/\partial\gamma=0$, we can find the optimal γ.

$$\gamma_O = \frac{1}{1+\sqrt{1+\dfrac{1}{C}+\dfrac{1+C}{C^2(3\alpha^2+1)}}} \tag{2.75}$$

To make rotational bending dominant hence increasing the energy conversion efficiency, we always prefer a large α. Therefore, for the optimal design, we should keep $\alpha \gg 1$. Then, with this condition, we have

$$\gamma_O \approx \frac{1}{1+\sqrt{1+1/C}} \qquad . \tag{2.76}$$

The optimal γ can be further simplified when $D \gg t_1$ (large gap), which is

$$\gamma_O \approx \sqrt{C} = \frac{1}{\sqrt{12}}\frac{t_1}{D} \tag{2.77}$$

The plot of efficiency η as a function of γ with different C is presented in Fig. 2.9. As we can see from the plot, there exists an optimal γ where the energy conversion efficiency η reaches

its maximum value. Once γ_0 is decided, we can easily find the distance between neutral plane and

top piezoelectric beam d_2, and other related parameters such as w_1, w_2 and t_2.
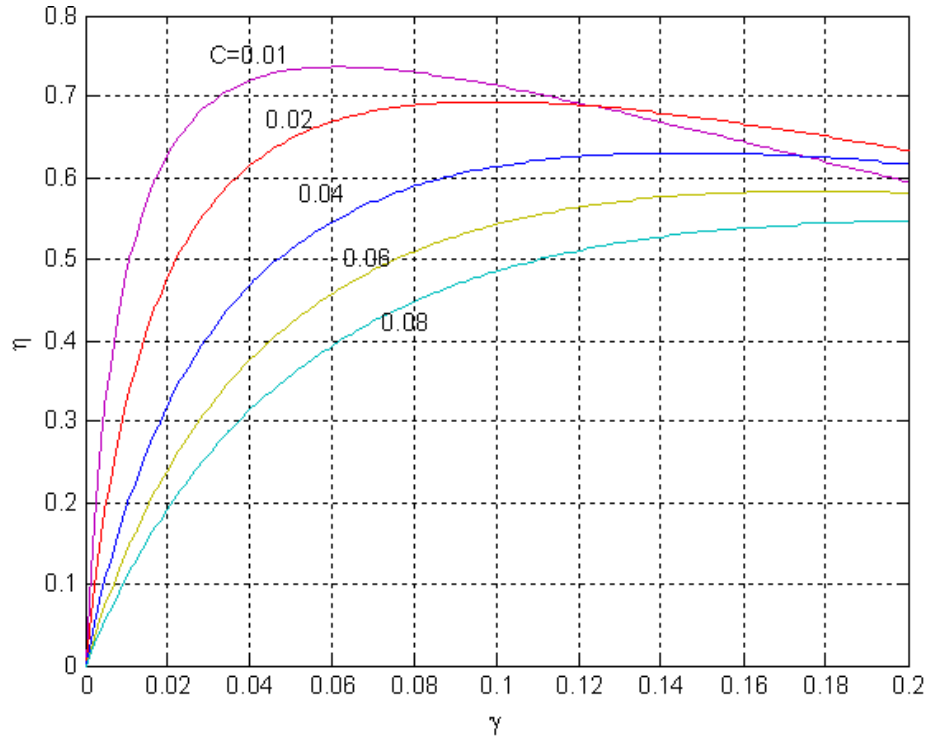
Figure 2.9. Plot of efficiency η as a funtion of γ with different C ($\alpha =5$).

2.5.2 Effect of the air gap

Previously, it's been mentioned that separating the mechanical beam and the sensing

beam with a gap leads to a larger sensitivity. However it is also important to note that without

proper design and optimization, the increased gap may decrease the sensitivity instead. This

phenomenon can be interpreted using energy perspective as well. Figure 2.10 plots η_1, η_2 and η

as functions of D when other parameters are fixed.
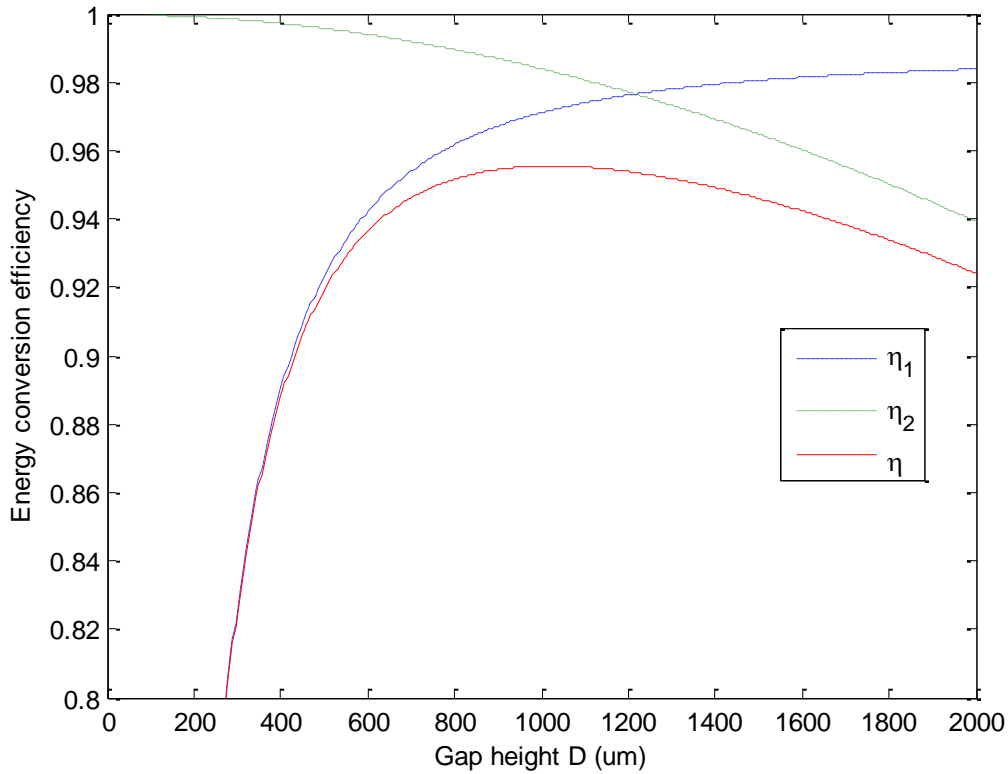
Figure 2.10. Energy efficiencies as functions of D when other parameters are fixed. w_1=400 μm, t_1=50 μm, l_1=120 μm, w_2=20 μm, t_2=2 μm, l_2=20 μm, w_m=2000 μm, t_m=420 μm, l_m=4000 μm.

As we can see from the plot that the total energy conversion efficiency η shows a rapid increase at the beginning and start to decrease after reaching maximum as the gap D increases. This result clearly indicates that the gap between top sensing beam and bottom mechanical beam is not the larger the better.

Looking further into the two sub energy efficiencies, we can observe that a large D always helps to increase η_2 (ratio from energy on top sensing beam by pure stretch/compression to the rotational bending energy) and make it reaches its theoretical limit (i.e., 100%). This is because larger gap separates the top sensing beam from neutral plain further and make it to

stretch or compress even more. This is the exact reason why this gapped cantilever is beneficial and introduced at the first place.

However, we can also see a decrease of a ratio from rotational bending energy to the total bending energy η_1 as the gap D increases. This is because a larger gap increases rotational bending rigidity and makes the cantilever harder to bend in rotational shape. In other words, larger gap leads to a dominance of the translational bending. One solution is to make η_1 almost equal to one and decreases very slowly as the gap D increases. To make this possible, k_R need to be much larger than k_T at the very beginning by properly choosing other parameters. This criterion can be mathematically expressed as

$$N(\alpha,\beta)=\frac{k_R}{k_T}=\frac{1}{3\alpha^2\beta} \ll 1 \tag{2.78}$$

It can be observed that k_R/k_T is a complicated function of many parameters. However, one simple way to satisfy the above inequality is to make the length of the proof mass much longer than the cantilever length, i.e., $l_m \gg l_1$ (equivalent to $\alpha \gg 1$).

2.6 Summary

In this chapter, mechanics of material method is first introduced. Then, the gapped cantilever structure is described schematically with all geometric and material properties defined. Next, the force and bending moment equilibriums for gapped cantilever are analyzed. With all these preparations, the theoretical model for gapped cantilever is developed with the assistance of decomposing the cantilever bending into two bending shapes: rotational bending and translational bending. Finally, an optimization process focusing on energy conversion efficiency

is discussed with the derived model. Some of the most important equations and derived parameters are summarized below in Table 2.2.

Table 2.2. Important equations and parameters derived in the analytical model.

Names	Equations
Bending rigidity for rotational bending	$R_R = E_1 I_1 + E_2 I_2 l_1 / l_2 + E_1 A_1 d_1^2 + E_2 A_2 d_2^2 l_1 / l_2$ (2.36)
Bending rigidity for translational bending	$R_T = E_1 I_1 + E_2 I_2 l_1^3 / l_2^3$ (2.48)
length ratio of proof mass and bottom beam	$\alpha = \dfrac{l_1 + l_m}{l_1}$ (2.51)
Ratio of two bending rigidities	$\beta = \dfrac{R_T}{R_R}$ (2.52)
Spring constant for rotational bending	$k_R = \dfrac{4R_R}{l_1^3 \alpha^2}$ (2.53)
Spring constant for translational bending	$k_T = \dfrac{12 R_T}{l_1^3}$ (2.54)
Resonant frequency (concentrated mass model)	$f_0 = \dfrac{1}{2\pi} \sqrt{\dfrac{k_E}{m}} = \dfrac{1}{2\pi} \sqrt{\dfrac{12 R_T}{m l_1^3 (3\alpha^2 \beta + 1)}}$ (2.56)
Normal strain in top sensing beam	$\varepsilon_2 = \dfrac{\Delta x_2}{l_2} = \dfrac{F l_1 (l_1 + l_m) d_2}{2 R_R l_2}$ (2.57)
Resonant frequency (Rayleigh-Ritz method)	$f_0' = \dfrac{\omega}{2\pi} = \dfrac{1}{2\pi} \sqrt{\dfrac{R_T}{m l_1^3} \dfrac{12(3\alpha^2 \beta + 1)}{(3\alpha^2 \beta + 1)^2 + 3\alpha^2 \beta^2 (\alpha - 1)^2}}$ (2.63)
Energy ratio from rotational bending to total	$\eta_1 = \dfrac{k_T}{k_R + k_T} = \dfrac{1}{1/3\alpha^2 \beta + 1}$ (2.64)
Energy ratio from top stretching to rotational	$\eta_2 = \dfrac{\mu E_2 A_2 d_2^2}{R_R} = (1 - \beta)(1 - \gamma)$ (2.70)
Total energy conversion efficiency	$\eta = \eta_1 \eta_2 = \dfrac{(1 - \beta)(1 - \gamma)}{1/3\alpha^2 \beta + 1}$ (2.71)
Optimal γ	$\gamma_O \approx \sqrt{C} = \dfrac{1}{\sqrt{12}} \dfrac{t_1}{D}$ (2.77)
Criterion to make rotational bending dominant	$N(\alpha, \beta) = \dfrac{k_R}{k_T} = \dfrac{1}{3\alpha^2 \beta} \ll 1$ (2.78)

CHAPTER 3. FINITE ELEMENT SIMULATION

Theoretical analysis of mechanical systems in engineering has been carried out by deriving differential equations of multiple variables using well-known basic physical principles such as equilibrium, conservation of energy, the laws of thermodynamics, Maxwell's equations and Newton's laws of motion. However, it is very difficult or sometimes even impossible to solve such a group of complex equations to derive a mathematical model, especially when dealing with nonlinear partial differential equations. Only very simple problems of regular geometry such as a rectangular or a circle with the simplest boundary conditions are tractable. Therefore, several numerical methods assisted by computer programs have been developed to solve complex mechanical structures to find the mathematical models..

3.1 Finite element analysis

Finite Element Analysis is one of several numerical methods that can be used to solve complex problems and is the dominant method used nowadays. As the name implies, finite element analysis is an approach to break a complex problem down into a finite number of simple problems and finally develop the system model by adding up all the solutions of each of these finite problems.

Practically, it breaks the continuous mechanical structure into a large number of analogue finite elements such as triangular or quadrilateral shape in two dimensions and cube or triangular prism shape in three dimensions. Each element in a finite element model will have a fixed number of nodes that define the element boundaries to which loads and boundary conditions can be applied. The breaking down procedure is usually called 'mesh'. An example of a 2D mesh with triangular shape finite element is shown in Fig. 3.1. One principle regarding mesh is that the

finer the mesh, the closer we can approximate the geometry of the structure, the load conditions, as well as the stress and strain gradients. It's also worth noting that regions of interest (e.g. regions that have large stress) usually have a higher mesh density than other regions. However, the tradeoff is that it will take much more time for the computer to calculate the mathematical model if meshed element number increases. Therefore, learning how to limit the finite element numbers and meanwhile guarantee enough calculation accuracy is a crucial skill as an engineer for finite element analysis.
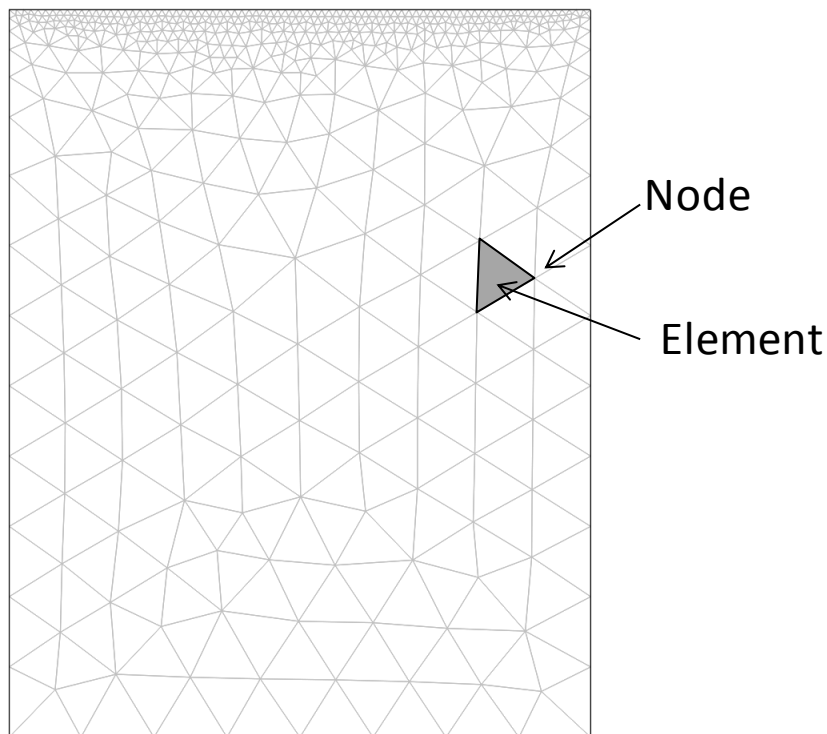
Figure 3.1 Mesh of a block in 2D. Each triangle in the picture represents an element. One triangular element has 3 nodes and 3 boundaries.

Using finite element analysis, one can easily predict how a product reacts to real-world forces, vibration, heat, fluid flow, or other physical effects. Therefore, once a design idea came

out, engineers can directly use finite element analysis to analyze whether the product work the way it was designed or just predict what is going to happen.

3.2 COMSOL FEA software

The commercial FEA software COMSOL version 4.3 is used to model the gapped cantilever structure in this work. A screen shot of COMSOL software interface is shown in Fig. 3.2.
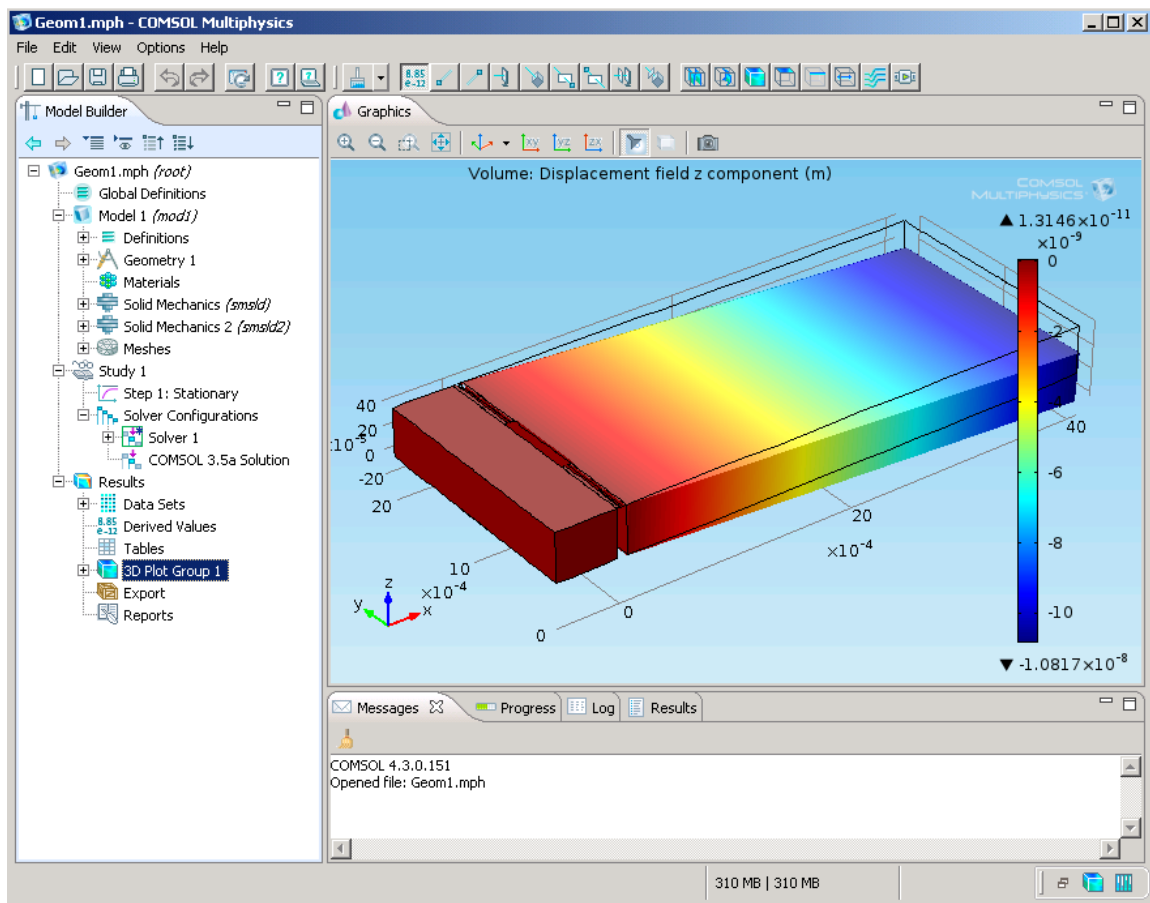
Figure 3.2 Screen shot of COMSOL version 4.3 interface.

The simulation process of a mechanical stress-strain problem in COMSOL is summarized below:

1. Pre-processing

a) Design of physical model: In this step the proper physical module is selected from the simulator, which determines the physical mechanism for modeling. The geometry of the model is then drawn in the simulator along with selection of materials properties for each domain and the assignment of boundary conditions.

b) Meshing: The geometric domain is meshed based on a balance between accuracy required and the available computing power. A fine mesh creates more discrete elements in the model which gives more accurate results. However, the time required to compute the problem also increases when the number of elements increases. In this work, a fine mesh is implemented on the top sensing beam and bottom mechanical beam which experience large stress and strain. On the other hand, a coarse mesh is implemented to base and proof mass which are rigid enough that the deformation can be neglected.

2. Solving

This step specifies the type of analysis that needs to be done. Static analysis was performed first to find out the displacement of the proof mass and the strain and stress in the top sensing beam when the system is subject to a vertical force or a vertical acceleration at proof mass. Then, an eigenfrequency analysis was performed to obtain the resonant frequencies for several different resonant modes. Frequency response analysis was also performed if necessary to find out the vibration amplitude at different frequencies. Theoretically, vibration amplitude reaches its maximum at resonant frequencies.

3. Post-processing

The solution of finite element simulation is interpreted in several ways. For example, the deformation of the gapped structure can be schematically observed. Values of the deformation, strain or stress at any point in the structure can be directly obtained as well. In addition, a plot of variables of interest along a defined line or a surface can be drawn too. In frequency response analysis, the vibration amplitude versus frequency can also be plotted.

3.3 Finite element analysis of gapped cantilever.

A systematic finite element analysis is carried out in several steps to fully understand the gapped cantilever structure in this work.

3.3.1. Model verification

It is obvious that the first step should be a verification of the theoretical model which is developed in chapter 2. It's important to note that in this step all the assumptions that are made during analytical derivation should preserve in the simulations as well. Three key assumptions are 1) deformation of the proof mass is neglected; 2) mass of the beams are neglected; 3) small deflection is assumed. Practically, 1) the Young's modulus of the proof mass is set to a very high number; 2) the densities of the beams are set to very small numbers; and 3) small deflection option is selected in the simulation to mimic these assumptions.

In order to make sure the model above is valid for all conditions, it's also necessary to simulate in several different cases. Since the bending of gapped cantilever tends to have rotational bending shape or translational bending shape, the simulations are performed in three cases 1) rotational bending is dominant; 2) rotational and translational bending are equally distributed; 3) translational bending is dominant. Mathematically, these conditions can be expressed using the criterion parameter from Eq. (2.73), and that is 1) $N(\alpha,\beta) \ll 1$; 2) $N(\alpha,\beta)=1$;

and 3) $N(\alpha,\beta)\!\gg\!1$. Therefore, three sets of simulations with these three different conditions are designed and the results are compared with analytical calculations. For the purpose of evaluating material effect, three different materials are specified for bottom beam (Aluminum), top beam (PZT) and proof mass (Steel) respectively. The simulation results and corresponding analytical values for the three cases are summarized in Tables 3.1 ~ 3.3 respectively. Note that the length of top beam and bottom beam are designed as equal in this simulation for simplicity, and the design with different bottom and top beam will be investigated later. Also note that 1 m/s^2 acceleration is applied in vertical direction on the proof mass in static analysis.

Table 3.1. Simulation and analytical results for $N(\alpha,\beta)$=0.11. Geometry parameters: w_1=1.2 mm, t_1=0.3 mm, w_2=0.4 mm, t_2=0.1 mm l=0.5 mm, w_m=1.2 mm, t_m=1 mm, l_m=2 mm

	Simulation	Analytical	Difference(%)
Spring constant (N/m)	1.75e+06	1.88e+06	6.78
Resonant frequency f_0 (Hz)	4.41e+04	4.66e+04	5.43
Average normal strain ε	9.82e-09	1.04e-08	5.72

Table 3.2. Simulation and analytical results for $N(\alpha,\beta)$=1.03. Geometry parameters: w_1=1 mm, t_1=0.3 mm, w_2=0.5 mm, t_2=0.1 mm l=1 mm, w_m=1 mm, t_m=1.2 mm, l_m=1.4 mm.

	Simulation	Analytical	Difference (%)
Spring constant (N/m)	8.91e+05	9.77e+05	8.73
Resonant frequency f_0 (Hz)	4.04e+04	4.29e+04	5.81
Average normal strain ε	4.60e-09	4.79e-09	3.88

Table 3.3. Simulation and analytical results for $N(\alpha,\beta)$=10.3. Geometry parameters: w_1=1 mm, t_1=0.2 mm, w_2=0.5 mm, t_2=0.1 mm l=1 mm, w_m=1 mm, t_m=2 mm, l_m=1.4 mm.

	Simulation	Analytical	Difference (%)
Spring constant (N/m)	5.12e+05	5.39e+05	4.97
Resonant frequency f_0 (Hz)	2.43e+04	2.50e+04	2.68
Average normal strain ε	4.37e-09	4.54e-09	3.81

As shown in the tables above, the analytical values for spring constant, resonant frequency and average normal strain agree very well with simulation results for all three cases. Note that the differences between theoretical model and simulation results can be further reduced by increasing the finite element numbers or using elements with more nodes. The bending shapes of gapped cantilever for three different cases are shown in following figures as well. It's very obvious that rotational bending shape in Fig. 3.3 and translational bending in Fig.3.5 are clearly observed. However, it is difficult to say which shape the bending is close to in Fig. 3.4 since rotational bending and translational bending are equally distributed in this case. In conclusion, the two bending shape theory that we proposed is clearly observed and the accuracy of the analytical model that derived in chapter 2 is demonstrated by finite element method.
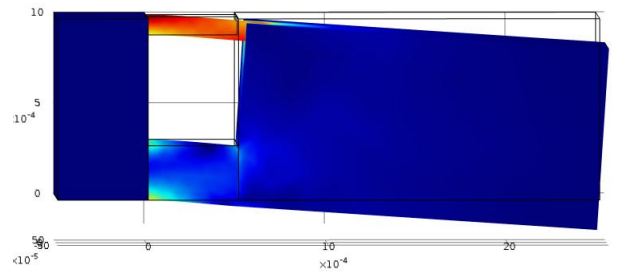
Figure 3.3 Side view of the deformed gapped cantilever when rotational bending is dominant ($N(\alpha,\beta)$=0.11).
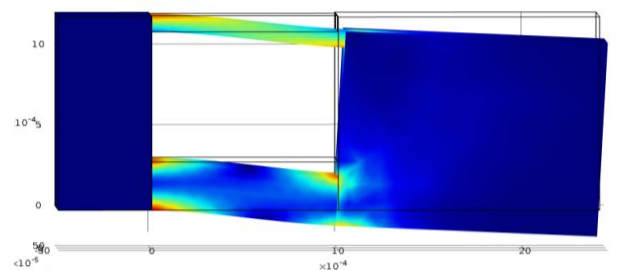
Figure 3.4 Side view of the deformed gapped cantilever when rotational bending and translational bending are equally distributed ($N(\alpha,\beta)$=1.03).
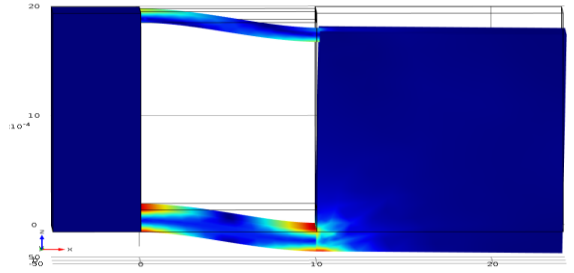
Figure 3.5 Side view of the deformed gapped cantilever when translational bending is dominant (*N(α,β)=10.3*).

3.3.2 Real conditions

It's worth noting that the simulations conducted in the previous section are based on several ideal assumptions. However, it's possible that those assumptions may be far away from the real conditions in many cases. For example, the bending of proof mass cannot be neglected if the proof mass is thin and long or it's composed by a material with small Young's modulus. The mass of the beams cannot be neglected either if the beams are made by materials with high density or the beams are just large enough. In those cases the results from analytical model may have a large difference with the experimental results from real devices. Therefore, it's really important to perform another type of simulation without those assumptions to examine the difference between ideal cases (with assumptions) and real cases for every design.

In these series of simulations, normal Young's moduli of proof mass and normal densities of the beams are applied to simulate the real conditions as close as possible. Note that the large deflection option is not selected in this step since the deflection of the cantilevers is usually very small compared to the length of the device itself. In addition, it will take much more time to calculate with large deflection option which is not efficient at all in the work. Since these types of simulations are targeted for the evaluation of the difference between analytical calculations

and experimental results from real devices, the simulation have to be performed during design period for each of the gapped cantilever applications.

As an example to show the importance of simulation without assumptions, a simple case is presented in the following. The geometric and material properties of the gapped cantilever in this simulation are summarized in Table 3.4. The simulation results with assumptions, simulation results without assumptions and analytical results are listed in Table 3.5. As we can see in the tables, the simulation results with ideal assumptions agree very well with analytical calculations. However, the simulation results without those assumptions show a fairly large discrepancy with analytical results. Since the simulations without assumptions must be closer to the real conditions, we have to consider these results as better expectation for the performance of the real device in the design phase in this case.

Table 3.4 Geometric and material properties of bottom beam, top beam and proof mass for the simulated gapped cantilever.

	Bottom beam	Top beam	Proof mass
Length (mm)	1	1	3
Width (mm)	1	0.5	0.1
Thickness (mm)	0.2	0.1	0.5
Young's modulus (GPa)	70	62	200
Density (kg/m^3)	2700	7800	7800

Table 3.5. Simulation results with and without ideal assumptions and analytical results for gapped cantilever defined in table 3.4.

	Simulation with assumption	Simulation no assumption	Analytical
Spring constant (N/m)	7.75×10^4	7.22×10^4	7.81×10^4
Resonant frequency f_0 (Hz)	1.21×10^4	1.16×10^4	1.22×10^4
Average normal strain ε	1.86×10^{-8}	1.85×10^{-8}	1.86×10^{-8}

However, it's also worth noting that analytical calculations are much more convenient and take much less time than simulations. In addition, the analytical results are usually not too far away from simulations without assumptions as we can see in Table 3.5. Therefore, there is no doubt that the analytical model that developed in this work can provide accurate enough guidance during the design period, and simulations are used to assist verifying and finding more precise expectations of the design.

The deformation of gapped cantilever with normal beam mass and normal proof mass stiffness is presented in Fig. 3.6. Compared with the results seen from Figs 3.3~3.5 in which the proof mass is rigid, we can observe a slight deformation of the proof mass in this case.
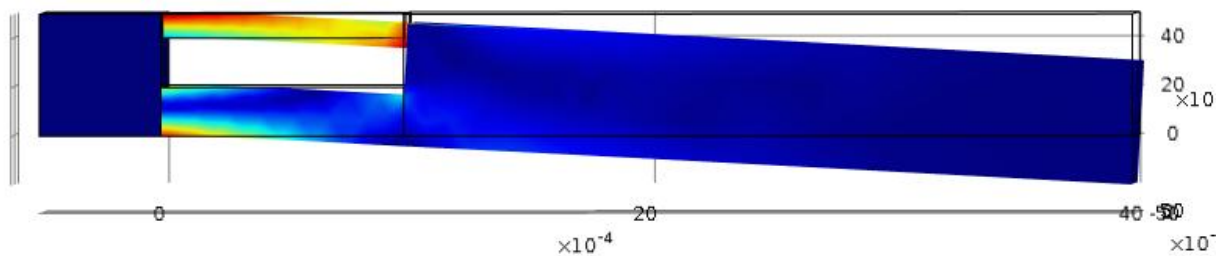
Figure 3.6 Side view of the deformed gapped cantilever with no assumptions made.

3.3.3 Higher resonant modes

In the previous simulations, we assumed the proof mass resonates in vertical direction and only focused on this resonant mode. However, as well known, there are multiple resonant modes in mechanical vibrations. It's worth noting that resonant frequencies of other resonant modes could be very close to the vertical mode and sometimes even smaller than that for gapped cantilever structure. In these cases, the performance of the devices may be severely affected by those other resonant modes and it is difficult to achieve the normal function that we expected.

Considering difficulty to calculate higher resonant modes theoretically, it is very important to perform finite element simulation to find out other resonant modes. If the results show resonant frequencies of other modes close to the vertical mode, it is also required to modify design or look for solutions to avoid or compensate that. This process is again need to be done for every design in the real applications.

As an example of investigating higher resonant mode, another series of simulations is performed in this section. The geometric and material properties of the gapped cantilever in this simulation are summarized in Table 3.6. At this time, an eigenfrequency analysis is utilized to study multiple resonant modes of the gapped cantilever. The first three resonant frequencies and corresponding resonant mode shapes are summarized in Table 3.7 and Figs. 3.7~3.9 respectively.

Table 3.6 Geometric and material properties of bottom beam, top beam and proof mass for the simulated gapped cantilever.

	Bottom beam	Top beam	Proof mass
Length (mm)	1	1	2
Width (mm)	0.8	0.2	2
Thickness (mm)	0.2	0.1	1
Young's modulus (GPa)	70	62	Infinity
Density (kg/m^3)	0	0	7800

Table 3.7. Simulation results of the first three resonant frequencies for gapped cantilever with properties specified in Table 3.6.

Resonant mode number	1	2	3
Resonant frequency (Hz)	1.06×10^4	1.23×10^4	1.75×10^4
Mode shape	Lateral	Vertical	Torsional
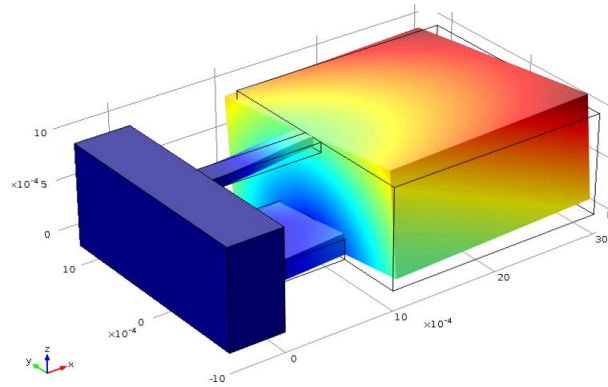
Figure 3.7 Illustration of the mode shape corresponding to the first resonant frequency (10.6 kHz). The deformation of the gapped cantilever is close to lateral (y-direction) bending.
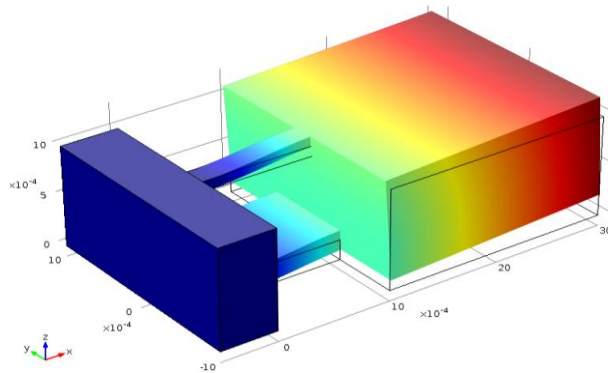
Figure 3.8 Illustration of the mode shape corresponding to the second resonant frequency (12.3 kHz). The deformation of the gapped cantilever in this mode is vertical (z-direction) bending.
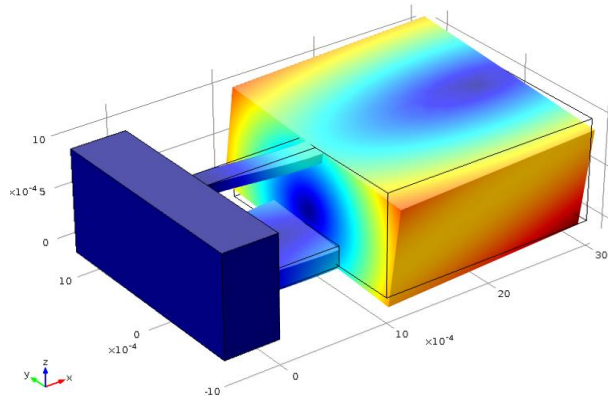
Figure 3.9 Illustration of the mode shape corresponding to the third resonant frequency (17.5 kHz). The deformation of the gapped cantilever in this mode is torsional around x-axis.

As we can see from the simulation results that the resonant frequency of lateral vibration mode is smaller than vertical vibration mode. In this case, there is a high possibility that lateral vibration is dominant, and the device will not vibrate in vertical direction which we expected to see. Another problem with other dominant resonant mode is that the device may be easily damaged due to unexpected deformations.

Additionally, we can also observe from the results that the resonant frequency of torsional vibration is higher but still very close to the resonant frequency of the vertical mode. This adjacent torsional vibration may also severely affect the vertical vibration. Consequently, torsional vibration along with lateral vibration interfere the signal from the device which is only supposed to pick up the signal from vertical vibration mode. In this case, it is really difficult to post-process the signal to extract useful information about vertical vibration that we are interested in. Therefore, it is really necessary to design carefully to make vertical vibration mode far more dominant than other resonant modes with the assistance of finite element simulations.

In fact, splitting top and bottom beams into two and separating them far away from each other is a very effective way to suppress lateral and torsional vibrations. In the following, another simulation result is presented to show the effect of this approach. The geometric and material properties are kept the same as previous simulation which are shown in Table 3.6. The only difference in this step is that the bottom and top beams are both split in half and each piece is moved the two edges in lateral (y) direction. Theoretically, this change will not affect the vibration in vertical direction but only suppress lateral and torsional vibrations. The simulation results are shown in Table 3.8. Comparing the new simulation results with previous ones shown in Table 3.7, we can clearly observe an increase of the resonant frequencies for lateral and torsional vibration modes without varying the resonant frequency of vertical mode. Consequently,

the resonant frequency of vertical vibration mode is turned to be the lowest one with this new design. This means vertical vibration will be dominant now and less interferences will be induced by other resonant modes. Therefore, if there is no much of difficulty during development phase, the cantilever beam splitting scheme is always preferable in the applications. The illustrations of the deformed of gapped cantilever with bottom and top beams split are shown in Figs. 3.10~3.12.

Table 3.8. Simulation results of the first three resonant frequencies for gapped cantilever after bottom and top beams are split.

Resonant mode number	1	2	3
Resonant frequency (Hz)	1.23×10^4	1.96×10^4	3.63×10^4
Mode shape	Vertical	Lateral	Torsional
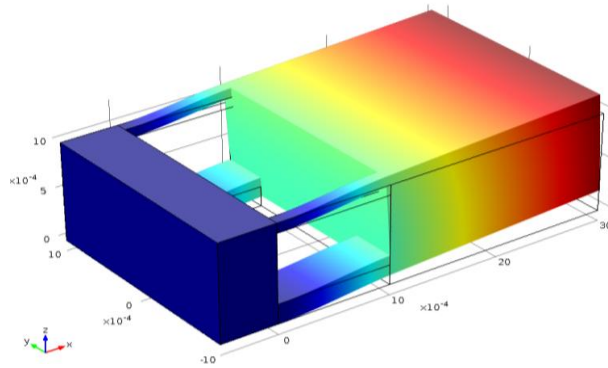
Figure 3.10 Illustration of the mode shape corresponding to the first resonant frequency after bottom and top beams are split (12.3 kHz). The deformation is in vertical direction.
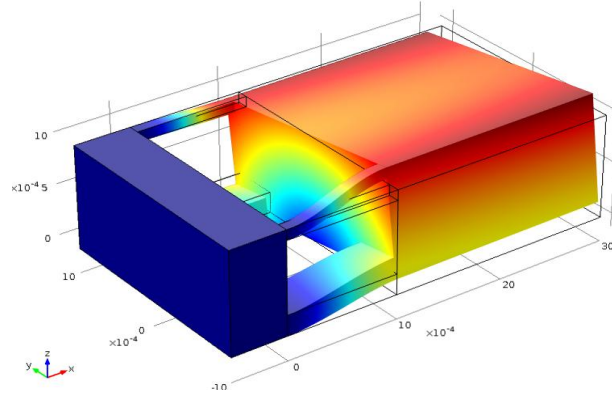
Figure 3.11 Illustration of the mode shape corresponding to the second resonant frequency (19.6 kHz) after bottom and top beams are split. The deformation is close in lateral direction.
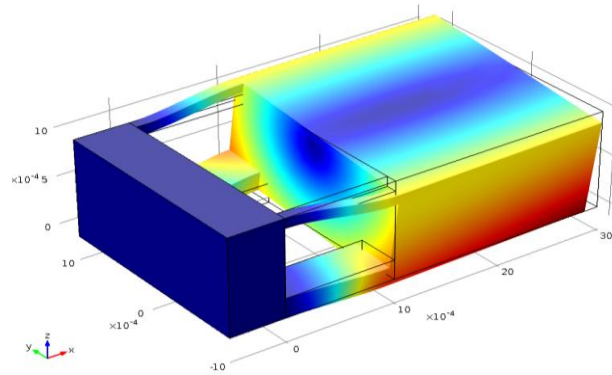
Figure 3.12 Illustration of the mode shape corresponding to the third resonant frequency (36.3 kHz) after bottom and top beams are split. The deformation is in torsional.

3.4 Summary

In this chapter the finite element simulation of gapped cantilever is studied systematically. First of all, a brief introduction of finite element analysis has been presented. The FEA, assisted by computer program, is one of the most popular numerical methods that can be used to solve complex mechanical problems. In this work, a commercial FEA software Comsol version 4.3 is used to simulate gapped cantilever structure. Finite element simulations are performed in several steps for different purposes. First, the analytical model developed in chapter 2 is verified using FEA. In this step, the three ideal assumptions (rigid proof mass, zero beam mass and small

deflection) made during analytical model derivation are kept the same. The results show a great agreement between simulation and theory, and therefore the analytical model is verified. Next, another series of simulations is performed with all ideal assumptions removed, and the larger discrepancy between real case and analytical calculations is shown. This tells us the analytical calculations sometimes may not precisely predict the performance of real devices and it is really necessary to simulate the real conditions to make a better estimation. In the last, a series of eigenfrequency analyses has been performed to study lateral and torsional resonant modes other than vertical resonant mode. The results from this simulation indicate that there is a chance that lateral and torsional modes may interfere vertical mode if the gapped cantilever is not properly designed. One direct solution is that bottom and top beams can be split and widely separated to suppress lateral and torsional vibration mode, and this approach is demonstrated by simulations as well. In conclusion, finite element simulation is an excellent tool to assist the design of gapped cantilever transducers and it will be implemented specifically for each of the applications in the following several chapters.

CHAPTER 4. PIEZORESISTIVE ACCELEROMETER

Gapped cantilever structure has proven to have a great potential to increase the sensitivity of cantilever based sensors by both analytical calculation in chapter 2 and finite element simulation in chapter 3. Now, it is time to seek the applications of gapped cantilever in engineering by taking the advantage of high sensitivity. As the first demonstration, the most typical and popular cantilever based sensor, piezoresistive accelerometer is chosen in this work.

4.1 Introduction

4.1.1 Piezoresistive accelerometer

Micromachined accelerometers have been extensively researched in the past several decades due to their small size, low power consumption, low unit cost, and the possibility of integration with circuits. These sensors are used for a large variety of military, industrial, medical and consumer applications. Among various sensing mechanisms for micromachined accelerometers [31], piezoresistive sensing has been a popular choice [1, 6, 8, 11, 12, 32-39]. However, low sensitivity has been recognized as one of the disadvantages of piezoresistive accelerometers [17]. There are several approaches to address this issue. For instance, the sensitivity can be increased by selecting the proper geometric dimensions of the cantilever and proof mass. Furthermore, the sensor performance can be improved by optimizing the piezoresistors on the cantilever using methods similar to those reported in [10, 14, 40]. Alternatively, the performance of the piezoresistive accelerometers can be improved by employing some novel configurations. Suminto reported a configuration in which the support beam of the proof mass was composed of a central hinge and two decoupled piezoresistors [41]. Later, a high performance piezoresistive accelerometer, consisting of two axially-stressed tiny

beams combined with a central supporting cantilever, was demonstrated by Huang et al based on a similar idea [17].

In this work, the development of a piezoresistive accelerometer based on a gapped cantilever structure is reported. It is worth noting that patents issued to Wilner in Endevco Corporation and Kurtz in Kulite Semiconductor Products, Inc. in the 1960s and 1970s have described similar structures with strain gauges mounted across a gap or slot [26, 28]. The silicon micromachined versions of such a structure were also described in later patents [27, 29]. In 2005, Naeli *et al.* reported the development of piezoresistive cantilevers using a similar stress concentration structure [25]. Nevertheless, how the sensor's performance is affected by the geometrical parameters of the asymmetrically-gapped cantilever has not been systematically studied. Consequently, there is no well-developed methodology for the optimization of the design and the potential of this structure has not been fully realized. As a matter of fact, this structure may degrade, instead of enhance, the sensor performance if not properly designed.

4.1.2 Continuous lung sound monitoring

Among numerous applications of micromachined accelerometers, the original goal of inventing the more sensitive piezoresistive accelerometer in this research is to accurately and continuously monitor human lung sound (or respiratory sound). In the following, the importance of continuous lung sound monitoring is first introduced to further emphasize the significance of our work. Then, the requirements of the accelerometer for lung sound measurement are analyzed for preparation of the sensor design.

4.1.2.1 Importance of continuous lung sound monitoring

Most people probably have experience with respiratory sound monitoring via stethoscope auscultation in the clinic or hospital or just in a regular physical checkup. In fact, respiratory sounds play much more important roles than most of us realize. They are physiological vital signs (together with heart sounds, heart rate, blood pressures, oxygen saturation, etc.) designated by American Society of Anesthesiologists (ASA), containing a rich reservoir of vital physiological and pathological information [42-44]. We are very familiar with the scenes on TV/movie or from personal experience that the electrocardiogram (ECG) of the patient is being continuously monitored in ORs or ICUs. But we have never seen continuously monitoring of respiratory sound. This is not because the respiratory sounds are not important. Instead, this is because the technology of continuous respiratory sound monitoring is far from mature at this moment.

The successful development of the proposed accelerometer will have significant impacts on various clinical and healthcare applications. One specific example is anesthesia monitoring in the operating room. The continuous monitoring, recording and computer-assisted signal processing of respiratory sounds can provide critical and prompt information in situations of airway complications such as pulmonary edema, bronchial intubation, tube malfunctioning, etc. [45-47]. For instance, when bronchospasm occurs during surgery, a pattern change in breathing sounds is perhaps its fastest indication. Unfortunately, now in the operation room, the respiratory sound is only monitored intermittently using stethoscopes. Our technology will allow direct, continuous, and non-invasive monitoring of pulmonary functions, greatly enhancing the diagnosis capability that is currently provided indirectly by measured variables such as airway pressure, flow rate, O_2 and CO_2 levels, blood O_2 saturation, etc. The potential impact of the

system on the targeted anesthesia application will be substantial in increasing diagnostic accuracy and speed, avoiding unnecessary lab tests, easing the physician stress levels, increasing decision accuracy, reducing drug consumption, shortening recovery time and hospital stay, and enhancing the safety of the anesthesia decision process. It will, therefore, improve the quality of anesthesia and patient care in ORs.

This technology will have important applications to many other clinical areas in which the non-invasive and continuous monitoring of lung functions plays an important role. This includes continuous asthma monitoring for severity characterization, diagnosis, and drug impact analysis; non-invasive vital sign monitoring for pilots and other military personnel; patient monitoring in ICU, nursing facilities and Emergency Medical Services (EMS); the assessment of drug effectiveness for pain management in cancer patients, etc. [48-55]. Consequently, the successful development of this technology will break grounds for developing smart monitoring systems in many clinical applications. When integrated ultimately with wireless communication capability, it would be a convenient option to connect the device with communication and internet systems for telemedicine.

4.1.2.2 Technology

In the following paragraphs, a brief introduction to respiratory sound detection is presented and challenges of continuous respiratory sound monitoring are discussed. The dominant tool for measuring respiratory sounds is the stethoscope, which is comprised of a bell-shaped air chamber and a microphone to pick up sound signals. As shown in Fig 4.1 (a), the respiratory sound generates a vibration on the chest skin with an amplitude of x_1. Due to the amplification effect of the air chamber, the vibration amplitude on the microphone membrane x_2 is much larger. Although widely used, the stethoscope has a number of limitations for continuous

respiratory sound monitoring. For instance, the stethoscope is bulky due to the air chamber. Therefore, it is difficult to be body-worn or applied to obstructed auscultation sites. Furthermore, the signal picked up by the stethoscope is very sensitive to the way in which the stethoscope is applied on the patient (location, angle, force, etc.), and a slight movement (e.g., caused by patient) may result in a complete loss of the respiratory signal. Therefore, stethoscopes are only used for intermittent auscultation but are not suitable for continuous respiratory sound monitoring.

The vibration of the skin due to respiratory sounds can also be detected by accelerometers [43, 56-58]. Compared with the stethoscope, the accelerometer is in direct contact with the skin and does not need an air chamber to couple the acoustic signal. However, the accelerometers need to be much more sensitive since there is no air chamber to amplify the signal. For monitoring respiratory sounds, especially lung sounds, we have found that the resolution of the accelerometer needs to be $\sim 1\mu g/Hz^{1/2}$ ($1\mu g$ represents the acceleration equivalent to one millionth of the gravity of earth). A highly sensitive accelerometer usually requires a large proof mass. The conventional packaging method also increases the overall mass and size significantly. Therefore, current high sensitive accelerometers usually are heavy and bulky.
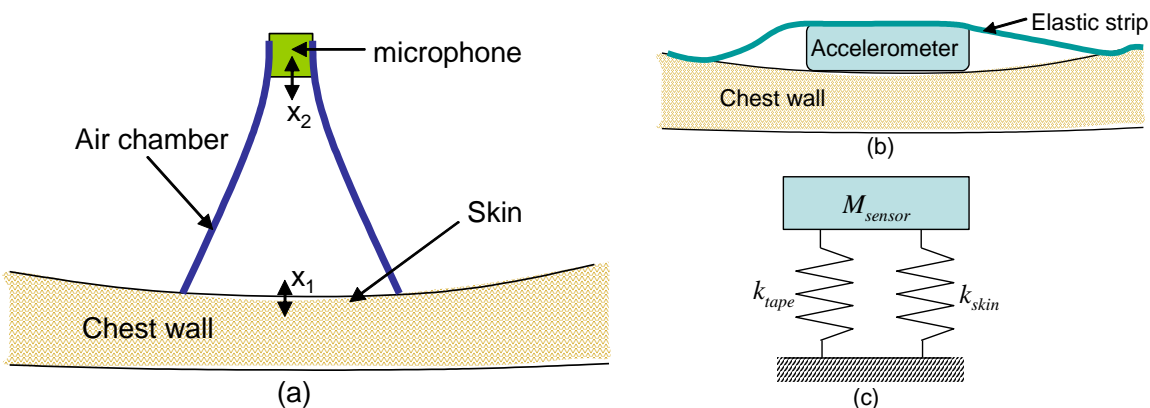
Figure 4.1. (a) A schematic drawing of the operating principle of the stethoscope after [43]; (b) a schematic drawing of using an accelerometer to detect respiratory sounds; (c) a simplified

mechanical model of an accelerometer attached to the chest by an elastic strip. M_{sensor} is mass of the whole sensor including packaging.

To detect respiratory sounds, an elastic strip is usually used to tape the sensor on the chest wall as shown in Fig. 4.1 (b). The large mass of the sensor has an important disadvantage, i.e., mass-loading effect. The mass-loading effect induces a cut-off frequency that is given by

$$f_o = \frac{1}{2\pi} \sqrt{\frac{k_{tape} + k_{skin}}{M_{sensor}}} \tag{4.1}$$

where k_{eff} is the effective spring constant determined by the skin and tape. The above equation indicates that when the mass of the sensor is too large, the cut-off frequency will be fairly low, and the higher frequency components of the respiratory signals will be significantly attenuated. This is the undesirable mass-loading effect [43, 57, 59].

For continuous respiratory sound monitoring, another requirement is that these accelerometers need to be wearable, or more specifically, can be attached to the skin conveniently and comfortably. This is not only a nicety but also a necessity for this type of device to be widely accepted by doctors and patients. For example, in the operating room, the sensor needs to be applied to obstructed auscultation sites. For daily life asthma or vital sign monitoring, the sensor has to be comfortable and non-visible.

In conclusion, the accelerometers for continuous respiratory sound monitoring have to be (1) sensitive, (2) light-weight and (3) wearable. There have been a few efforts in developing systems for continuous respiratory sound monitoring [60, 61]. Most of these efforts were based on off-the-shelf stethoscopes/microphones or accelerometers. So far we have not seen any sensor that satisfies all three requirements. As a result, in most clinical studies that involved

continuous respiratory sound monitoring, off-the-shelf accelerometers and stethoscopes were used [45-48, 51]. Even though all these studies were done in a well-controlled clinical environment, the performance was not satisfactory. For example, Nishida et al. stated that in 21 of 43 cases in their clinical study, the monitoring system failed to measure respiratory sounds continuously enough for the diagnosis of diseases [62]. The continuous monitoring of respiratory sounds in the non-controlled daily environments is much more challenging and has not been achieved so far.

4.2 Design

Even though continuous lung sound monitoring requires the accelerometer to be wearable, the priority task of our work is the design of a highly sensitive micromachined piezoresistive accelerometer. In this section, the proposed accelerometer based on gapped cantilever structure is presented first. Then, the performances are analyzed by discussing sensitivity and noise issues.

4.2.1 structure

The structure of the piezoresistive accelerometer based on gapped cantilever is schematically shown in Fig. 4.2(a). For this design, the supporting beam of the proof mass is a composite cantilever, consisting of a bottom mechanical layer and a top piezoresistive layer (red color) separated by a gap. Note that, as introduced in section 3.3, top beam is split into two and widely separated in order to suppress lateral and torsional vibration mode in this design. This structure is also preferable in the fabrication process as explained later in section 4.4. The advantage of this design can be conceptually explained by using the cross sectional view in Fig. 4.2(b). The mechanical strain experienced by the piezoresistors is proportional to d_2, the distance between the piezoresistors and the neutral plane. This conclusion is valid for

conventional cantilevers as well. However, for gapped cantilevers, this distance is approximately equal to the height of the gap between the top and bottom beams, which can be as large as the wafer thickness (e.g., 400 μm). For the conventional cantilever, this distance is only half of the cantilever thickness, which is much smaller. Therefore, this design leads to a higher sensitivity. For the first demonstration, the following parameters are selected in our design: w_1=400 μm, t_1=50 μm, l_1=120 μm, w_2=20 μm, t_2=2 μm, l_2=20 μm, w_m=2000 μm, t_m=420 μm, l_m=4000 μm, D=394 μm and E_1= E_2= E_m=168 Gpa. Based on the analytical model derived in chapter 2, a resonant frequency of 5.85 kHz and an average normal strain of 5.23 ×10^{-5} on the top piezoresistive beam (with 1 g vertical acceleration) are calculated.

(a) (b)
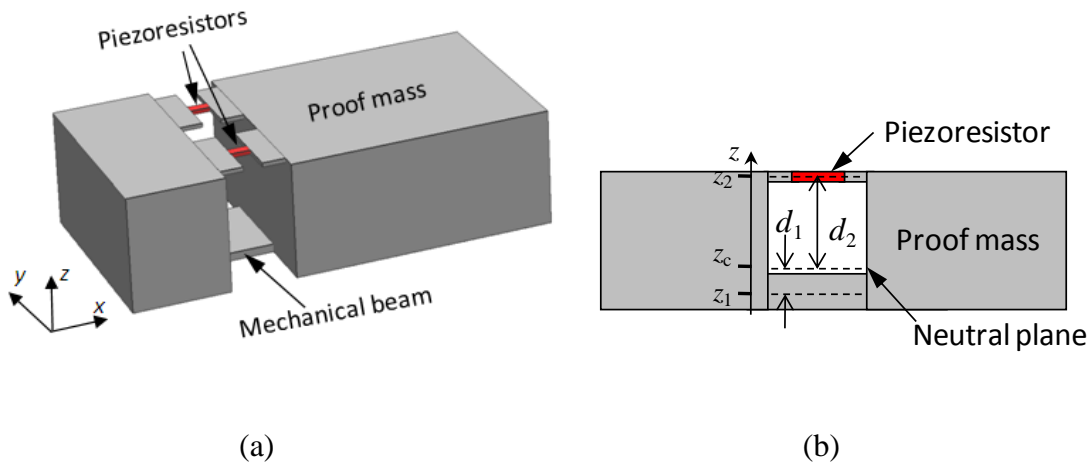
Figure 4.2. (a) Schematic structure of the accelerometer based on gapped cantilever structure. The dimensions (width × thickness ×length) of the bottom mechanical beam, the top short piezoresistive beams and proof mass are w_1 × t_1 × l_1, $0.5w_2$ × t_2 × l_2 and w_m × t_m × l_m, respectively. (b) Cross sectional view of the accelerometer based on gapped cantilever structure. z_1 and z_2 are the coordinates of the middle planes of the bottom and top beams. z_c is the effective neutral plane.

4.2.2 Sensitivity

If the piezoresistor is configured as a Wheatstone bridge with three other reference resistors, the output voltage will be

$$\Delta V = \frac{1}{4} \frac{\Delta R}{R} V_0 = \frac{1}{4} \varepsilon_2 G V_0 \qquad (4.2)$$

where V_0 is the supply voltage of the Wheatstone bridge, G is the gauge factor and ε_2 is the mechanical strain. Based on Eq. (2.57), the sensitivity is

$$S = \Delta V / a = \frac{m(l_1 + l_m)\mu d_2}{8R_R} GV \qquad (4.3)$$

It can be clearly observed that the sensitivity is proportional to d_2, the distance between the middle plane of the piezoresistor and the neutral plane of the gapped beam. The position of the neutral plane is determined by the ratio of cross sectional areas of top and bottom beams. For an optimized design, the cross section of the bottom beam is much larger than the top beams. Therefore, the neutral plane is very close to the bottom beam. Consequently, the distance between the top sensing beam and the neutral plane is approximately equal to the wafer thickness, e.g., ~400 μm. For the conventional design, the neutral plane is usually in the middle of the beam, and d_2 is simply half of the cantilever thickness, which is usually much smaller. Therefore, the design based on gapped cantilever has a sensitivity higher than that of the conventional one.

A specific design of conventional piezoresistive accelerometer is given to show the increase of sensitivity quantitatively. To make a meaningful comparison, the proof masses of the two designs are identical. The length and width of the conventional cantilever are chosen to be 120 μm and 400 μm, same as the bottom beam of the gapped cantilever. The thickness is selected to be 82 μm, resulting in the same spring constant as the gapped cantilever. The piezoresistor is placed on the top surface of the cantilever and is 2 μm thick. The sensitivity of this conventional design (assuming rigid boundary condition) is 1.98×10^{-6}/g, 25 times less than

our new design. Even if the soft boundary is considered, the design based on the gapped cantilever is still 21 times more sensitive.

It must be noted that the sensitivity improvement predicted by Eq. (4.3) is based on the assumption that R_R remains constant when d_2 increases. Since $\mu E_2 A_2 d_2^2$ term is dominant in R_R equation for an optimized design, it is necessary to decrease the cross sectional area of the piezoresistors accordingly to keep R_R constant. This is an important design rule for gapped cantilevers.

It can also be observed from Eq. (4.3) that translational bending does not affect the sensitivity. This is because translational bending generates opposite mechanical strains across the middle plane of the top piezoresistive beams. The mechanical strains cancel with each other and do not lead to net resistance change if these strains are small and only first order effect is considered. Although translational bending does not contribute to the sensitivity, it does decrease the resonant frequency. Therefore, translational bending should be minimized when the bandwidth is considered. This requirement can also be derived from the energy perspective, i.e., the energy should be concentrated in rotational bending.

4.2.3 Noise

Noise is another critical issue of transducers. For piezoresistive accelerometers, there are three major noise sources: 1/f noise, Johnson noise and thermomechanical noise. At low frequencies, 1/f noise, given by the following equation, is typically dominant [9, 14, 15, 63]

$$\frac{\langle v \rangle^2}{\Delta f} = \frac{\alpha_H V^2}{f^n N} \tag{4.4}$$

where *f* is the frequency, *N* is the total carrier number in the piezoresistor, *V* is the voltage across the piezoresistor, *n* is typically between 0.9-1.1 [4], and α_H is an empirical coefficient usually called Hooge factor.

The buckling and self-heating of the piezoresistive layer of the gapped cantilever have been discussed elsewhere [18]

4.3 Finite element simulation

Finite element simulation has been carried out to verify the analytical calculations. In the finite element simulation, the top piezoresistive beam is selected to be 20 μm long, 10 μm (each beam) wide, and 2 μm thick. As explained later, piezoresistive beams are fabricated using the device layer of the SOI (Silicon-in-Insulator) wafer. The length, width and thickness of the bottom beam (mechanical beam) are 120 μm, 400 μm and 50 μm, respectively. The proof mass has a dimension of $4000 \times 2000 \times 420$ μm³. The distance between the middle planes of the top and bottom beam *D* is approximately 394 μm. Note that as shown in Eq. (4.3), a short piezoresistive beam is preferred for higher sensitivity. Due to the aspect ratio limit of DRIE, the piezoresistors are connected to wide plates (as shown in Fig. 4.2(a)) which are also formed by the device layer. Since the plates are much wider than piezoresistors, they are treated as rigid boundary in our analytical model.

Static analysis is first conducted with 1 g vertical acceleration applied on the structure. Figure 4.3 schematically shows the simulation results of the deformed piezoresistive accelerometer based on gapped cantilever structure.
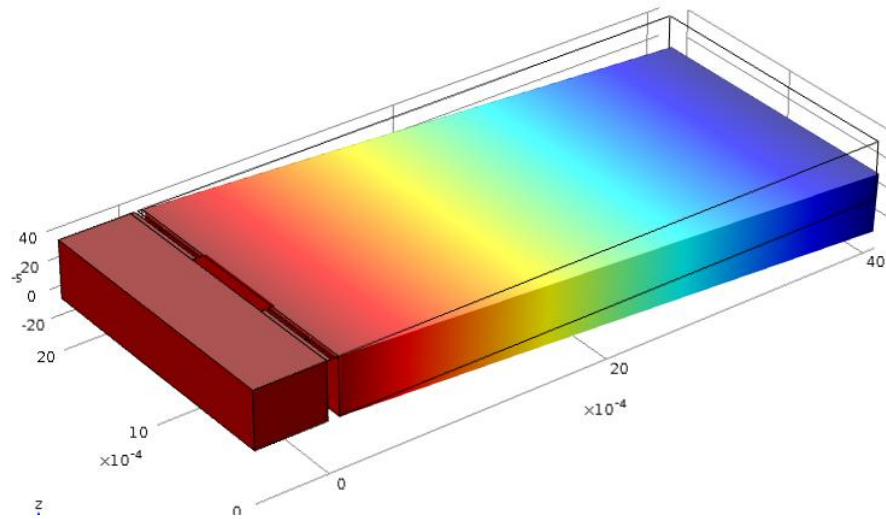
Figure 4.3 Simulation result of the deformed piezoresistive accelerometer based on gapped cantilever structure.

In addition to rigid boundary condition which is asumed in analytical model as well, soft boundary case is also simulated in order to anticipate real situation and to evaluate the accuracy of our analytical model. The simulation results of normal strain experienced by top piezoresistor along x-axis are ploted in Fig. 4.4 in both rigid and soft boundary cases. As we can see from the figure that, the normal strain apears to be nearly constant along the piezoresistive beam, but shows a rapid decay close to the boundaries ajacent to base and proof mass. This is normal when two subjects experiencing different strains are connected together. Due to the non-uniformity of the strain in the piezoresistors, an average normal strain is calculated from the simulation results as shown in Table 4.1. It can also be observed from Fig. 4.4 and Table 4.1 that the normal strain in piezoresistor is larger in case of rigid boundary compared with soft boundary case. This can be easily explained by the strain distribution on piezoresistor and the ajacent boundaries as shown in Fig. 4.4 (insets) that the soft boundaries share some of the strain energy from piezoresistor.
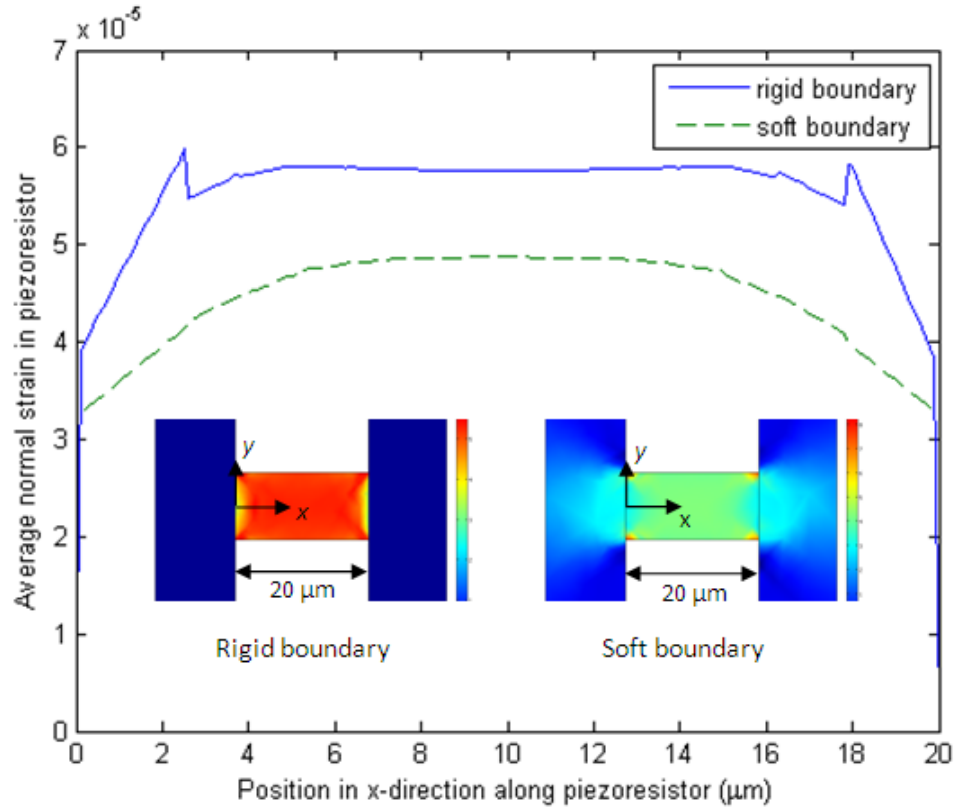
Figure 4.4 The average normal strain (in *x* direction) experienced by the top piezoresistive beams for both rigid boundary and soft boundary cases. The acceleration applied is 1g in vertical direction. Insets show the top views of the normal strain distribution in the piezoresistors and ajacent boundaries.

The fundamental resonant frequency has been studied using finite element simulation as well. The simulation results and corresponding analytical values are listed in Table 4.1. The resonant frequencies are calculated using both concentrated mass model and Rayleigh-Ritz method and the difference is about 15% for this specific design. As expected, the resonant frequency calculated by Rayleigh-Ritz method matches with the simulation result based on rigid boundary condition very well.

Table 4.1. Analytical and simulation results for the designed piezoresistive accelerometer. The analytical resonant frequencies are calculated using both concentrated mass model and Rayleigh-

Ritz method. The finite element simulation is carried out for both rigid boundary and soft boundary cases.

	Analytical		Simulation	
			Rigid boundary	Soft boundary
Resonant frequency f_0 (kHz)	Concentrated Mass	6.71	5.84	3.96
	Rayleigh-Ritz	5.85		
Average normal strain ε_2 (with 1 g acceleration)	5.23×10^{-5}		5.26×10^{-5}	4.28×10^{-5}

It is worth nothing that the proof mass can also resonate in lateral and torsional modes. Eigenfrequency analysis shows that the resonant frequencies of lateral and torsional modes are 15.4 kHz and 23.5 kHz respectively, which are much higher than the resonant frequency of vertical mode. The corresponding mode shapes are schematically shown in Fig. 4.5. In the future development, the bottom beam can also be split into two and widely separated to further suppress lateral and torsional modes.

(a)   (b)
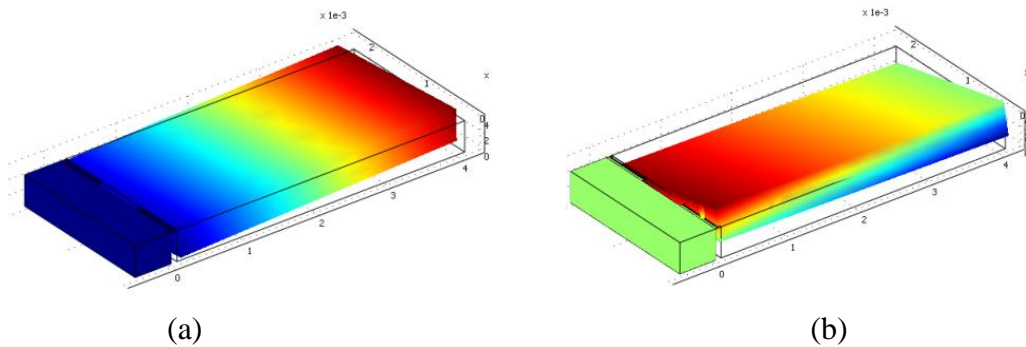
Figure. 4.5 Mode shapes of (a) lateral and (b) torsional vibration for piezoresistive accelerometer based on gapped cantilever structure. Resonant frequencies for these two modes are 15.4 kHz and 23.5 kHz respectively.

4.4 Fabrication

The fabrication process is carried out on 4" (100) SOI wafers purchased from MEMS Engineering & Material, Inc (Fremont, California). The p-type device layer has a thickness of

2.0 μm and a resistivity of 0.008~0.01 Ω·cm. The buried oxide layer and substrate layer are 2.0

μm and 420 μm thick, respectively. First, a 250 nm thick Au film was deposited by E-beam

evaporation with 20 nm Cr adhesion layer. This metal layer was then patterned to form the metal

traces and contact pads, as shown in Fig. 4.6 (a). In the next step, with a photoresist mask, DRIE

was used to etch the device layer to form the top piezoresistive beams, as shown in Fig. 4.6 (b).

In order to protect the accelerometer from shocks while handling and packaging, a 5-6 μm thick

parylene C layer was deposited on the front side of the wafer. This parylene layer was patterned

and etched by oxygen plasma using a thick photoresist mask layer. An etching window for the

bottom mechanical beam was opened in this step, as shown in Fig. 4.6 (c). The exposed SiO_2

was subsequently stripped by Buffered HF (BHF). Next, DRIE was carried out on the front side

of the wafer to etch the exposed area. The inset in step (d) shows a magnified view of the cavity

etched. The etching stopped when the remaining Si thickness was about 50 μm. Note that this

thickness was not accurately controlled due to the lack of an etch stop. However, this inaccuracy

of bottom beam thickness will not cause a large variation of the sensor performance. In the future

development, special SOI wafers with device layers on both sides can be used to accurately

control the thickness of the mechanical beam. Then the second DRIE was carried out from the

back side of the wafer as shown in step (e). The bottom beam was first shaped during this

etching. The DRIE stopped when the buried SiO_2 was reached. The SiO_2 layer was then

removed by BHF. Note that after this step, the proof mass was not completely free-standing

because of the protective parylene C layer. The device was glued on a printed circuit board

(PCB) and wire-bonded. It is worth noting that the top parylene C layer is critical during the

wire bonding process. Without this protective layer, the large shock generated during wire

bonding may destroy the accelerometer. The parylene C layer was removed by oxygen plasma

after the packaging process was finished. A photograph of a fabricated accelerometer is shown

in Fig. 4.7 (a). Note that parylene C layer was removed for clarity. The scanning electron

microscope (SEM) images of the fabricated devices are shown in Fig. 4.7 (b, c).
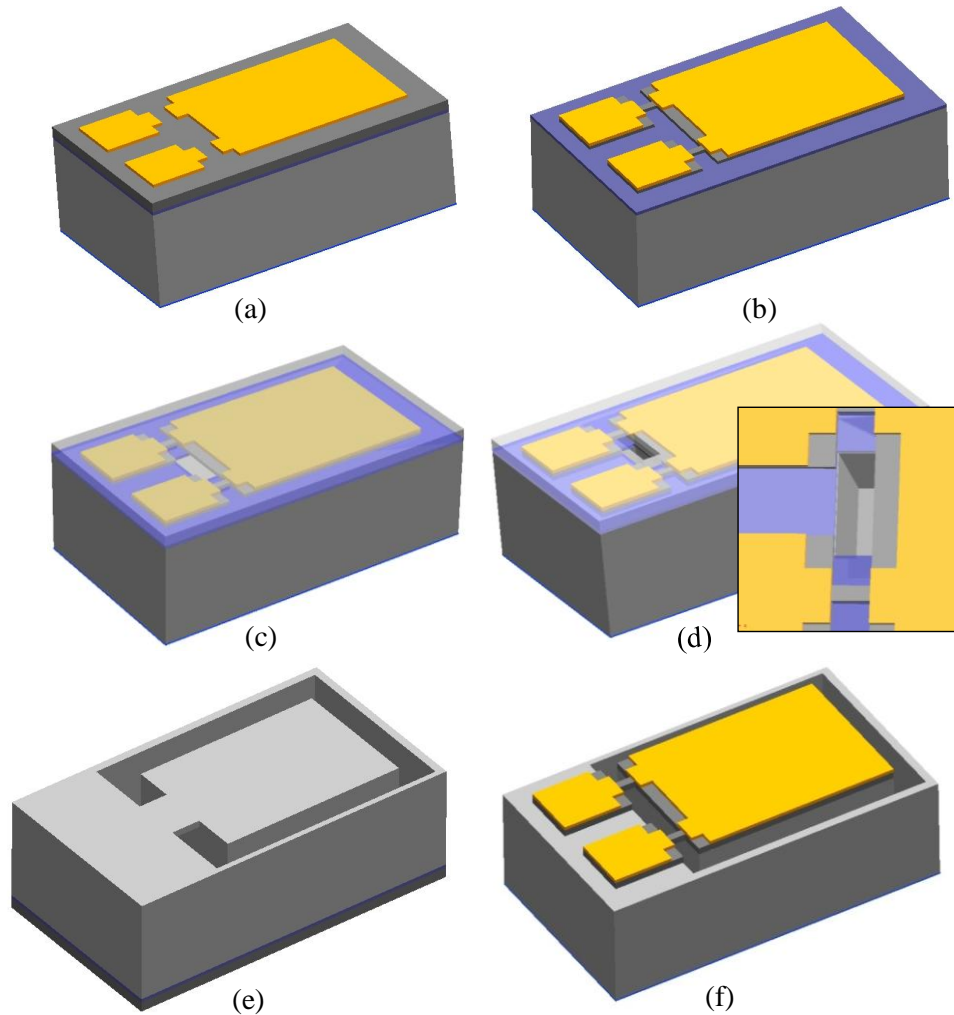
Figure 4.6. Simplified fabrication process of the accelerometer based on gapped cantilever: (a) deposit and pattern Au/Cr thin films on the SOI wafer; (b) pattern the device layer to form top piezoresistive beams; (c) deposit and pattern a parylene layer; strip the exposed oxide layer; (d) etch from the front side of the wafer using DRIE; (e) DRIE from the back side of the wafer (backside view); (f) top side view of the finished accelerometer (parylene layer is not shown for clarity).
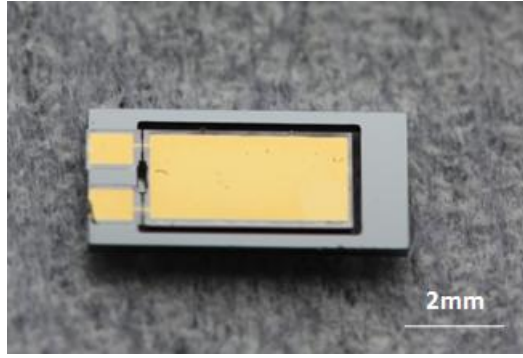
(a)
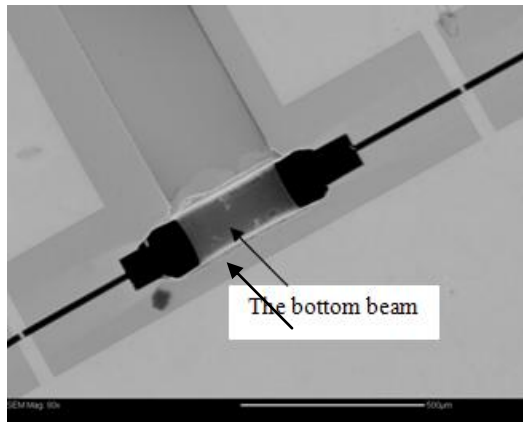
(b)
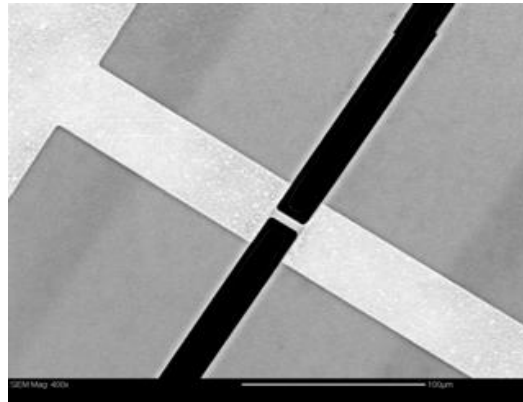
(c)

Figure 4.7. (a) Photograph of a fabricated device. (b) SEM image of one fabricated piezoresistive accelerometer based on an gapped cantilever. (c) Magnified view of one free-standing top piezoresistor.

4.5 Characterization

The packaged piezoresistive accelerometer was characterized using a mechanical shaker (Labworks, ET-126B) and a commercial accelerometer (Model 752A13, Endevco), as shown in Fig. 4.8. The dimension of the accelerometer under characterization is given in section 4.2.1. The nominal resistance of the piezoresistor is ~300 ohm. A Wheatstone bridge circuit was formed using two fixed resistors and one adjustable resistor. 5V dc supply voltage was used. The bridge voltage was tuned to zero by varying the resistance of the adjustable resistor. The output signal was first amplified by a pre-amplifier (Stanford Research SR560, with a noise spectral density of 4 nV/Hz$^{1/2}$ at 1 kHz) and then recorded by a data acquisition board (National Instrument NI 4461).
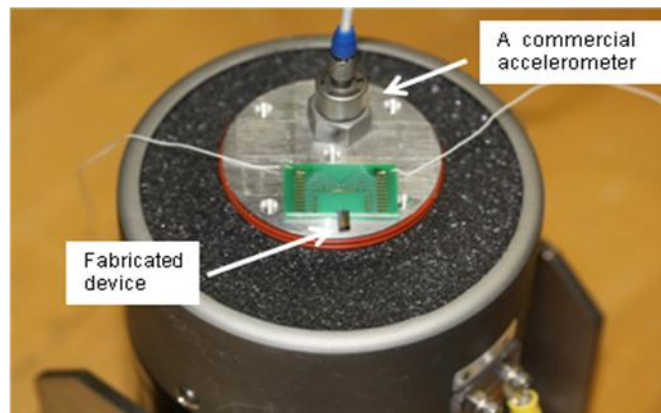
Figure 4.8. The packaged device was mounted on a mechanical shaker. A commercial accelerometer was used to calibrate the acceleration.

Figure 4.9 (a) shows the output voltage as a function of the amplitude of applied acceleration at 100Hz. The measured sensitivity is 0.36 mV/V/g. The frequency response of the accelerometer is shown in Fig. 4.9 (b). A resonant frequency of about 4060Hz was observed. If the piezoresistive coefficient is 32×10^{-11} N^2/m [4, 14], a sensitivity of 0.36 mV/V/g is equivalent

to a strain sensitivity of 2.7×10^{-5}/g in the piezoresistors. It can be observed that the experimental value of resonant frequency is less than the analytical value presented in Table 4.1. The main reason for this discrepancy is that we treated the top wide plates to which the piezoresistors are anchored as a rigid boundary in our analytical model. However, in the real case, these plates also experience mechanical strains, reducing the strain in the piezoresistors. The effect of elastic boundary was studied by finite element simulation using the actual Young's modulus of silicon in <110> direction (168 GPa) [13]. The results are presented in Fig. 4.4 and Table 4.1. It can be observed that the simulated resonant frequency based on soft boundary is 3.96 kHz, matching with the experimental value very well. However, the sensitivity is still lower than the simulation value. This discrepancy is likely because the actual piezoresistive coefficient is smaller than the value (32×10^{-11} N^2/m) which is used in our calculation. The piezoresistive coefficient may vary considerably depending on several factors including doping concentration, temperature and crystal orientation[4]. For instance, a temperature increase caused by self-heating of the piezoresistor will result in a decrease of the piezoresistive coefficient. In addition, it has been reported that the piezoresistive coefficient of silicon could be 33% lower than generally accepted value, probably simply due to material property variation [5]. In addition, the parasitic resistance connected in series with the piezoresistor may also contribute to the lower sensitivity.
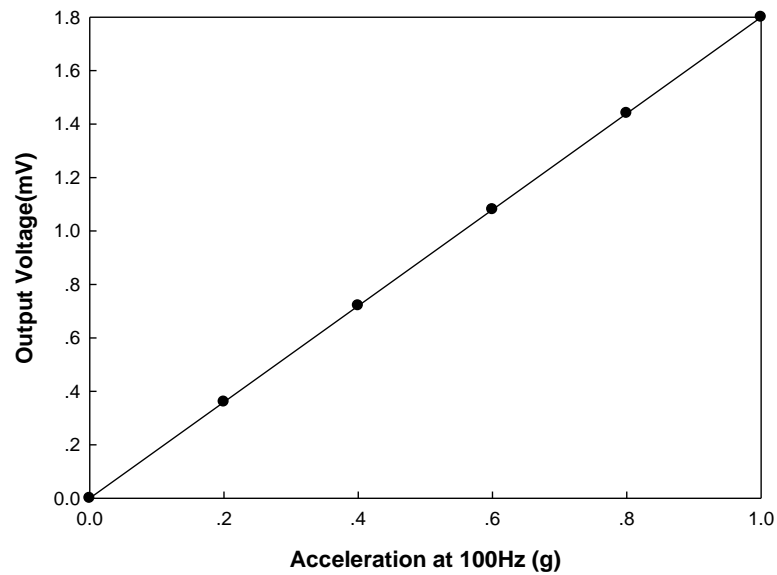
(a)
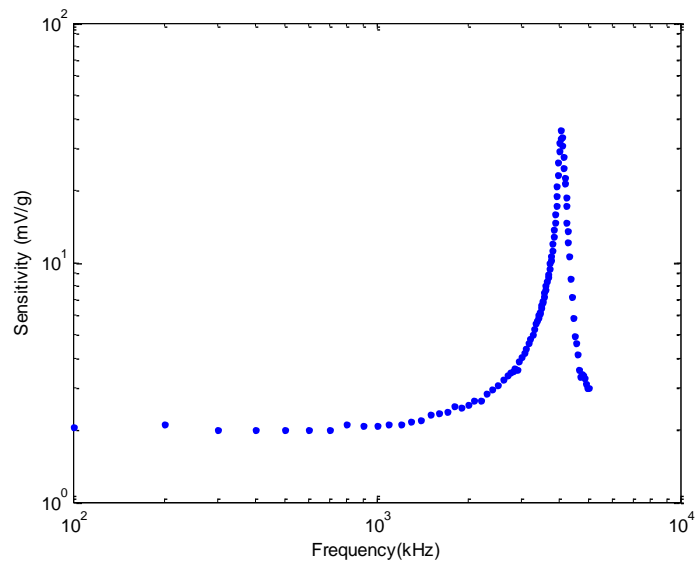
(b)

Figure 4.9. (a) Output voltage of the accelerometer as a function of acceleration at 100Hz with 5 V supply voltage. A sensitivity of 0.36 mV/V/g is observed with good linearity. (b) Frequency response of the accelerometer under 1 g acceleration. A resonant frequency of 4060Hz and a quality factor of 23 are measured.

The noise of the fabricated piezoresistive accelerometer was also measured. Figure 4.10 shows the measured noise spectral density. The dashed line shows the noise floor of the measurement system. This noise floor was measured by replacing the sensor with a low noise metal film resistor in the Wheatstone bridge. It is clearly observed that 1/f-like noise, with a frequency exponent n approximately equal to 1.4, is dominant at low frequencies. When $n \approx 1$, the origin of 1/f noise is generally considered to be conductivity fluctuation [16]. With $n>1$, other noise mechanisms such as current constriction are believed to play important roles [63, 64]. Assuming Eq. (4.4) is still valid, α_H of our device is 8.7×10^{-3}, which is at the upper end of reported Hooge factors of single crystal silicon (10^{-7} to 10^{-3}) [40, 63]. The larger noise is likely due to the excessive amount of defects in the device layer of the SOI wafer. It is reported that high temperature annealing could reduce 1/f or 1/f-like noise significantly [3, 40, 63]. The minimum detectable acceleration can be calculated based on the measured noise and sensitivity. With a bandwidth from 10 Hz to 1000 Hz, the minimum detectable acceleration based on the experimental results is 670 μg.
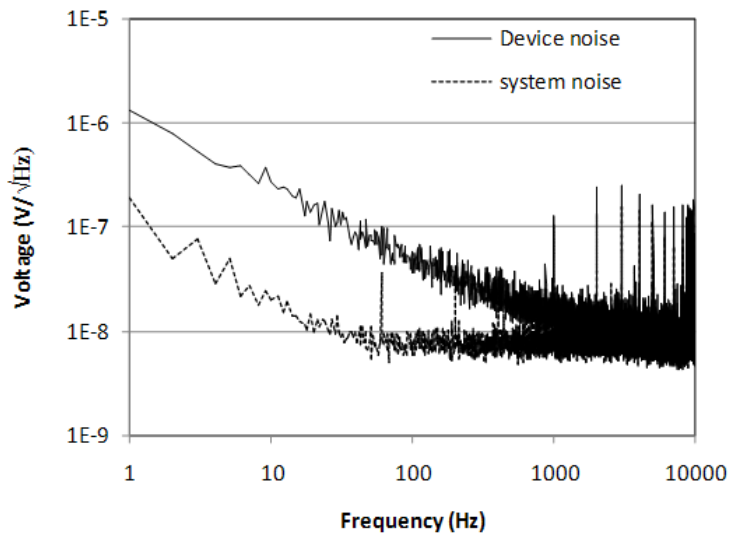
Figure 4.10. The measured noise spectral density ($V/\sqrt{Hz}$) of the piezoresistive accelerometer.

4.6 Summary

Micromachined piezoresistive accelerometer based on gapped cantilever structure is studied in this chapter. The accelerometer is designed in response to the requirements of continuous lung sound monitoring which is very important in clinical. The micro-scale prototype is designed and corresponding sensitivity and noise are discussed theoretically using the analytical model derived previously in chapter 2. Finite element simulation is also performed systematically to verify several important parameters such as average normal strain in piezoresistor and resonant frequency, etc. Higher resonant modes are proved to have little effect on the fundamental resonant mode for the proposed design as well using eigenfrequency analysis. The designed piezoresistive accelerometers are microfabricated using double-side DRIE process on SOI wafers. The developed accelerometers have been successfully characterized and the results show an agreement with analytical predictions and finite element simulations. In conclusion, the concept of micromachined piezoresistive accelerometer based on gapped cantilever structure is demonstrated. In the future, techniques (e.g., silicon islands on parylene membrane) which are able to make the accelerometer wearable will be investigated to finally make lung sound monitoring possible by using the accelerometer invented in this work.

CHAPTER 5. VIBRATION ENERGY HARVESTER

Vibration energy harvesting has attracted a great interest due to its various applications in both civilian and military fields, e.g. powering wireless sensor networks. Cantilever-mass structures are widely used in vibration energy harvesting devices. To convert the mechanical energy to electrical energy, a layer of piezoelectric material is usually fabricated on the surface of the cantilever or the cantilever itself is a piezoelectric bimorph. The AC voltage generated usually needs to be converted to DC voltage before it can be used to power the following circuits. Therefore, it is always desirable to increase the voltage and power output of a piezoelectric vibration energy harvester. Vibration energy harvester based on gapped cantilever structure is proposed in this work by taking the advantage of high voltage sensitivity and high energy conversion efficiency of gapped cantilever structure.

5.1 Introduction

5.1.1 Tire pressure monitoring system (TPMS)

This work is pursued in response to a new federal rule (Federal Moving Vehicle Safety Standard 138) mandating that every passenger vehicle sold in the U.S. market after January 1st, 2008 should be equipped with Tire Pressure Monitoring Sensors (TPMS) on every tire. The ruling further mandates that only direct measurement systems that monitor all four tires simultaneously to detect under-inflation of 25% or more of recommended pressure be utilized. This means that every tire including the spare contains a TPMS and each TPMS requires a power source, mainly batteries.

Currently TPMS power sources contain a finite amount of energy, and based on manufacturer's own early estimates, are expected to last as few as 6 years in this

application. This can present a conundrum for the vehicle owners at the time of battery failure. TPMS batteries are not rechargeable and the vast majority of the devices on the market do not allow for the replacement of these batteries. Because of the less than ideal environment inside tires, the pressure sensor and surrounding electronics are protected with the use of a material that makes it impossible to replace any components within the TPMS device. Owners will have to decide whether they will replace the TPMS devices at a cost of as much as $240 per tire or $1200 for all tires, including the spare, or forego the use of a mandated safety feature that they have become accustomed to. So customers will be forced to live without this technology or pay a lot of money for replacement devices because of a battery that would cost the consumer at most $3.00 a piece at the local Radio Shack. Lithium batteries are considered a hazardous material and must be disposed of properly. Based on information obtained from engineers within Ford and General Motors (GM), automakers are actively searching for alternatives to the lithium battery because of the potential warranty issues, potential customer backlash, and potential litigation that could occur because of battery failure as well as the environmental issues caused by the use of lithium.

Generally alternative power sources for battery-less TPMS [65] can be grouped into three categories. The first method is based on back scatter technology, which has been used for RFID. In this method, readers are mounted on chassis. The RF signal sent by readers is reflected back and modulated by the pressure signal. In the second method, the power is transmitted to TPMS module wirelessly, e.g., using low frequency (LF) electromagnetic wave. In the third category, the energy is scavenged from the environment, including vibration energy scavenging and thermal energy scavenging based on thermoelectricity. The following table is a comparison of different approaches[65]. Freescale, a major TPMS supplier, concludes that the vibration energy

harvesting device based on piezoelectric material is the most promising solution [65]. This is mainly because the automotive industry is extremely sensitive to cost. The piezoelectric vibration harvesting device is so far the lowest cost battery-less solution. It is also the least disruptive to the current TPMS module production process. In addition, installation is not complicated by any chassis mounted devices at each wheel location, reducing labor cost.

Table 5.1. Comparison of different power approaches for TPMS (adapted from [65])

	Battery	Piezoelectric	Thermal	LF power	Back-scatter
Total system cost	$42	$50	$54	$58	$80
Replacement Interval	6-10 years	Life of car	Life of car	Life of car	Life of car
Consumer Life Cycle Cost	$204-1164	$100	$108	$116	$160

5.1.2 Advantage of gapped cantilever for TPMS

To make satisfactory vibration energy harvesting devices for TPMS, two conflicting challenges have to be addressed simultaneously. First, the power generated by the vibration energy harvesting devices needs to be large enough. According to [65], it takes 21.9 μJ, 6.54 μJ and 258.3 μJ to make, process and transmit one measurement. Tire Pressure Monitor Global SSLT Workgroup of General Motor specifies that the TPS shall measure the tire pressure at least once every 30 seconds. Therefore, the power harvested needs to be >10 μW. Second, the device has to be robust enough to withstand the huge shock acceleration and large centrifugal acceleration inside a fast-spinning tire. This poses a unique challenge on vibration energy harvesting for TPMS. Since at one hand, a large spring constant is required to withstand this acceleration; but on the other hand, this large spring constant considerably decreases the power level.

(a) Bimorph structure   (b) Unimorph structure
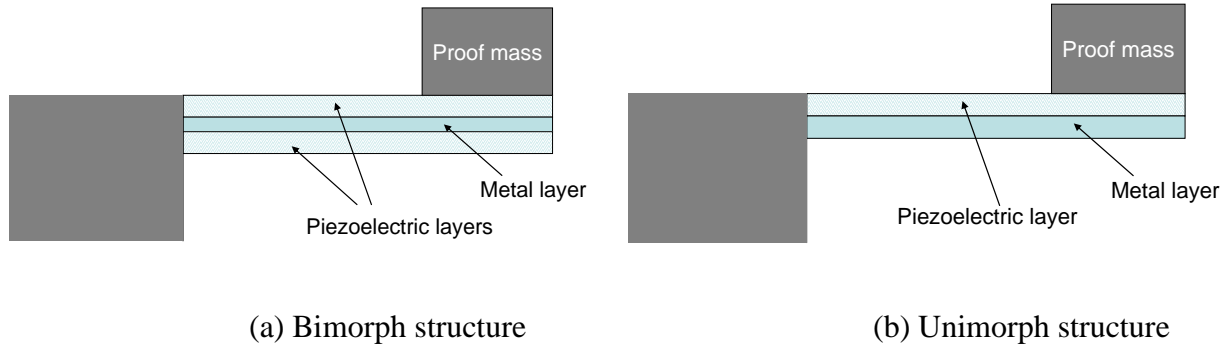
Figure 5.1. Conventional vibration energy harvesting devices based on piezoelectric bimorph and unimorph cantilevers. One end of the cantilever is fixed. The other end is attached with a proof mass.

Vibration energy harvesting devices based on conventional piezoelectric bimorph or unimorph cantilevers[66-71] [72-80] as shown in Fig. 5.1 are used to explain the challenges for TPMS. When there is a vibration, the proof mass will oscillate up and down, straining the piezoelectric material. The piezoelectric material then converts the mechanical strain to electrical energy, by generating electrical charges on its top and bottom surfaces. If the amplitude of the external vibration is constant, the power generated is proportional to frequency of the vibration and the proof mass, and inversely proportional to the spring constant. Due to the space and weight constraint of TPMS, the proof mass is limited and thus can not be too large. At the same time, the spring constant needs to be large enough to withstand the huge accelerations inside tires. However, this large spring constant reduces the output power.

Please note that there is a large centrifugal acceleration (up to ~400g under normal driving condition) inside tires when the vehicle is running. But the majority of this acceleration is a constant component, leading to no energy harvesting. Only the variation of the acceleration (e.g., due to gravity) can be used to generate electricity. The frequency of this variation is same

as the rotation rate of the tire, which is usually between 10-20 Hz. This is a fairly low frequency, which makes it even more challenging to meet the power requirement of TPMS.

It is also worth noting that when operating at resonant frequency, the amplitude of the proof mass vibration will be much larger and thus the power generated will be much higher. Therefore, most vibration energy harvesting devices are designed to operate at resonant frequency. Nevertheless, it is not possible in the case of TPMS, where the majority energy of the vibration is between 10Hz~20Hz. To make it robust enough, the energy harvesting device needs to be very rigid. Consequently, the resonant frequency is chosen around 1000 Hz, far beyond 10-20 Hz. Therefore, the vibration energy harvesting device for TPMS has to operate far below the resonant frequency. This is a significant difference compared with most other vibration energy harvesting devices developed so far.

(a)   (b)
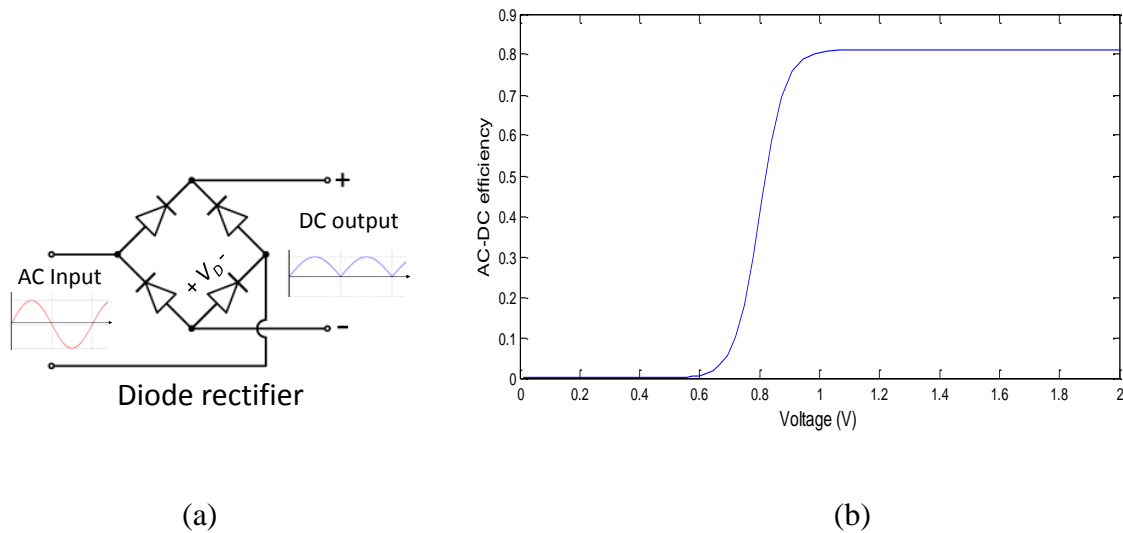
Figure 5.2. (a) A full-wave rectifier (bridge rectifier); (b) AC-DC efficiency of a full-wave rectifier as a function of the amplitude of the input AC voltage for typical diodes (I_s=10-14 A, n=1.5, R_L=1kohm. V_T=0.026V).

This power problem is further worsened by the fact that the AC voltage usually needs to be converted to DC voltage in order to power the following circuits/sensors. This is usually done by a diode rectifier as shown in Fig 5.2. (a). This AC-DC conversion efficiency could be far below 100% when the amplitude of the AC voltage is small. For a simplified model, $\eta_{AC\text{-}DC}$ of a full-wave diode rectifier can be estimated using the following equation:

$$\eta_{AC-DC} = 0.812/[1+\frac{R_d}{R_L}] \tag{5.1}$$

where R_L is the load resistance, R_d is the diode resistance.

As shown in Fig. 5.2 (b), the AC-DC conversion efficiency of diode rectifier quickly drops to almost zero when the amplitude is below a threshold voltage. Accordingly, the converted DC power will be very small. This could be a serious issue. Many researchers are starting to look into this issue. For example, one approach is to develop rectifiers with almost zero forward drop voltage ($V_D \cong 0$) [81, 82]. However, these rectifiers are active circuits that need to be powered during operation. In many cases, the power consumed by these active circuits is even larger than the power harvested. Therefore, the ideal approach is to increase V_I.

Another big issue is the reliability since the energy harvesting device inside the tire is subject to huge accelerations. For example, the centrifugal acceleration can be as large as 650g. The weakest link is usually the piezoelectric material (e.g., PZT). The fracture strain of PZT when it is stretched is about 500 microstrain (500×10^{-6}). But when PZT is compressed, the fracture strain is at least 5 times larger. Therefore, it is more robust for the PZT to operate in the compression mode. But for the conventional bimorph structure, there must be one PZT layer being stretched no matter how the proof mass displaces. Unimorph, with one piezoelectric and

one metal layer, is more robust. But more than 50% of the mechanical energy is wasted to strain the metal layer.

5.2 Design

The schematic vibration energy harvester based on asymmetric gapped cantilever structure is shown in Fig. 5.3. The composite cantilever consists of a top piezoelectric layer and a bottom mechanical layer, separated by an air gap. With such structures, the AC voltage generated will be significantly higher due to the increased distance between the piezoelectric layer and neutral plane. Therefore, the AC to DC conversion efficiency is increased significantly. Interestingly, the mechanical to electrical energy conversion efficiency is also improved because gapped cantilevers enable the majority of the strain energy to stretch/compress the piezoelectric layer. Furthermore, the asymmetric structure allows the piezoelectric layer to operate in the compression mode when the centrifugal acceleration is applied in the upward direction. Therefore this design will be more robust than the bimorph structure.

The design parameters of vibration energy harvester in this work are as follow: $w_1=15$ mm, $t_1=0.9$ mm, $l_1=8$ mm, $w_2=5$ mm, $t_2=0.502$ mm, $l_2=8$mm, $w_m=15$ mm, $t_m=3$ mm, $l_m=30$mm, $E_1=E_m=200$Gpa and $E_2=66$Gpa, $\rho_1=\rho_m=8000$ kg/m^3 and $\rho_2=7800$ kg/m^3. Note that in this design, top piezoelectric beam and bottom mechanical beam have same lengths. Based on analytical model the spring constant, average normal strain on top piezoelectric beam and resonant frequency of vertical vibration are calculated. The results are summarized in Table 5.2 along with corresponding simulation results.
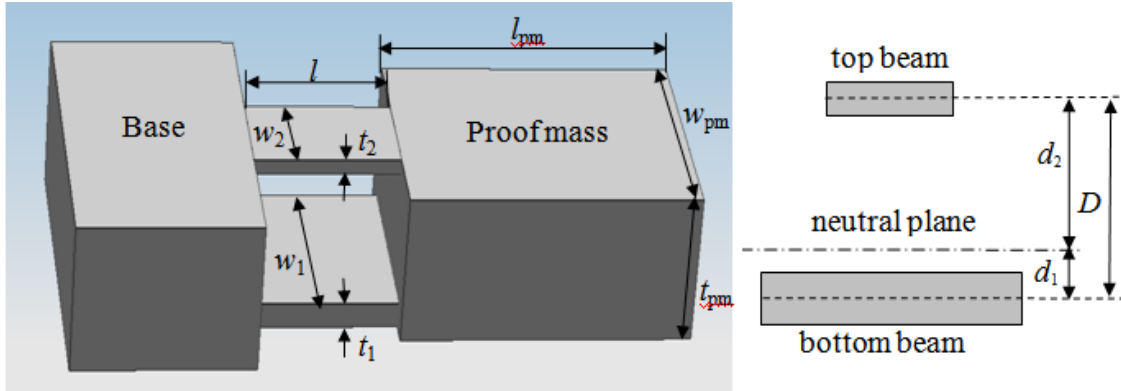
Figure 5.3. Schematic structure of vibration energy harvester based on gapped cantilever structure.

5.3 Finite element simulation

A fast finite element simulation is performed to completely evaluate the performance of the designed gapped cantilever vibration energy harvester. As discussed in chapter 3, simulations with ideal assumptions, simulations without assumptions and eigenfrequency analysis are all conducted. All the results are summarized in Table 5.2 along with corresponding analytical results.

Table 5.2 Simulation and analytical results for designed vibration energy harvester based on gapped cantilever structure. Simulations are performed both with and without ideal assumptions. Eigenfrequency analysis is also performed to find out resonant frequencies of torsional and lateral vibration modes.

	Simulation with assumptions	Simulation without assumptions	Analytical
Spring constant (N/m)	3.22×10^4	2.96×10^4	3.24×10^4
Strain on top beam	4.42×10^{-6}	$4.39. \times 10^{-6}$	4.40×10^{-6}
Vertical resonant frequency (Hz)	800	757	803
Torsional resonant frequency (Hz)	4070	3676	N/A
Lateral resonant frequency (Hz)	5750	5598	N/A

As we can see from the tables above, when ideal assumptions are adopted in the simulation, spring constant, average normal strain and resonant frequency of the first mode (vertical) match really well with theoretical calculations. Meanwhile, even though same parameters from simulation without those assumptions show larger discrepancy from analytical results, the differences are still within acceptable range (less than 10%). We can also observe from the eigenfrequency analysis results that the resonant frequencies of higher resonant modes (torsional and lateral) are far above the first resonant mode (vertical). Therefore, the vertical vibration which will be mainly used to harvest energy is dominant for the designed device. An illustration of the deformed energy harvester from simulation is shown in Fig. 5.4.
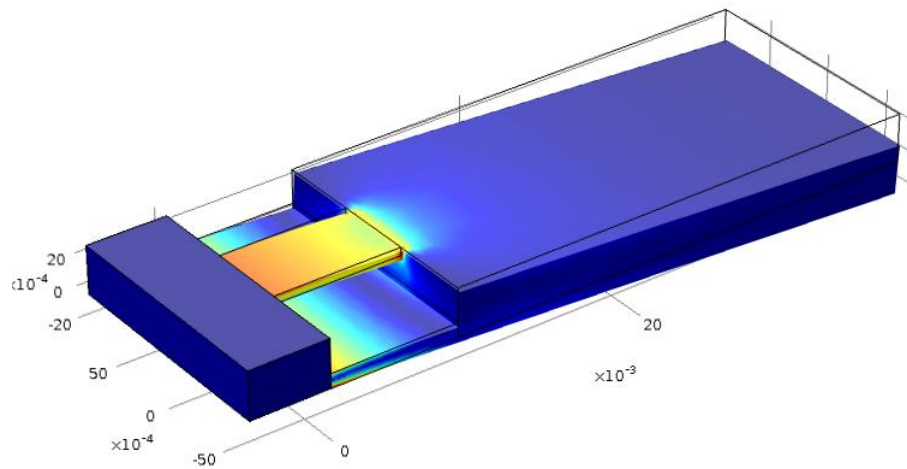
Figure 5.4. Illustration of the deformed vibration energy harvester from simulation result.

5.3 Bench-top characterization

A prototype vibration energy harvester based on gapped cantilever structure is developed using PZT sheets (T105-A4E-602) purchased from Piezo System, Inc., Cambridge, MA, USA. The piezoelectric coefficient d_{31} is equal to -190×10^{-12} meters/volt. The Young's modulus E_1 is 66GPa. The relative dielectric constant is 1800 (at 1 kHz). The base, the bottom beam and the

proof mass is machined together using one piece of stainless steel. Then, the top PZT layer is glued onto the base/bottom beam/proof mass combined metal piece using conductive epoxy. Another separate stainless steel mass will be glued onto the proof mass if it's necessary to increase the mass of the proof mass. The resulting gapped cantilever energy harvester is shown in Fig.5.5. The device is mounted to a mechanical shaker, which is used to generate mechanical vibrations. A commercial accelerometer (Model 752A13 isominTM, Endevco, CA, USA) is attached to the base to measure the acceleration generated by the shaker. Sinusoidal signals are applied to the shaker at various frequencies.
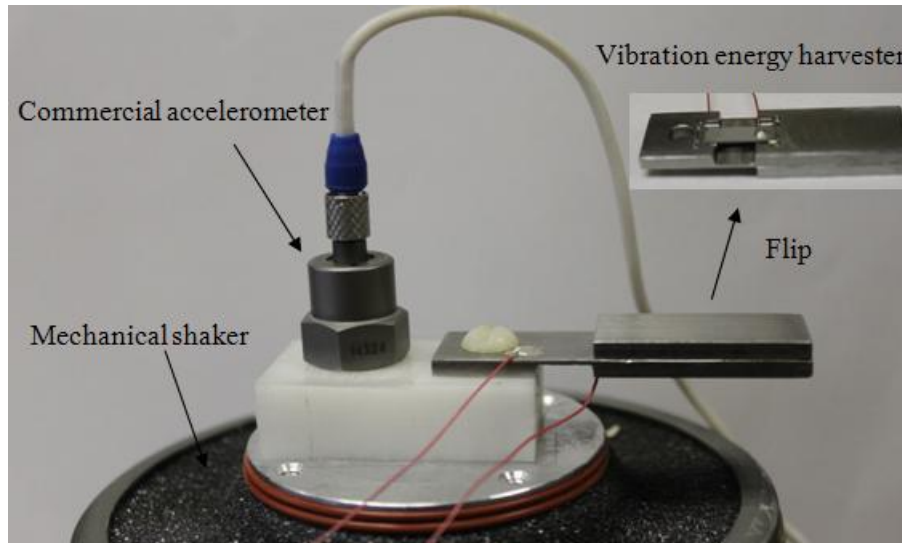
Figure 5.5. Picture of a prototype vibration energy harvester up-side-down mounted on a mechanical shaker. Commercial accelerometer is also attached to the shaker for calibration purpose.

When the mechanical shaker vibrates in vertical direction, the vibration energy harvester also vibrates generating a sinusoidal voltage between top and bottom surfaces of the PZT sheet. The voltage sensitivity (V/g) at low frequency can be easily calculated since the expression of average normal strain in the top piezoelectric beam ε_2 is already known by Eq. (2.57):

$$V/a = \frac{\lambda d_{31}}{\varepsilon_0 \varepsilon_3} \varepsilon_2 E_2 t_2 \tag{5.2}$$

where d_{31} is the piezoelectric coefficient, ε_3 is the relative dielectric constant of PZT in direction 3, ε_0 is vacuum permittivity, and $\lambda = l/l_T$ (l_T is the total length of the diced PZT) is a coefficient which is used to compensate the parasitic PZT capacitances on the base and the proof mass. The voltage sensitivity versus frequency is plotted in Fig. 5.6 based on bench-top characterization results. As we can see, the voltage sensitivity is 1.81 V/g at low frequency, and it is close to the theoretical one calculated by Eq. (5.3) which is 1.97 V/g. In addition, we can find that the resonant frequency of the device is 354 Hz, and this is about 25% lower than the theoretical resonant frequency of 471 Hz calculated by Eq. (2.63). Note that some of the geometric parameters are modified from the design in section 5.2 based on the real device geometry, and consequently the two parameters theoretically calculated above are different from the simulation results shown in sections 5.3 as well.
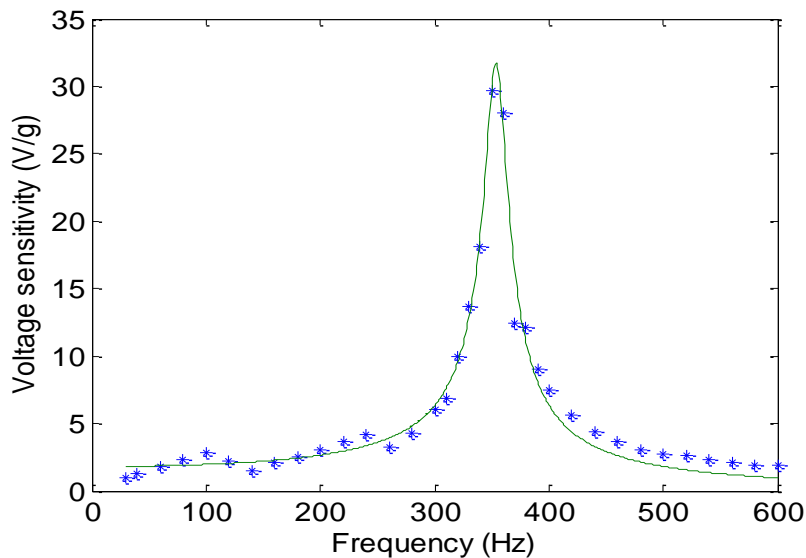
Figure 5.6. Output voltage sensitivity of the vibration energy harvester as a function of frequency.

There are several possible reasons for the discrepancy between experimental results and theoretical calculations. First, the real spring constant is smaller than the theoretical one since the proof mass is also subject to deformation in the experiment which was ignored in the analytical model. Second, the mass of the system is larger than theoretical one since we didn't consider the mass of the mechanical beam and PZT layer in the analytical model. Last, the bonding is not perfectly rigid, possibly leading to softening effect of the boundary.

5.4 Road test

This prototype vibration energy harvester is also road-tested to practically inspect the feasibility of harvesting energy from tire vibrations. This test also allows us to find out any possible problems of the gapped vibration energy harvester and consequently improve the design in the future.

5.4.1 Single device

A single device test is first conducted on a vehicle (2003 Mazda Tribute) as planned. The assembly is shown in Fig. 5.7. The vibration energy harvester is mounted on the wheel up-side-down to make sure the PZT operates in compression mode. The wiring to the rotary assembly on the wheel is achieved using a slip-ring from Michigan Scientific. The two lead wires from the energy harvester are connected to the "rotor" of the slip-ring. There is an internal mechanism to electrically connect the terminals on the "rotor" to the "stator". Then the signals from the "stator" are wired out through the aluminum tube and recorded by a USB-based data acquisition board (NI USB 6210) controlled by a laptop computer.
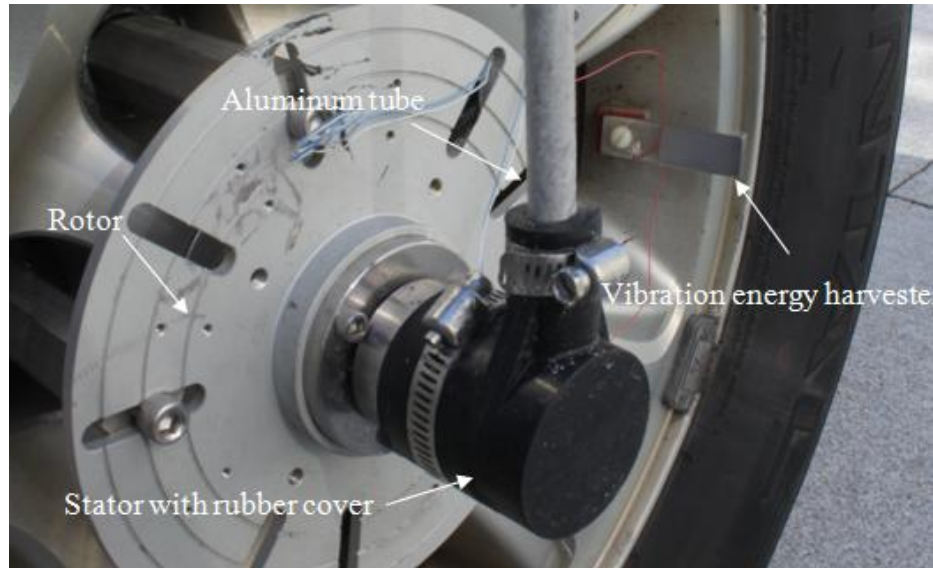
Figure 5.7. The road test assembly on the wheel for a single device test.

Two sets of experiments with different driving speeds and different weights of the proof mass are carried out, and the power spectral density of the output voltage from the device is plotted in Figs. 5.8 and 5.9. As we can see in the figures, there are two peaks in the power spectrum plot. It is obvious that the first peak at low frequency relative to the rotation rate of the tire, i.e., 11 Hz peak in Fig. 5.8 is corresponding to a driving speed of 55 mph and 6 Hz in Fig. 5.9 is corresponding to a driving speed of 30 mph. The second peak at high frequency represents to the resonant frequency of the device. Since resonant frequency is inversely proportional to the square root of mass (Eq. (2.63)), 470 Hz peak in Fig. 5.8 is corresponding to mass weight of 10.8 gram and 340 Hz peak in Fig. 5.9 is corresponding to mass weight of 21.6 gram.
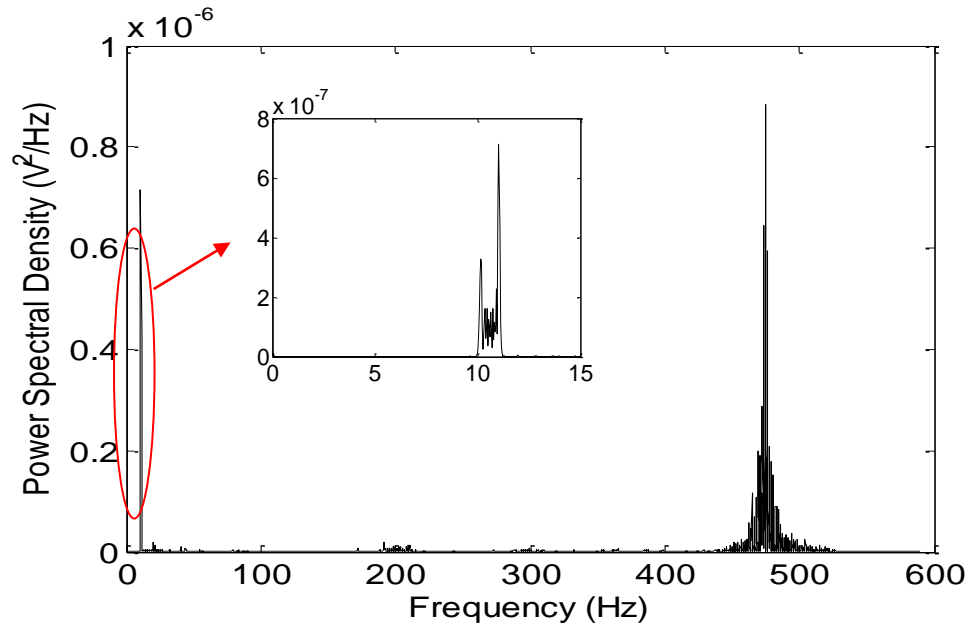
Figure 5.8. Power spectral density of the output voltage in road test when driving speed is 55 mph and proof mass is 10.8 gram. Two peaks: 11 Hz (inset) and 475 Hz
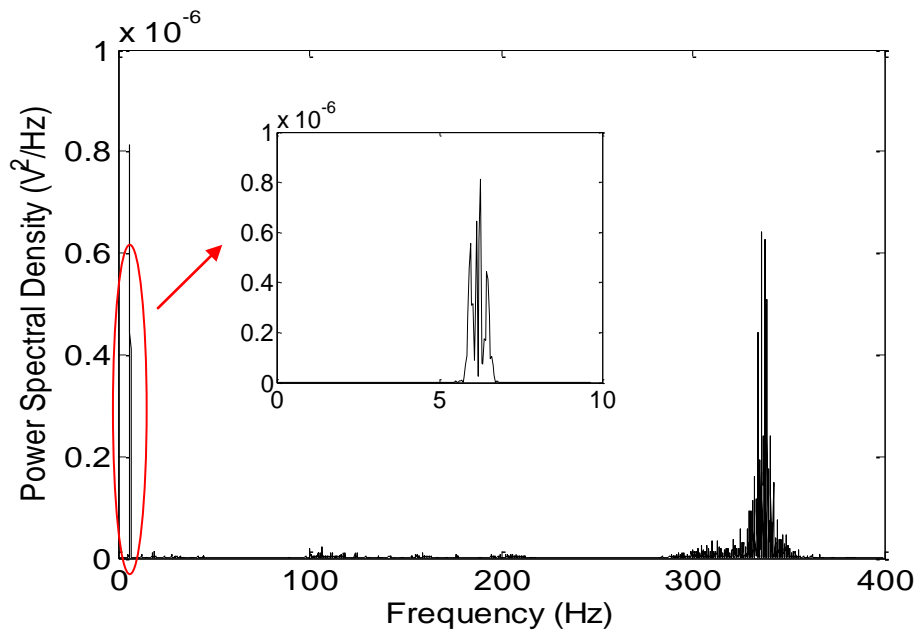
Figure 5.9. Power spectral density of the output voltage in road test when driving speed is 30 mph and the proof mass is 21.6 gram. Two peaks: 6 Hz (inset) and 336 Hz

The voltage generated by the vibration energy harvester is used to charge a 32 μF capacitor through a bridge rectifier. The result of the capacitor voltage charged by energy harvester with ~50 mph driving speed and 21.6 gram of proof mass is shown in Fig. 5.10. As we can see in the figure, it takes about 35 seconds to charge the capacitor to around 8 V, and the maximum power is calculated to be 47 μW. Inset shows the magnified view of the charging waveform at 60s.
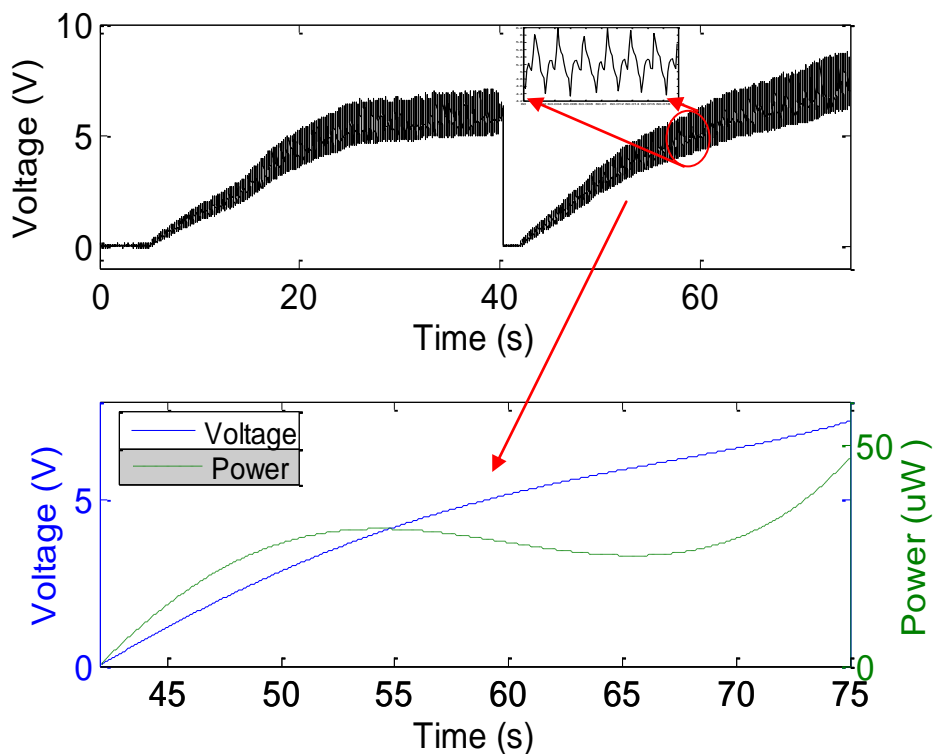
Figure 5.10. Top: the voltage of a 32 μF capacitor charged by the energy harvester. Bottom: fitted voltage of one charging cycle and corresponding power. Driving speed is ~50 mph, and the mass of the proof mass is 21.6 gram. Inset shows the magnified charging waveform.

5.4.2 Double device.

The road test performed previously harvested energy of a vibration in centrifugal direction. In order to explore the potential of harvesting energy by vibration in tangential direction, another set of experiment is performed additionally. In this experiment, two identical

vibration energy harvesters (w_1=15 mm, t_1=0.9 mm, l_1=8 mm, w_2=5 mm, t_2=0.502 mm, l_2=8mm, w_{pm}=15 mm, t_{pm}=6 mm, l_{pm}=30mm, E_1= E_{pm}=200Gpa and E_2=66Gpa.) are developed and simultaneously used to harvest energy from centrifugal and tangential vibrations respectively to make a reasonable comparison between these two modes.

The two vibration energy harvesters are bench-top characterized first. As shown in Fig. 5.11, the resonant frequency and sensitivity of the two harvesters match really well (2% and 10% difference). The road test is performed on the same vehicle (2003 Mazda Tribute). The new assembly is shown in Fig. 5.12 The two vibration energy harvesters are mounted in two different directions (centrifugal and tangential) on the same plastic base which is glued on the wheel. Wires and a slip-ring are again used to transfer signals from the harvesters to the laptop in vehicle.
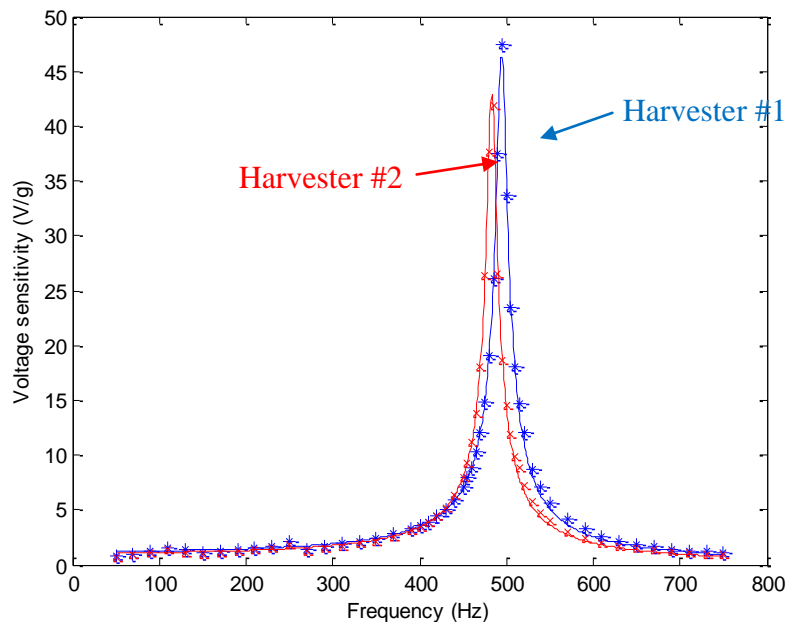
Figure 5.11. Frequency response of two identically designed vibration energy harvesters. Harvester #1 has resonant frequency of 494 Hz and sensitivity of 1.21 V/g, and harvester #2 has resonant frequency of 483 Hz and sensitivity of 1.08 V/g.
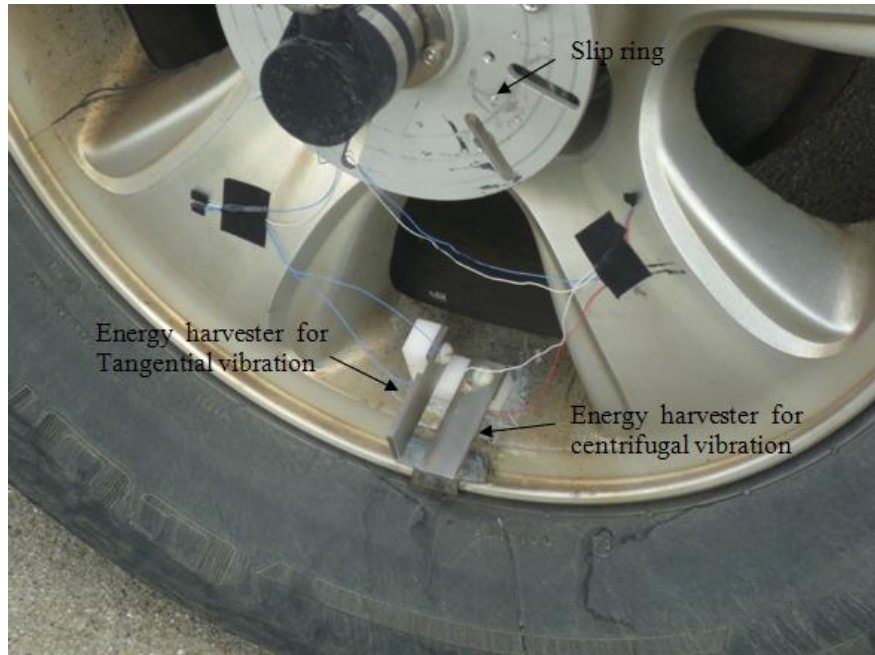
Figure 5.12. The road test assembly on the wheel for centrifugal and tangential vibration simultaneously.
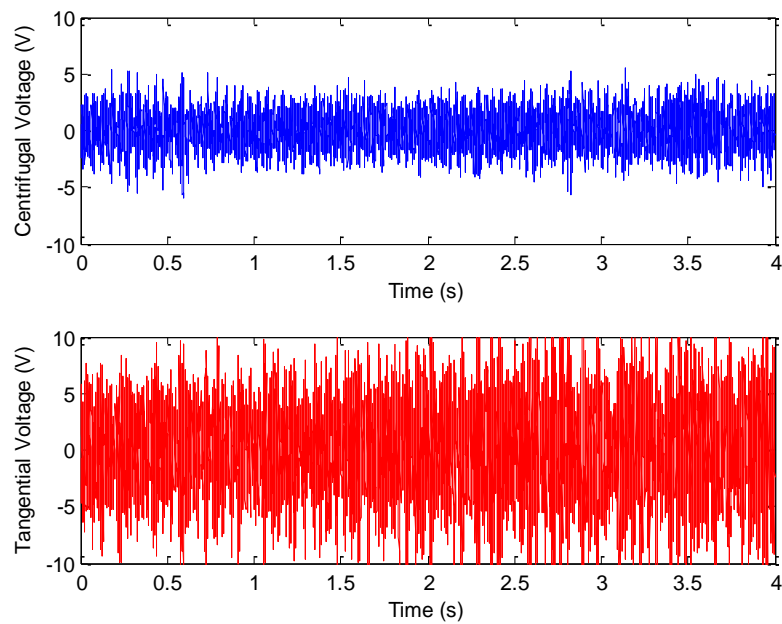
Figure 5.13. Voltages from the harvesters measuring centrifugal vibration and tangential vibration respectively. RMS voltages of centrifugal and tangential signals are 1.4 V and 3.8 V respectively.

The voltages from the two harvesters are recorded simultaneously. Figure 5.13 shows the voltages of the harvesters in centrifugal and tangential directions respectively at a vehicle speed of 50 mph. It is interesting to note that the RMS voltage of the harvester vibrating in tangential direction is 3.8 V which is more than twice of the RMS voltage of 1.4 V from the harvester vibrating in centrifugal direction. This result indicates that the vibration energy harvesting is more efficient in tangential direction of the tire than in centrifugal direction.

In order to further verify the higher efficiency of tangential vibration mode, the two harvesters are also used to charge capacitors with same capacitance (32 μF) through identical bridge rectifiers. Voltages across the two capacitors are monitored during charging process, and the results are shown in Fig. 5.14. As we can see, the capacitor connected to the harvester in tangential mode is charged faster to a higher saturation voltage compared to the other. By means of excluding the errors induced by non-identical capacitors and rectifier circuits, the two connection lines from harvesters to charging circuits are switched to each other in the next test. As can be seen from the switched charging voltages shown in Fig. 5.15, similar results are obtained. In conclusion, the vibration energy in tangential direction of the tire is higher than the energy in centrifugal direction, hence it is more efficient to harvest energy from the vibration in tangential direction in the tire for TPMS.
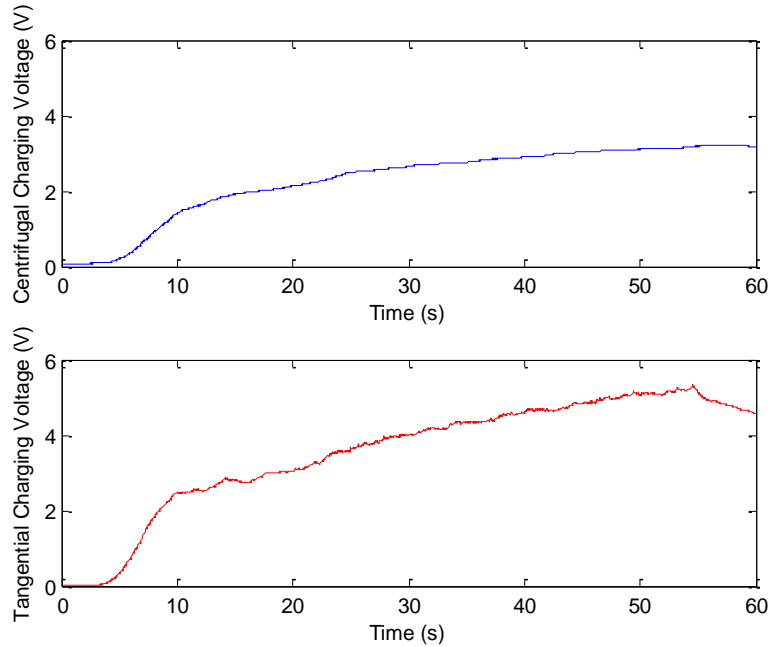
Figure 5.14. The voltage of a 32 µF capacitor charged by the vibration energy harvesters for vibration in centrifugal and tangential directions respectively.
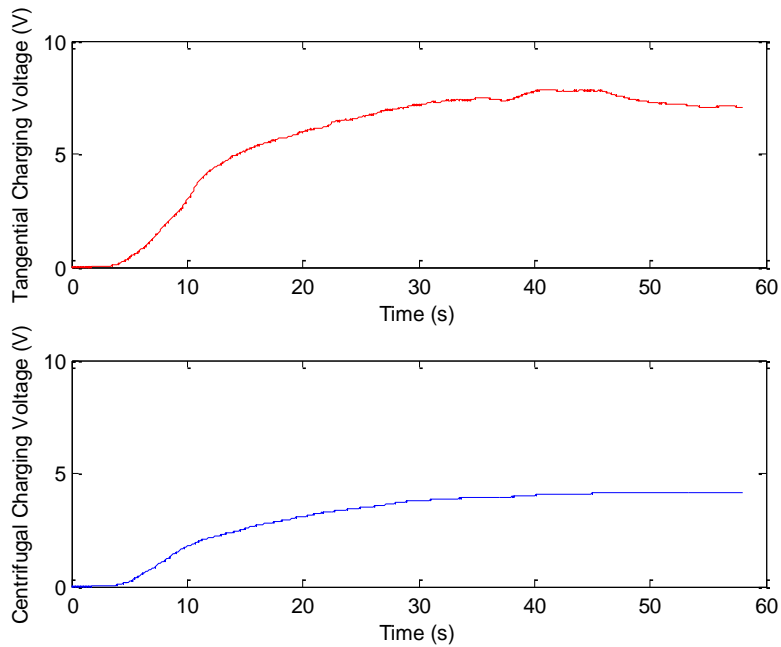
Figure 5.15. The voltages of 32 µF capacitors charged by the vibration energy harvesters for vibration in tangential and centrifugal directions respectively after the charging lines are switched.

5.5 Summary

In this chapter, vibration energy harvester based on gapped cantilever structure is studied. Among many applications of vibration energy harvester, the design in this work is specifically targeted to power tire pressure monitoring system on vehicles. Finite element simulations are performed to verify the harvester design. Prototype vibration energy harvesters are developed and tested both in the lab and on the road respectively. The output voltage sensitivity and resonant frequency from bench-top characterization show good agreement with theoretical values calculated using our analytical model. The road test results show the device is able to produce a as large as 8 V absolute voltage and 47 μW power, which preliminarily demonstrated the feasibility of powering tire pressure monitoring system using vibration energy harvester based on gapped cantilever structure. Another road test is performed using two identical prototype harvesters simultaneously to compare the vibration energy for different directions in the tire. The results interestingly indicate that the vibration energy in tangential direction is much higher than the vibration energy in centrifugal direction.

CHAPTER 6. RESONANT MASS SENSOR

In this chapter, the resonant mass sensor based on gapped cantilever structure is investigated. Theoretically, the gapped structure is advantageous in resonant mass sensing due to increased displacement sensitivity. A meso-scale prototype is first developed and tested to prove the concept of gapped cantilever mass sensor. Later, a micro-scale prototype is designed, fabricated and preliminarily tested.

6.1 Introduction

Recently, resonant mass sensors based on MEMS/NEMS (Micro or Nano-Electro-Mechanical Systems) cantilevers have attracted a lot of attention and many exciting results have been reported [83-95]. For these resonant mass sensors, one critical component is the transducer that detects the vibration of the cantilever. Optical methods such as laser Doppler vibrometer, interferometry and optical lever technique seem to be the most popular choice because they offer very high displacement sensitivity and make the microfabrication of cantilevers very simple [83-85, 87] [86, 89, 90]. However, the overall system becomes expensive, bulky, and not very portable although the cantilever resonator itself is very small. Furthermore, these methods become insensitive when the dimension enters nanometer regime due to diffraction issue. Piezoresisitvity and piezoelectricity are another two well-developed sensing mechanisms. Their advantages include low cost, simplicity and on-chip integration that may lead to a portable system. A number of piezoresistive and piezoelectric cantilevers have already been developed for resonant mass sensing [88, 92-95]. To improve the performance of the resonant mass sensor, it is highly desirable to increase the sensitivity of piezoresistive and piezoelectric sensing.

Therefore, we proposed resonant mass sensor based on gapped cantilever structure as well to achieve higher sensitivity in this work.

6. 2 Design

Based on concentrated mass model, the resonant frequency of a mechanical resonator is

$$f_0 = \frac{1}{2\pi} \sqrt{\frac{k}{M_{\text{eff}}}} ,$$

(6.1)

where k is the spring constant and M_{eff} is the effective mass of the resonator. When there is a mass change ΔM, a resonant frequency change Δf can be observed:

$$\Delta f \approx -\frac{1}{2} \frac{f_0}{M} \Delta M$$

(6.2)

Therefore, the mass change can be detected by measuring the resonant frequency shift. If the noise is white, following the procedure reported in [96], the minimum detectable mass of the resonant sensor can be expressed as,

$$\Delta M_{\text{min}} \approx \frac{\sqrt{2\pi} M_{\text{eff}}}{Q} \frac{v_{\text{noise}}}{v_{\text{carrier}}}$$

(6.3)

where v_{carrier} is the carrier voltage (RMS) of the resonator, v_{noise} is the noise voltage, and Q is the quality factor of the resonator. Note that the above three equations are generic and valid for various resonant mass sensors.

The basic structure of the proposed resonant mass sensor in this work is schematically shown in Fig. 6.1. Similar to previous applications of gapped cantilever structure, the supporting beam is an asymmetrically gapped cantilever, consisting of a bottom mechanical layer (gray

color) and a top sensing layer (red color) separated by a gap. The sensing layer can either be piezoresistive or piezoelectric. The proof mass is designed as hollow to reduce the mass, since smaller proof mass makes the device more sensitive to mass change.

(a)   (b)
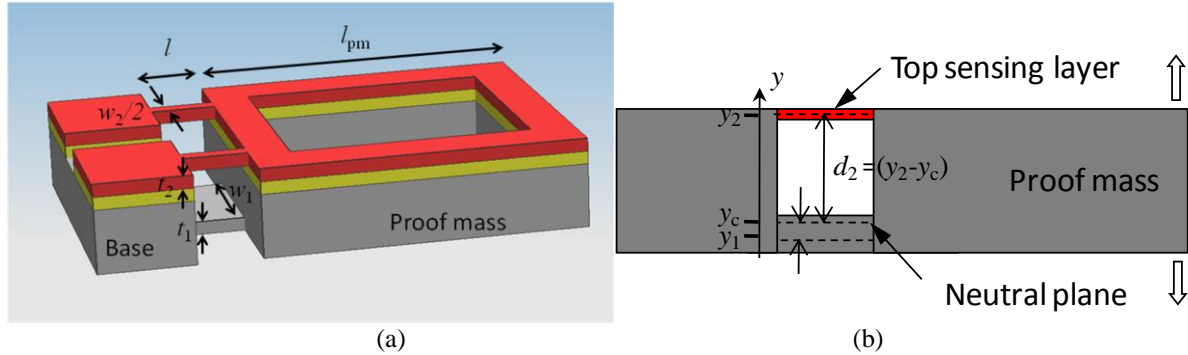
Figure. 6.1. (a) Schematic of the resonant mass sensor based on asymmetrically-gapped cantilever (the proof mass is hollow to reduce the effective mass); (b) cross sectional view of the asymmetrically-gapped cantilever.

As mentioned in chapter 2, the mechanical strain experienced by the top sensing beam is significantly increased in gapped cantilever structure, and this in turn leads to larger $v_{carrier}$. Consequently, a better mass resolution can be achieved as illustrated in Eq. (6.3) if v_{noise} is a constant (e.g., the noise of readout circuit).

6.3 Meso-scale prototype

6.3.1 Structure

To prove the concept of resonant mass sensor based on gapped cantilever structure, a meso-scale prototype is designed and developed. Note that the top beam is piezoelectric in this meso-scale design. The schematic structure of designed meso-scale resonant mass sensor is shown in Fig. 6.2. As we can see from the top and side views, the shape of proof mass in this design is hollow and tapered. This is because we prefer the proof mass as light as possible to increase the resolution of mass sensing.

(a) top view (b) side view
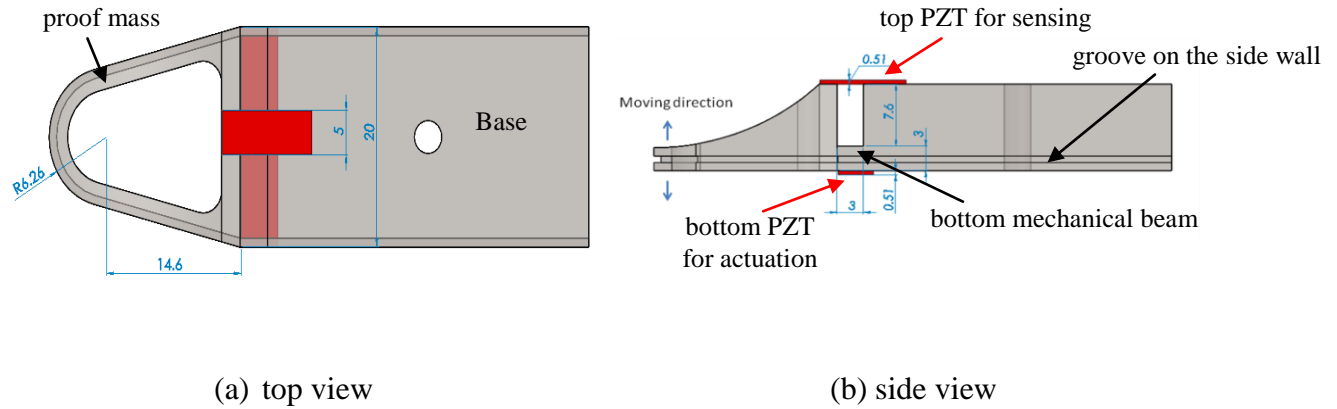
Figure. 6.2. Schematic (a) top view and (b) side view of the meso-scale resonant mass sensor based on gapped cantilever structure.

6.3.2 Development

The developed meso-scale resonant mass sensor is shown in Fig. 6.3. The sensor body contacting base, bottom mechanical beam and proof mass is made by one piece of aluminum block. Top PZT sheet (T105-A4E-602, Piezo System, Inc., Cambridge, MA, USA) is then glued across a narrow trench machined on the aluminum substrate using conductive epoxy to form the gapped cantilever structure. A grove is carved on the sidewall of the resonator to fit the PEEK tubing which allows the flow-through of liquid sample. Another PZT sheet is bonded to the bottom surface of the aluminum mechanical beam for the purpose of driving the resonator for vibration. Lead wires are glued to both PZT sheets using conductive epoxy. The aluminum substrate serves as the ground. A PEEK tubing (0.5 mm i.d.) is glued to the groove on the sidewall of the resonator. The total length of the tubing wrapped around the resonator lever is about 47 mm which results in a sample volume of 38 μL.
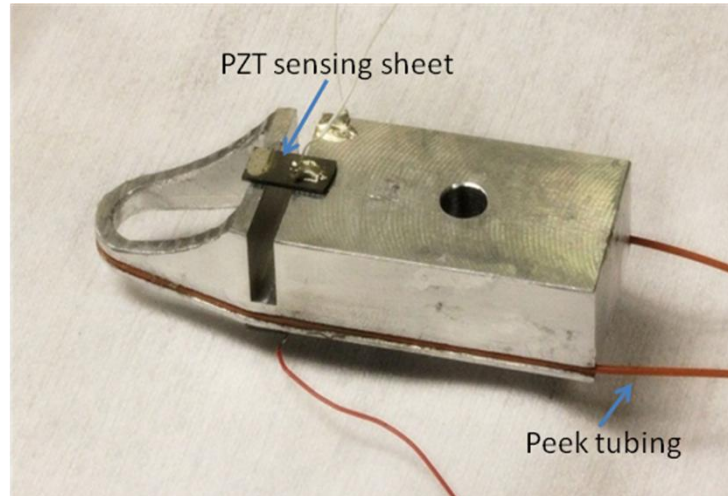
Figure. 6.3. Picture of a meso-scale prototype device made by an aluminum block, PZT sheets, PEEK tubing and lead wires.

6.3.3 Characterization

The resonator is tested in a vacuum chamber to reduce the air damping. The electrical connections are made using an electrical feed-through. The PEEK tubing glued on the resonator can be accessed externally via two small holes drilled on the vacuum chamber. The measurement setup is schematically illustrated in Fig. 6.4. In our preliminary test, the resonator is driven at a fixed frequency. The shift of resonant frequency is then measured indirectly through the amplitude change of the vibration (slope detection) [97]. Specifically, a sinusoidal voltage provided by a function generator (Agilent 33120A) is applied to the bottom PZT sheet to actuate the resonator at a frequency f_d slightly higher than its resonant frequency. At this frequency, the amplitude has the maximum slope with respect to the frequency. The vibration signal from the top PZT beam is first high-pass filtered and then amplified using a pre-amplifier (Stanford Research SR560). The RMS amplitude of the sinusoidal voltage is measured by a multi-meter (Agilent 34401A) and recorded into a computer via a GPIB port of the multi-meter

with 5 Hz sampling rate. Note that the measured signal is RMS amplitude of the voltage from

the top sensing PZT beam which indicates the RMS amplitude of the resonant level.
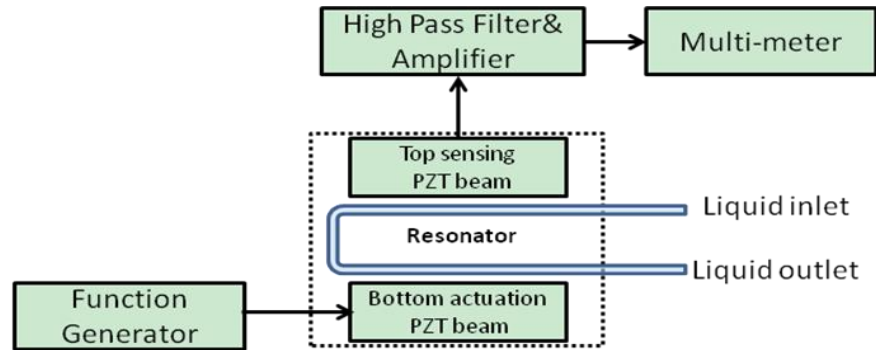
Figure. 6.4. Schematic diagram of the measurement setup for the resonant mass sensor.
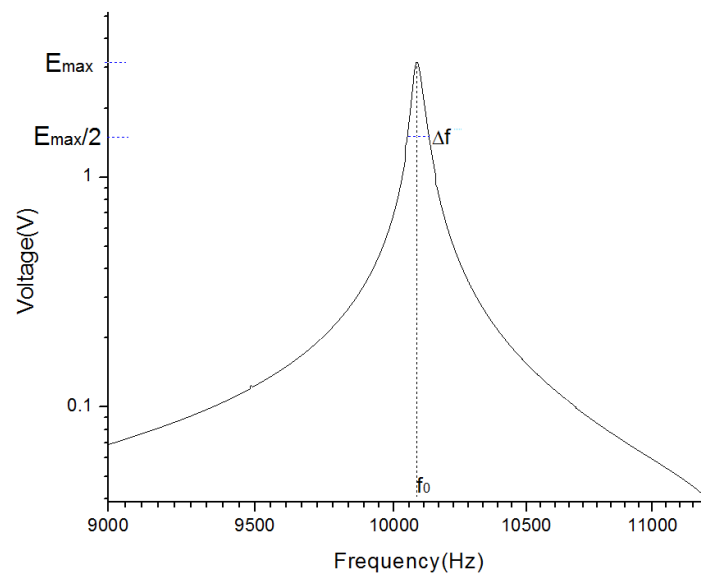
Figure. 6.5. Frequency response of the resonant mass sensor. Vertical axis is the steady-state RMS amplitude.

The frequency response of the resonant mass sensor when the channel is empty is

measured and the result is shown in Fig. 6.5. Based on the frequency response curve, the quality

factor can be calculated, which is

$$Q = f_0 / \Delta f \approx 240 \tag{6.4}$$

To maximize the sensitivity of slope detection, the driving frequency is selected as [97]

$$f_d \approx f_0(1+\frac{1}{\sqrt{8Q}}) \tag{6.5}$$
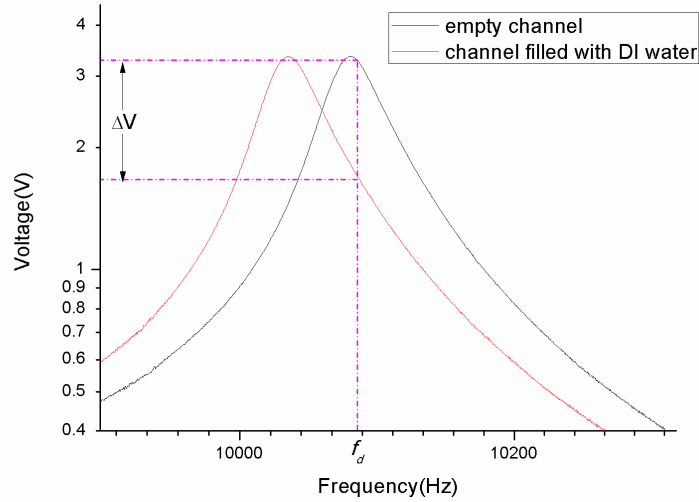
Figure. 6.6. Frequency responses of RMS amplitude before and after the channel is filled with DI water.

Figure 6.6 plots the frequency responses of the sensor before and after the PEEK tubing is filled with DI (de-ionized) water. The shift of resonant frequency can be clearly observed. Figure 6.6 also illustrates the basic principle of slope detection. When the resonator is driven at a fixed frequency, the resonant frequency shift can be measured indirectly by monitoring the vibrating amplitude change. It can also be observed that the quality factor almost remained unchanged after the channel is filled by water. A well-known challenge of resonant mass sensor is the viscous damping in liquid. It has been demonstrated previously that integration of fluidic channels with the resonator is a promising approach to address the liquid damping issue [89-91, 98]. The experimental results shown above confirmed this conclusion.

In another set of experiment, the prototype is tested by sequentially injecting alcohol and DI water in the PEEK tubing. Fig. 6.7 shows the real-time amplitude of the resonator when alcohol and DI water are sequentially injected. The signal change caused by different densities of solutions can be clearly observed. The transient response due to the sample injection can also be observed. Similar experiment is also performed using 1X, 5X, and 10X phosphate buffered saline (PBS) solutions. The output voltage change, together with the alcohol and DI water data, are plotted in Fig. 6.8. Note that the drifting of the ambient temperature has considerable impact on the resonant frequency. In order to acquire more consistent data, vibration amplitude of the empty tubing is always measured as a reference for every solution measurement.

Based on the date shown in Fig 6.8, the sensitivity is calculated to be 1.1 $V/(g\ cm^{-3})$ for the prototype device. The standard deviation of the signal is 6.6×10^{-5} V as shown in the inset of Fig. 6.7. Therefore, the minimum detectable density change is calculated to be 6.0×10^{-5} $g\ cm^{-3}$ and the corresponding mass change is 2.3 µg.
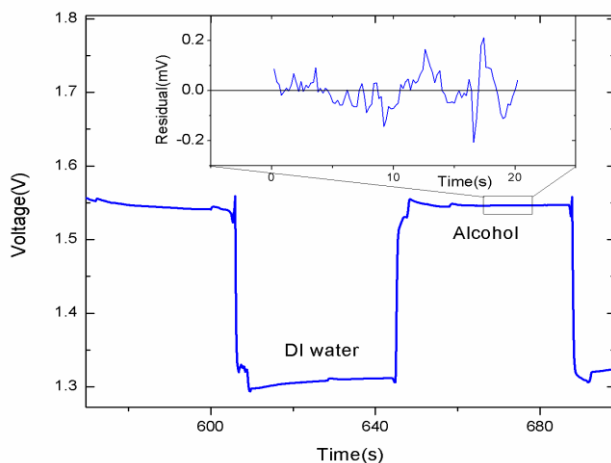
Figure 6.7. RMS Vibration amplitude (voltage) of the resonator when alcohol and DI water are sequentially injected. Inset shows the noise information with low frequency drift removed.
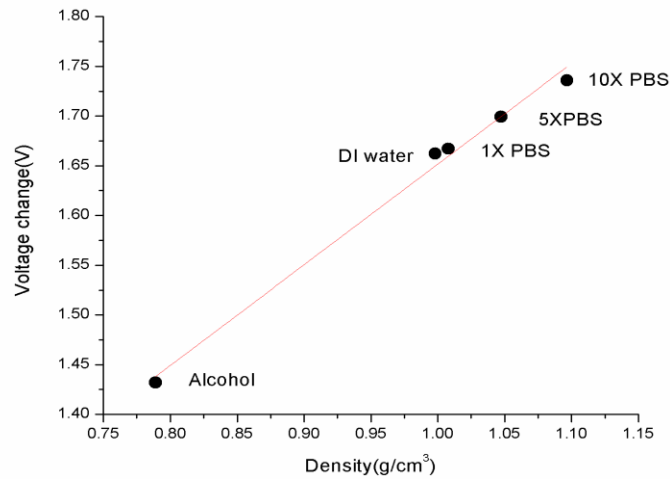
Figure. 6.8. Vibration amplitude change (referenced to the case when the channel is empty) as a function of liquid density

Note that these results are achieved using a meso-scale prototype and the experimental conditions are not ideal. Even based on these non-optimal results, a simple scaling analysis based on Eq. (6.3) indicates that atto-gram (10^{-18} gram) mass resolution in liquid can be achieved if the dimension of the resonator is scaled down by a factor of 1000 (to ~20 μm), and the quality factor and signal to noise ratio combined can be improved by 500.

It is worth noting that the meso-scale prototype based on PZT sheets can potentially function as a densitometer. Commercial densitometers have been developed based on vibrating U-tubes. The vibration of U-tubes is typically detected using coils [99]. Research prototypes of vibrating U-tube densitometers based on optical detection methods have also been developed [100]. Compared with existing products on the market, the advantages of this new design include low cost and portability. The stability and repeatability need to be further investigated.

6.4 Micro-scale prototype

6.4.1 structure

The schematic structure of the proposed micro-scale resonant mass sensor is shown in Fig. 6.9. Note that the top beams are piezoresistive in this micro-scale design. This sensor includes three main parts: 1) a gapped cantilever piezoresistive resonator; 2) a base with gold contact pads; and 3) and two solid legs for tube coupling. Note that there is a micro channel going through the whole structure routing one leg, base, cantilever resonator, base and the other leg. This channel serves as a tube from which the liquid is injected for mass sensing. In this design, the gapped cantilever resonator has four top silicon beams, two bottom mechanical beams with micro channel and a hollow proof mass with micro channel. It's worth noting that one pair of the top silicon beams are used as a thermo-elastic actuators to drive the cantilever to vibrate, and the other pair are used as piezoresistors for strain sensing as shown in Fig. 6.9(inset).
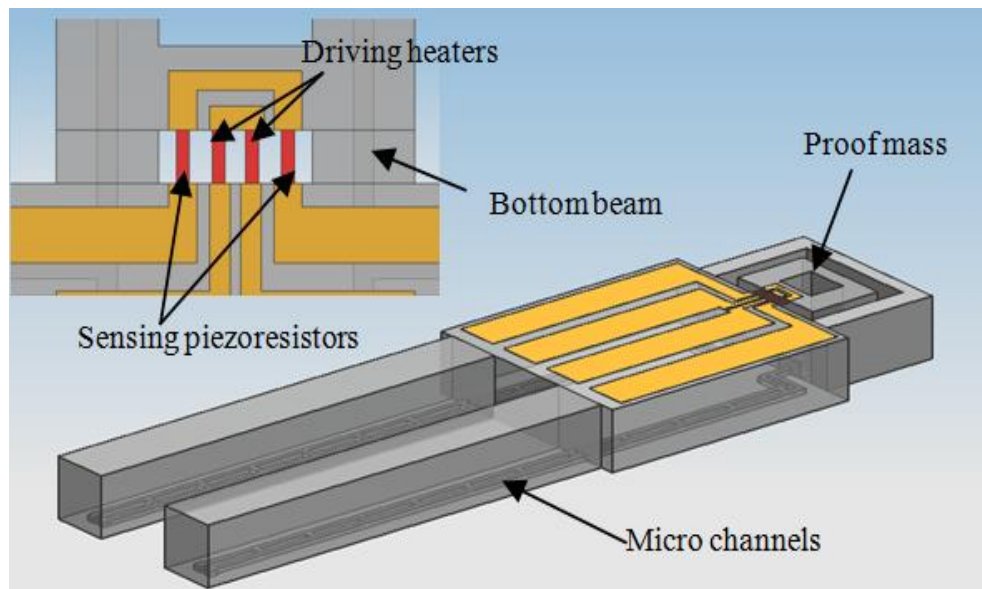
Figure 6.9. schematic top view (inset) and 3D view of the proposed micro-scale resonant mass sensor based on gapped cantilever structure.

6.4.2 Simulation

Finite element simulations are carried out to verify the parameters that derived from our analytical model. The geometric and material properties are selected as: w_1=400 μm, t_1=100 μm, l_1=95 μm, w_2=100 μm, t_2=20 μm, l_2=95 μm, w_m=700 μm, t_m=400 μm, l_m=495 μm, E_1= E_2=E_m=168 Gpa, ρ_1= ρ_2 =ρ_m= 2330 kg/m^3. The hollow cavity inside the proof mass is 245 μm wide and 350 μm long. Based on the theoretical model derived in chapter 2, a resonant frequency of 6.46×10^5 Hz and normal strain of 5.34×10^{-9} on top piezoresistive beams are derived. Finite element simulation is again performed using commercial software Comsol 4.3. The simulation results show an average normal strain of 5.45×10^{-9} on the top piezoresistive beams, which is very close to the analytical result. The simulated resonant frequency is 5.45×10^5 Hz which is about 15 % less than analytical result. The resonant frequency discrepancy is mainly caused by the error induced from the hollow proof mass. Finite element simulation result of the deformed resonant mass sensor is schematically shown in Fig. 6.10.
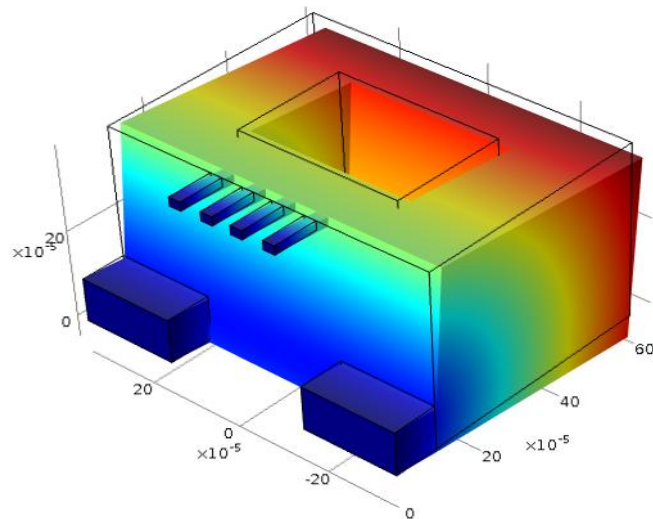
Figure 6.10. Schematic result of the finite element simulation for the piezoresistive resonant mass sensor. The micro channels in the bottom beams and proof mass are neglected in the simulation.

6.4.3 Fabrication

The proposed micro-scale piezoresistive resonant mass sensor is fabricated in this work. The fabrication process is similar to the process for piezoresistive accelerometer described in section 4.4, except for the fabrication of the micro channels. A 4" (100) SOI wafers purchased from MEMS Engineering & Material, Inc (Fremont, California) is also used for resonant mass sensor. The handle/oxide/device layers have thicknesses of 380 μm/0.5 μm/20 μm respectively. The resistivity of the device layer is 0.01~0.02 Ω·cm. First, a 20 nm/200 nm thick Cr/Au film is deposited and patterned to form the metal traces and contact pads. Next, DRIE is used to etch the device layer to form the top piezoresistive beams. Then, a 5-6 μm thick parylene C layer is deposited on both sides of the wafer. Note that back parylene C layer is used to form micro channel, but front parylene C layer serves as a protection layer while performing backside processes, Next, a 200 nm thick aluminum layer is deposited and patterned on backside. Oxygen plasma process is then performed to etch parylene C underneath using the aluminum layer patterned previously as the mask. The next step on backside is XeF_2 isotropic etching of silicon using parylene C layer as the mask to form the micro channels, followed by another parylene C deposition of about 7 μm thick to seal the channel openings. A photograph of the fabricated micro channel is shown in Fig. 6.11. Coming back to the front side process, aluminum deposition/patterning, parylene C patterning, and silicon etching are processed in sequence to form the cavity which defines the top edges for bottom mechanical beams. Another back DRIE is then performed using the same process as front DRIE to complete the side edges of bottom mechanical beam and release the devices. In the last, the buried oxide layer is removed using BHF solution. Next, the micro fabricated devices are seperated from the wafer, glued on printed circuit boards (PCB) and wire-bonded. Finally, the protective front parylene C layer is removed

by oxygen plasma after the packaging process is finished. A photograph of the fabricated resonant mass sensor is shown in Fig. 6.12.
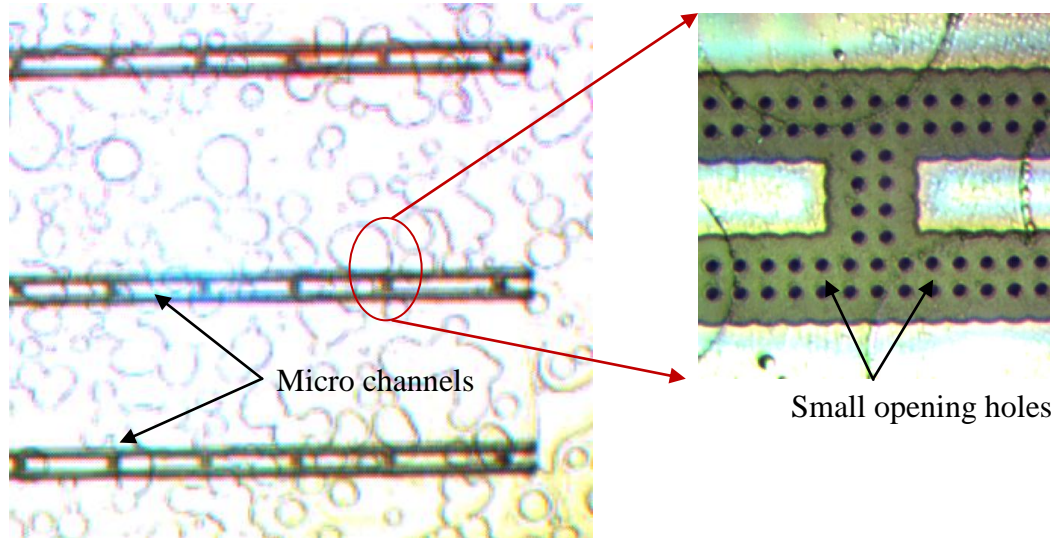
Figure 6.11. Photograph of the micro channel fabricated on back side of the wafer. Simplified fabrication process: 1) first layer of parylene C is deposited and patterned to form the opening holes. 2) XeF_2 isotropic etching is performed to etch silicon underneath to form the channel cavity. 3) another parylene C is deposited to seal the channel openings.
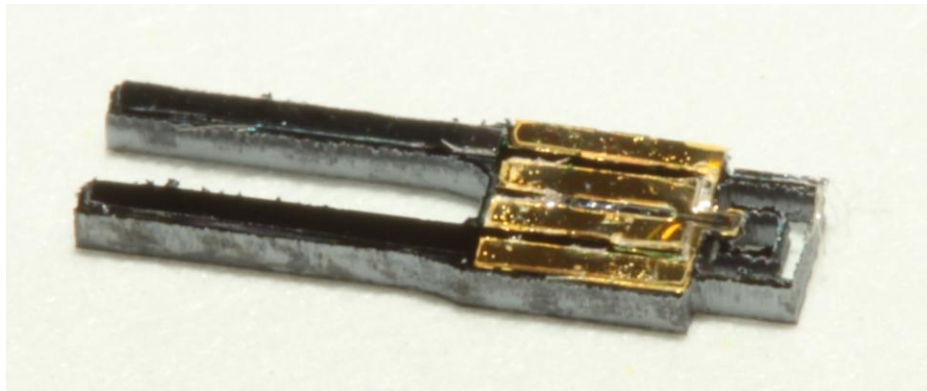
Figure 6.12. Photograph of the fabricated prototype resonant mass sensor.

6.4.4 Preliminary characterization

Preliminary test has been carried out. A sinusoidal voltage is applied to the thermo-elastic

actuation beams, and signals from the sensing piezoresistors are measured through a wheatstone

bridge. The result is shown in Fig. 6.13. As expected, the output signal is sinusoidal as well.

However, it's interesting to note that the frequency of output signal is doubled from input signal

since the thermo-elastic actuators experience expansion twice in one cycle of the input signal at

both positive and negative voltage phases. This results show the feasibility of driving the sensor

using thermo-elastic actuation, and sensing using piezoresistive method.
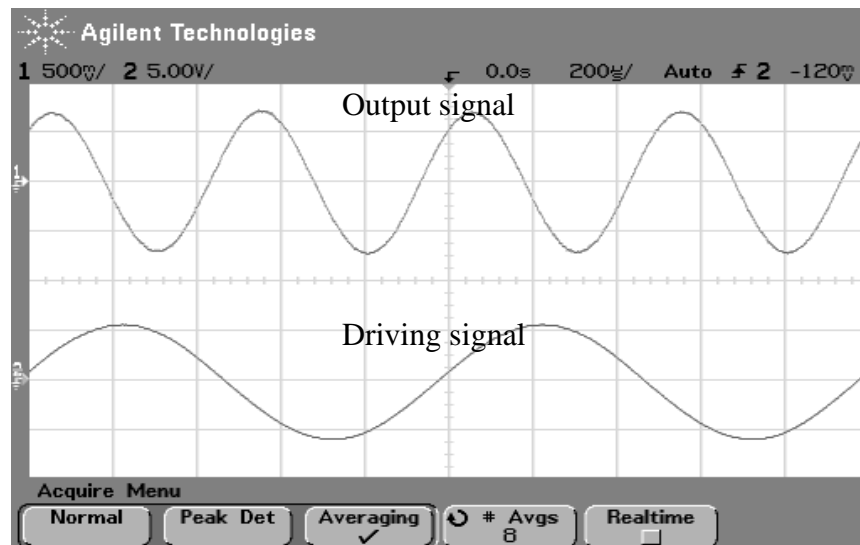
Figure 6.13. The output voltage from wheatstone bridge with sensing piezoresistors connected
and the input voltage to the driving piezoresistors. Note that frequency of output signal is
doubled from input voltage.

However, the output voltage amplitude shows a rapid decay after about 10 kHz and the

frequency turns to be the same as the input signal as well. This phenomenon makes it impossible

to measure the vibration of the micro-scale resonant mass sensor close to its resonant frequency

at ~500 kHz. Consequently, the mass sensing could not be carried out. There are several possible

reasons for the suppression of output voltage at high frequency. First, the power of thermoelastic

actuation using one pair of top silicon beams may not be large enough to drive the sensor to

vibrate at high frequencies. Second, the electro-magnetic coupling may be enhanced as

frequency increases, and thus severely interfere the signal from sensing piezoresistors. The third possible reason is that the thermal actuation may be suppressed by thermoelastic damping at high frequencies. In order to be able successfully characterize the micro-scale resonant mass sensor, these issues have to be solved by implementing new design, new fabrication process or just simply a better signal processing unit in the future.

6.5 Summary

Resonant mass sensor based on gapped cantilever structure is studied in this chapter. First, the sensing mechanism and the advantage of gapped cantilever for resonant mass sensor are theoretically interpreted by analyzing minimum detectable mass. Following the analysis carried out previously, a design of resonant mass sensor based on gapped cantilever structure is proposed, in which the proof mass is made hollow in order to reduce the mass for higher mass sensitivity. A meso-scale piezoelectric prototype is first designed and developed using aluminum block and PZT sheets. A series of tests have been done with this device for liquid mass sensing, and a sensitivity of 1.1 V/(g cm^{-3}) and a minimum detectable mass of 2.3 μg are obtained. These results prove the concept of mass sensing using resonant mass sensor based on gapped cantilever structure. In the next step, a micro-scale piezoresistive prototype is designed and successfully microfabricated. Preliminary test demonstrates the feasibility of thermoelastic actuation and piezoresistive sensing mechanism at low frequencies (below ~10 kHz). However, the functionality of the prototype is not proved at high frequencies, especially around the resonant frequencies at which the resonator should be operated. Possible reasons include low power, electro-magnetic coupling and thermo-elastic damping.

CHAPTER 7. CONCLUSION & FUTURE WORK

7.1 Conclusion

In this Ph.D. thesis work, gapped cantilever structure is proposed to significantly improve the performances of cantilever based piezoresistive/piezoelectric transducers. This novel structure is implemented to several applications in this work with the assistance by analytical model and finite element simulations. Numerous meso-scale or micro-scale prototypes are developed and tested. The experimental results demonstrate the advantage and feasibility of gapped cantilever structure for the enhancement of strain sensitivity and energy efficiency. Major results and accomplishments in this work can be summarized as follow:

- Analytical model for gapped cantilever structure is established by decomposing the deformation into rotational and translational bending.

- Optimization process is discussed to maximize the energy conversion efficiency.

- Finite element simulation is performed to verify the analytical model and to guide the design.

- Piezoresistive accelerometer based on gapped cantilever structure is designed and successfully micro-fabricated.

- Characterization results of the piezoresistive accelerometer show a good agreement with analytical model and finite element simulation.

- Vibration energy harvester based on gapped cantilever structure is designed and a meso-scale prototype is developed.

- Bench-top characterization results of vibration energy harvester show good agreement with analytical model and finite element simulation.

- Road test of the vibration energy harvester proves the feasibility of scavenging enough energy for tire pressure monitoring.

- Road test also indicates that it is more efficient to harvest energy from the vibration of the tire in tangential direction rather than in centrifugal direction.

- Resonant mass sensor based on gapped cantilever structure is designed and prototypes are developed both in meso-scale and micro-scale.

- Meso-scale prototype experiments successfully prove the concept of mass sensing using resonant mass sensor based on gapped cantilever structure.

In summary, this Ph.D. work has resulted in a number of important contributions to the field of cantilever based piezoresistive/piezoelectric transducers.

7.2 Future work

An enormous amount of research on the applications of gapped cantilever structure for piezoresistive accelerometer, vibration energy harvester and resonant mass sensor is still underway. Even though a great effort has been made on these subjects in this work and as a result plenty of important accomplishments have been achieved, there are still a lot more improvements could be made in the future.

7.2.1 Piezoresistive accelerometer

In the future, the performance of the piezoresistive accelerometer could be further improved by optimizing the structure parameters, material properties and fabrication process. For example, the mechanical beam can be split into two beams and moved to the two edges of the proof mass to further reduce the torsional mode and in-plane deflection. Another improvement is to select optimal doping concentration of the piezoresistor. In the current work, the piezoresistor is heavily doped for the simplification of the fabrication process whereas not necessarily optimal for signal-to-noise ratio. The fabrication process can be improved by using SOI wafers with two device layers, i.e., device layers on both sides of the handle wafer, to precisely control the thickness of the mechanical beam. Methods such as high temperature annealing can be investigated to further reduce noise in the future. To reduce the temperature sensitivity, the method reported in [7] which utilizes the orientation dependence of the piezoresistive coefficient of single crystal silicon can be employed as well.
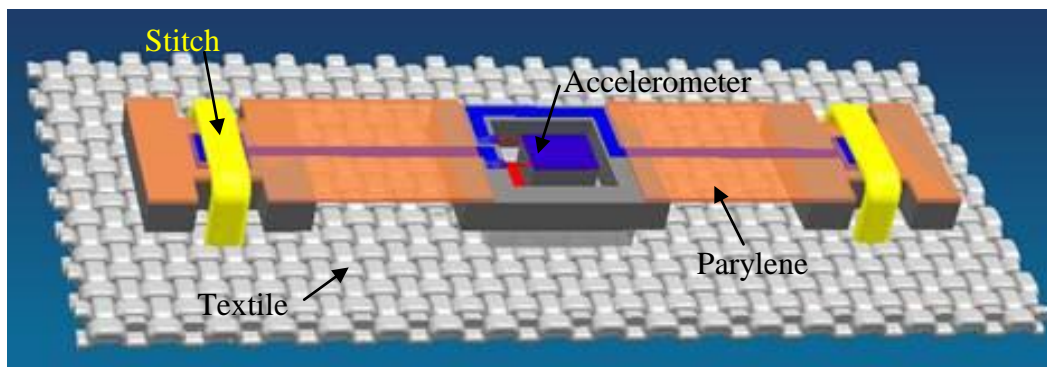
Figure 7.1. 3D illustration of a bandage-like wearable accelerometer for continuous respiratory sound monitoring.

In order for the accelerometer to eventually be able to continuously monitor human lung sound, it is necessary to make the accelerometer wearable as mentioned in section 4.1.2.

Currently, our group is investigating a technique called "intelligent textile" to make the piezoresistive accelerometer be able to attach on textile as shown in Fig. 7.1. In this case, vibrations from human chest can be easily measured by the sensor on textile which can be worn by human.

7.2.2 Vibration energy harvester

The fabricated vibration energy harvester has not fully optimized, and the performance can be further improved by selecting proper geometric and material properties. Based on theoretical analysis, the energy conversion efficiency can reach even up to 90%. Diodes with lower bias voltage or better circuit scheme can be used to increase the AC to DC conversion efficiency as well. The size of the device can also be further reduced even to micro-scale in order for more applications and to somehow match with industry requirement. Since the vibration energy harvesting in tangential direction on the tire is proved to be more efficient than in centrifugal direction, it is necessary to re-investigate the design accordingly in the future to meet the requirement for tangential direction. By taking the advantage of higher energy efficiency of the gapped cantilever structure, vibration energy harvesters can also be designed for many other applications.

It's also worth noting that the vibration energy harvester based PZT is not totally green because PZT contains lead. To make it completely green, other lead-free piezoelectric materials can be utilized. One candidate is reported by Saito *et al*. [101], whose performance is comparable to PZT.

7.3.3. Resonant mass sensor

The study for resonant mass sensor based on gapped cantilever is still at initial stage, and a lot more systematic study is underway. Even though meso-scale prototype shows a good

performance, the characterization of micro-scale resonant mass sensor encounters some difficulties. For example, the thermo-elastic actuation is only working at low frequency (less than 10 kHz) for current prototype in current measurement system, and the problems at high frequencies is still under investigation. The liquid injection testing of the micro-channels are also planned in the next step to verify the feasibility the micro-channel design and fabrication process. Once the functionality of the resonant mass sensor is demonstrated, different types of liquid will be injected into the channel while keeping the sensor vibrating at resonant frequency to characterize the sensitivity of the sensor. Noise issues are also critical and need to be studied a lot more in the future.

7.3.4 Other potential applications

As mentioned previously, there could be plenty of other applications of gapped cantilever structure by taking the advantage of high sensitivity and high energy conversion efficiency. For example, investigations of gapped cantilever for atomic force microscope, ultrasonic power transfer, force sensing and time reference, etc. can be conducted in the future.

REFERENCES

[1]   R. Amarasinghe, D. V. Dao, T. Toriyama, and S. Sugiyama, "Development of miniaturized 6-axis accelerometer utilizing piezoresistive sensing elements," *Sensors and Actuators a-Physical,* vol. 134, pp. 310-320, Mar 2007.

[2]   M. H. Bao, *Micro Mechanical Transducers: Pressure Sensors, Accelerometers and Gyroscopes*: Elsevier Science, 2000.

[3]   A. A. Barlian, S. J. Park, V. Mukundan, and B. L. Pruitt, "Design and characterization of microfabricated piezoresistive floating element-based shear stress sensors," *Sensors and Actuators a-Physical,* vol. 134, pp. 77-87, Feb 2007.

[4]   A. A. Barlian, W. T. Park, J. R. Mallon, A. J. Rastegar, and B. L. Pruitt, "Review: Semiconductor Piezoresistance for Microsystems," *Proceedings of the Ieee,* vol. 97, pp. 513-552, Mar 2009.

[5]   R. E. Beaty, R. C. Jaeger, J. C. Suhling, R. W. Johnson, and R. D. Butler, "Evaluation of piezoresistive coefficient variation in silicon stress sensors using a 4-point bending test fixture," *IEEE Transactions on Components Hybrids and Manufacturing Technology,* vol. 15, pp. 904-914, Oct 1992.

[6]   H. Chen, M. H. Bao, H. J. Zhu, and S. Q. Shen, "A piezoresistive accelerometer with a novel vertical beam structure," *Sensors and Actuators a-Physical,* vol. 63, pp. 19-25, Sep 1997.

[7]   B. W. Chui, L. Aeschimann, T. Akiyama, U. Staufer, N. F. de Rooij, J. Lee*, et al.*, "Advanced temperature compensation for piezoresistive sensors based on crystallographic orientation," *Review of Scientific Instruments,* vol. 78, Apr 2007.

[8] H. Crazzolara, G. Flach, and W. Vonmunch, "Piezoresistive accelerometer with overload protection and low cross-sensitivity," *Sensors and Actuators a-Physical,* vol. 39, pp. 201-207, Dec 1993.

[9] R. Dieme, G. Bosman, T. Nishida, and M. Sheplak, "Sources of excess noise in silicon piezoresistive microphones," *Journal of the Acoustical Society of America,* vol. 119, pp. 2710-2720, May 2006.

[10] J. C. Doll, S. J. Park, and B. L. Pruitt, "Design optimization of piezoresistive cantilevers for force sensing in air and water," *Journal of Applied Physics,* vol. 106, p. 12, Sep 2009.

[11] P. T. Dong, X. X. Li, H. Yang, H. F. Bao, W. Zhou, S. Y. Li, *et al.*, "High-performance monolithic triaxial piezoresistive shock accelerometers," *Sensors and Actuators a-Physical,* vol. 141, pp. 339-346, Feb 2008.

[12] E. J. Eklund and A. M. Shkel, "Single-mask fabrication of high-G piezoresistive accelerometers with extended temperature range," *Journal of Micromechanics and Microengineering,* vol. 17, pp. 730-736, Apr 2007.

[13] J. C. Greenwood, "Silicon in mechanical sensors," *Journal of Physics E-Scientific Instruments,* vol. 21, pp. 1114-1128, Dec 1988.

[14] J. A. Harley and T. W. Kenny, "1/F noise considerations for the design and process optimization of piezoresistive cantilevers," *Journal of Microelectromechanical Systems,* vol. 9, pp. 226-235, Jun 2000.

[15] F. N. Hooge, "1/f noise is no surface effect," *Physics letters A,* vol. 29, pp. 139-140, 1969.

[16] F. N. Hooge, "1/F Noise sources," *Ieee Transactions on Electron Devices,* vol. 41, pp. 1926-1935, Nov 1994.

[17]   S. S. Huang, X. X. Li, Z. H. Song, Y. L. Wang, H. Yang, L. F. Che*, et al.*, "A high-performance micromachined piezoresistive accelerometer with axially stressed tiny beams," *Journal of Micromechanics and Microengineering,* vol. 15, pp. 993-1000, May 2005.

[18]   Z. Wang and Y. Xu, "Design and optimization of an ultra-sensitive piezoresistive accelerometer for continuous respiratory sound monitoring," *Sensor Letters,* vol. 5, pp. 450-458, Jun 2007.

[19]   Z. Wang and Y. Xu, "Vibration energy harvesting device based on air-spaced piezoelectric cantilevers," *Applied Physics Letters,* vol. 90, p. 263512, Jun 25 2007.

[20]   Q. Zheng and Y. Xu, "Vibration energy harvesting device based on asymmetric air-spaced cantilevers for tire pressure monitoring system," presented at the The 9th International Workshop on Micro and Nanotechnology for Power Generation and Energy Conversion Applications, Washington DC, USA, 2009.

[21]   Q. L. Zheng, Z. Wang, and Y. Xu, "Symmetric air-spaced cantilevers for strain sensing," *Sensors and Actuators a-Physical,* vol. 147, pp. 142-149, Sep 15 2008.

[22]   Q. L. Zheng and Y. Xu, "Asymmetric air-spaced cantilevers for vibration energy harvesting," *Smart Materials & Structures,* vol. 17, Oct 2008.

[23]   R. Elfrink, T. M. Kamel, M. Goedbloed, S. Matova, D. Hohlfeld, Y. van Andel*, et al.*, "Vibration energy harvesting with aluminum nitride-based piezoelectric devices," *Journal of Micromechanics and Microengineering,* vol. 19, Sep 2009.

[24]   T. V. Roszhart, H. Jerman, J. Drake, and C. d. Cotiis, "An inertial-grade, micromachined vibrating beam accelerometer," in *Transducers*, Stockholm, Sweden, 1995.

[25]   K. Naeli and O. Brand, "Cantilever sensor with stress-concentrating piezoresistor design," in *the Fourth IEEE Conference on Sensors*, Irvine, CA, USA, 2005, pp. 592-595.

[26]   A. D. Kurtz, "Transducers employing gap-bridging shim members," USA Patent US Patent 3,995,247, Nov. 30,1976, 1976.

[27]   L. B. Wilner, "Piezoresistive transducer," US patent 4,498,229, Feb. 12, 1985, 1985.

[28]   L. B. Wilner, "Piezoresistive transducer," US patent 3,351,880, Nov. 7, 1967, 1967.

[29]   A. D. Kurtz and A. A. Ned, "Piezoresistive accelerometer with enhaced performance," US patent 5,539,236, Jul. 23, 1996, 1996.

[30]   E. J. Hearn, "Mechanics of Materials," 1997.

[31]   N. Yazdi, F. Ayazi, and K. Najafi, "Micromachined inertial sensors," *Proceedings of the Ieee,* vol. 86, pp. 1640-1659, Aug 1998.

[32]   L. M. Roylance and J. B. Angell, "Batch-fabricated silicon accelerometer," *Ieee Transactions on Electron Devices,* vol. 26, pp. 1911-1917, 1979.

[33]   K. H. Kim, J. S. Ko, Y. H. Cho, K. Lee, B. M. Kwak, and K. Park, "A skew-symmetric cantilever accelerometer for automotive airbag applications," *Sensors and Actuators a-Physical,* vol. 50, pp. 121-126, Aug 1995.

[34]   Y. B. Ning, Y. Loke, and G. McKinnon, "Fabrication and characterization of high g-force, silicon piezoresistive accelerometers," *Sensors and Actuators a-Physical,* vol. 48, pp. 55-61, May 1995.

[35]   J. J. Pak, A. E. Kabir, G. W. Neudeck, and J. H. Logsdon, "A bridge-type piezoresistive accelerometer using merged epitaxial lateral overgrowth for thin silicon beam formation," *Sensors and Actuators a-Physical,* vol. 56, pp. 267-271, Sep 1996.

[36] K. Kwon and S. Park, "A bulk-micromachined three-axis accelerometer using silicon direct bonding technology and polysilicon layer," *Sensors and Actuators a-Physical,* vol. 66, pp. 250-255, Apr 1998.

[37] J. H. Sim, C. S. Cho, J. S. Kim, and J. H. Lee, "Eight-beam piezoresistive accelerometer fabricated by using a selective porous-silicon etching method," *Sensors and Actuators a-Physical,* vol. 66, pp. 273-278, Apr 1998.

[38] A. Partridge, J. K. Reynolds, B. W. Chui, E. M. Chow, A. M. Fitzgerald, L. Zhang*, et al.*, "A high-performance planar piezoresistive accelerometer," *Journal of Microelectromechanical Systems,* vol. 9, pp. 58-66, Mar 2000.

[39] J. A. Plaza, A. Collado, E. Cabruja, and J. Esteve, "Piezoresistive accelerometers for MCM package," *Journal of Microelectromechanical Systems,* vol. 11, pp. 794-801, Dec 2002.

[40] X. M. Yu, J. Thaysen, O. Hansen, and A. Boisen, "Optimization of sensitivity and noise in piezoresistive cantilevers," *Journal of Applied Physics,* vol. 92, pp. 6296-6301, NOV 15 2002.

[41] J. T. Suminto, "A wide frequency range, rugged silicon micro accelerometer with overrange stops," in *the Ninth IEEE international Workshop on Micro Electro Mechanical Systems*, San Diego, California, USA, 1996, pp. 180-5.

[42] R. Loudon and R. L. Murphy, Jr., "Lung sounds," *The American review of respiratory disease,* vol. 130, pp. 663-73, Oct 1984.

[43] N. Gavriely and D. W. Cugell, "Breath sounds sensors," in *Breath sounds methodology*, ed Boca Raton, Florida: CRC Press, 1995, pp. 31-47.

[44] H. Pasterkamp, S. S. Kraman, and G. R. Wodicka, "Respiratory sounds - Advances beyond the stethoscope," *American Journal of Respiratory and Critical Care Medicine,* vol. 156, pp. 974-987, Sep 1997.

[45] H. Wang and L. Y. Wang, "Continuous Intro-Operative Respiratory Auscultation in Anesthesia," in *IEEE Sensors* Toronto, 2003.

[46] R. Haladjian, H. Wang, L. Y. Wang, and H. Zheng, "Computer-Aided Continuous Lung Sound Auscultation in Ventilated Patients," in *A.S.A. Annual Conference*, Las Vegas, 2004.

[47] H. Wang, H. Zheng, L. Y. Wang, H. J. Normile, and J. Nofs, "Separation of Lung and Heart Sound for Anesthesia Diagnosis," in *the 2006 WSEAS International Conference on Mathematical Biology and Ecology (MABE '06)*, Miami, Florida, USA, 2006, pp. 63-68.

[48] R. P. Baughman and R. G. Loudon, "Lung sound analysis for continuous evaluation of airflow obstruction in asthma," *Chest,* vol. 88, pp. 364-8, Sep 1985.

[49] N. Meslier, G. Charbonneau, and J. L. Racineux, "Wheezes," *The European respiratory journal,* vol. 8, pp. 1942-8, Nov 1995.

[50] S. Rietveld, M. Oud, L. H. Rijssenbeek-Nouwens, D. Vaghi, and E. H. Dooijes, "Characteristics and diagnostic significance of spontaneous wheezing in children with asthma: results of continuous in vivo sound recording," *Journal of Asthma,* vol. 36, pp. 351-8, Jun 1999.

[51] C. Lenclud, G. Cuttitta, D. Van Gansbeke, A. Visconti, A. Van Muylem, V. Bellia*, et al.*, "Evaluation of nocturnal bronchoconstriction by all night tracheal sound monitoring," *Thorax,* vol. 51, pp. 694-8, Jul 1996.

[52] L. Bentur, R. Beck, M. Shinawi, T. Naveh, and N. Gavriely, "Wheeze monitoring in children for assessment of nocturnal asthma and response to therapy," *The European respiratory journal,* vol. 21, pp. 621-6, Apr 2003.

[53] P. E. Krumpe and J. M. Cummiskey, "Use of laryngeal sound recordings to monitor apnea," *The American review of respiratory disease,* vol. 122, pp. 797-801, Nov 1980.

[54] J. Werthammer, J. Krasner, J. DiBenedetto, and A. R. Stark, "Apnea monitoring by acoustic detection of airflow," *Pediatrics,* vol. 71, pp. 53-5, Jan 1983.

[55] J. E. Earis and B. M. G. Cheetham, "Future perspectives. for respiratory sound research," *European. Respiratory Review,* vol. 10, pp. 641-646, 2000.

[56] H. Pasterkamp, S. S. Kraman, P. D. Defrain, and G. R. Wodicka, "Measurement of respiratory acoustical signals - comparison of sensors," *Chest,* vol. 104, pp. 1518-1525, Nov 1993.

[57] L. Vannuccini, J. E. Earis, P. H. B. M. G. Cheetham, M. Rossi, A. R. A. Sovij 鋌 vi, and J. Vanderschoot, "Capturing and preprocessing of respiratory sounds," *European Respiratory Review,* vol. 10, pp. 616-620, 2000.

[58] S. S. Kraman, G. R. Wodicka, G. A. Pressler, and H. Pasterkamp, "Comparison of lung sound transducers using a bioacoustic transducer testing system," *J Appl Physiol,* vol. 101, pp. 469-476, August 1, 2006 2006.

[59] J. C. Ziegert and J. L. Lewis, "EFFECT OF SOFT-TISSUE ON MEASUREMENTS OF VIBRATIONAL BONE MOTION BY SKIN-MOUNTED ACCELEROMETERS," *Journal of Biomechanical Engineering,* vol. 101, pp. 218-220, 1979.

[60] K. J. Cho and H. H. Asada, "Wireless, battery-less stethoscope for wearable health monitoring," Philadelphia, PA, 2002, pp. 187-188.

[61]   S. Henneberg, B. Ноκ, L. Wiklund, and G. Sjodin, "Remote auscultatory patient monitoring during magnetic resonance imaging," *Journal of clinical monitoring,* vol. 8, pp. 37-43, Jan 1992.

[62]   Y. Nishida, T. Hori, T. Suehiro, and S. Hirai, "Monitoring of breath sound under daily environment by ceiling dome microphone," in *the IEEE International Conference on Systems, Man and Cybernetics*, Nashville, TN, USA, 2000, pp. 1822-9.

[63]   J. R. Mallon, A. J. Rastegar, A. A. Barlian, M. T. Meyer, T. H. Fung, and B. L. Pruitt, "Low 1/f noise, full bridge, microcantilever with longitudinal and transverse piezoresistors," *APPLIED PHYSICS LETTERS,* vol. 92, Jan 2008.

[64]   E. P. Vandamme and L. K. J. Vandamme, "Current crowding and its effect on 1/f noise and third harmonic distortion - a case study for quality assessment of resistors," *Microelectronics Reliability,* vol. 40, pp. 1847-1853, Nov 2000.

[65]   M. Shaw, "Battery-Less TPMS Technologies," in *Intelligent Tire Technology Conference*, 2007.

[66]   H. B. Fang, J. Q. Liu, Z. Y. Xu, L. Dong, L. Wang, D. Chen*, et al.*, "Fabrication and performance of MEMS-based piezoelectric power generator for vibration energy harvesting," *Microelectronics Journal,* vol. 37, pp. 1280-4, Nov 2006.

[67]   M. Ferrari, V. Ferrari, D. Marioli, and A. Taroni, "Modeling, fabrication and performance measurements of a piezoelectric energy converter for power harvesting in autonomous microsystems," *IEEE Transactions on Instrumentation and Measurement,* vol. 55, pp. 2096-101, Dec 2006.

[68]   S. P. Beeby, M. J. Tudor, and N. M. White, "Energy harvesting vibration sources for microsystems applications," *Measurement Science & Technology,* vol. 17, pp. R175-95, Dec 2006.

[69]   J. Ajitsaria, S. Y. Choe, D. Shen, and D. J. Kim, "Modeling and analysis of a bimorph piezoelectric cantilever beam for voltage generation," *Smart Materials & Structures,* vol. 16, pp. 447-54, Apr 2007.

[70]   S. Jiang, X. Li, S. Guo, Y. Hu, J. Yang, and Q. Jiang, "Performance for a piezoelectric bimorph for scavenging vibration energy," *Smart Materials & Structures,* vol. 14, pp. 769-74, 2005.

[71]   S. Roundy and P. K. Wright, "A piezoelectric vibration based generator for wireless electronics," *Smart Materials & Structures,* vol. 13, pp. 1131-42, 2004.

[72]   Y. C. Shu and I. C. Lien, "Analysis of power output for piezoelectric energy harvesting systems," *Smart Materials & Structures,* vol. 15, pp. 1499-1512, Dec 2006.

[73]   Y. C. Shu and I. C. Lien, "Efficiency of energy conversion for a piezoelectric power harvesting system," *Journal of Micromechanics and Microengineering,* vol. 16, pp. 2429-2438, Nov 2006.

[74]   H. A. Sodano, G. Park, and D. J. Inman, "Estimation of electric charge output for piezoelectric energy harvesting," *Strain,* vol. 40, pp. 49-58, May 2004.

[75]   T. H. Ng and W. H. Liao, "Sensitivity analysis and energy harvesting for a self-powered piezoelectric sensor," *Journal of Intelligent Material Systems and Structures,* vol. 16, pp. 785-797, Oct 2005.

[76]   H. A. Sodano, D. J. Inman, and G. Park, "Comparison of piezoelectric energy harvesting devices for recharging batteries," *Journal of Intelligent Material Systems and Structures,* vol. 16, pp. 799-807, Oct 2005.

[77]   H. A. Sodano, D. J. Inman, and G. Park, "Generation and storage of electricity from power harvesting devices," *Journal of Intelligent Material Systems and Structures,* vol. 16, pp. 67-75, Jan 2005.

[78]   H. A. Sodano, J. Lloyd, and D. J. Inman, "An experimental comparison between several active composite actuators for power generation," *Smart Materials & Structures,* vol. 15, pp. 1211-1216, Oct 2006.

[79]   S. R. Anton and H. A. Sodano, "A review of power harvesting using piezoelectric materials (2003-2006)," *Smart Materials & Structures,* vol. 16, pp. R1-R21, Jun 2007.

[80]   N. G. Elvin, N. Lajnef, and A. A. Elvin, "Feasibility of structural monitoring with vibration powered sensors," *Smart Materials & Structures,* vol. 15, pp. 977-986, Aug 2006.

[81]   H. Raisigel, J.-C. Crebier, Y. Lembeye, J. Delamare, and O. Cugat, "Autonomous, Low Voltage, High Efficiency, CMOS Rectifier for Three-Phase Micro Generators," presented at the Solid-State Sensors, Actuators and Microsystems Conference,TRANSDUCERS 2007. International 2007.

[82]   C. M. Lai and K. K. Shyu, "A single-stage AC/DC converter based on zero voltage switching LLC resonant topology," *Iet Electric Power Applications,* vol. 1, pp. 743-752, Sep 2007.

[83]   T. Thundat, E. A. Wachter, S. L. Sharp, and R. J. Warmack, "Detection of mercury-vapor using resonating microcantilevers," *Applied Physics Letters,* vol. 66, pp. 1695-1697, MAR 27 1995.

[84]   B. Ilic, D. Czaplewski, M. Zalalutdinov, H. G. Craighead, P. Neuzil, C. Campagnolo*, et al.*, "Single cell detection with micromechanical oscillators," *Journal of Vacuum Science & Technology B,* vol. 19, pp. 2825-2828, Nov-Dec 2001.

[85]   T. Ono, X. X. Li, H. Miyashita, and M. Esashi, "Mass sensing of adsorbed molecules in sub-picogram sample with ultrathin silicon resonator," *REVIEW OF SCIENTIFIC INSTRUMENTS,* vol. 74, pp. 1240-1243, Mar 2003.

[86]   A. Gupta, D. Akin, and R. Bashir, "Single virus particle mass detection using microresonators with nanoscale thickness," *Applied Physics Letters,* vol. 84, pp. 1976-1978, Mar 15 2004.

[87]   B. Ilic, H. G. Craighead, S. Krylov, W. Senaratne, C. Ober, and P. Neuzil, "Attogram detection using nanoelectromechanical oscillators," *Journal of Applied Physics,* vol. 95, pp. 3694-3703, Apr 1 2004.

[88]   M. Li, H. X. Tang, and M. L. Roukes, "Ultra-sensitive NEMS-based cantilevers for sensing, scanned probe and very high-frequency applications," *Nature Nanotechnology,* vol. 2, pp. 114-120, Feb 2007.

[89]   T. P. Burg, M. Godin, S. M. Knudsen, W. Shen, G. Carlson, J. S. Foster*, et al.*, "Weighing of biomolecules, single cells and single nanoparticles in fluid," *Nature,* vol. 446, pp. 1066-1069, Apr 26 2007.

[90]   S. Son, W. H. Grover, T. P. Burg, and S. R. Manalis, "Suspended microchannel resonators for ultralow volume universal detection," *Analytical Chemistry,* vol. 80, pp. 4757-4760, Jun 2008.

[91]   D. Sparks, R. Smith, M. Straayer, J. Cripe, R. Schneider, A. Chimbayo*, et al.*, "Measurement of density and chemical concentration using a microfluidic chip," *Lab on a Chip,* vol. 3, pp. 19-21, 2003.

[92]   B. Rogers, L. Manning, M. Jones, T. Sulchek, K. Murray, B. Beneschott*, et al.*, "Mercury vapor detection with a self-sensing, resonating piezoelectric cantilever," *REVIEW OF SCIENTIFIC INSTRUMENTS,* vol. 74, pp. 4899-4901, Nov 2003.

[93]   J. D. Adams, G. Parrott, C. Bauer, T. Sant, L. Manning, M. Jones*, et al.*, "Nanowatt chemical vapor detection with a self-sensing, piezoelectric microcantilever array," *Applied Physics Letters,* vol. 83, pp. 3428-3430, Oct 2003.

[94]   D. Z. Jin, X. X. Li, J. Liu, G. M. Zuo, Y. L. Wang, M. Liu*, et al.*, "High-mode resonant piezoresistive cantilever sensors for tens-femtogram resoluble mass sensing in air," *Journal of Micromechanics and Microengineering,* vol. 16, pp. 1017-1023, May 2006.

[95]   G. Yoshikawa, H. P. Lang, T. Akiyama, L. Aeschimann, U. Staufer, P. Vettiger*, et al.*, "Sub-ppm detection of vapors using piezoresistive microcantilever array sensors," *Nanotechnology,* vol. 20, p. 5, Jan 2009.

[96]   K. L. Ekinci, Y. T. Yang, and M. L. Roukes, "Ultimate limits to inertial mass sensing based upon nanoelectromechanical systems," *Journal of Applied Physics,* vol. 95, pp. 2682-2689, Mar 2004.

[97] Y. Martin, C. C. Williams, and H. K. Wickramasinghe, "Atomic force microscope force mapping and profiling on a sub 100-A scale," *Journal of Applied Physics,* vol. 61, pp. 4723-4729, May 1987.

[98] D. Westberg, O. Paul, G. Andersson, and H. Baltes, "A CMOS-compatible fluid density sensor," *Journal of Micromechanics and Microengineering,* vol. 7, pp. 253-255, Sep 1997.

[99] B. G. Liptak, C. H. Hoeppner, and G. H. Murer, "Liquid/Slurry/Gas Density—Vibrating Densitometers," in *Instrument Engineers' Handbook: Process control and optimization* B. G. Liptak, Ed., ed: CRC Press, 2006, pp. 844-851.

[100] T. Aida, A. Yamazaki, M. Akutsu, T. Ono, A. Kanno, T. A. Hoshina*, et al.*, "Laser-Doppler vibrating tube densimeter for measurements at high temperatures and pressures," *REVIEW OF SCIENTIFIC INSTRUMENTS,* vol. 78, Nov 2007.

[101] Y. Saito, H. Takao, T. Tani, T. Nonoyama, K. Takatori, T. Homma*, et al.*, "Lead-free piezoceramics," *Nature,* vol. 432, pp. 84-87, Nov 2004.

ABSTRACT

GAPPED CANTILEVER FOR THE ENHANCEMENT OF STRAIN SENSITIVITY AND ENERGY EFFICIENCY

by

QINGLONG ZHENG

December 2012

Advisor: Dr. Yong Xu

Major: Electrical Engineering

Degree: Doctor of Philosophy

Cantilever structures have been widely used in a large variety of transducer applications. For cantilever based transducers, piezoresistive/piezoelectric mechanisms has always been a popular choice due to the advantages of being low cost, simple structure and portability. However, low sensitivity is recognized as a major disadvantage of these transducers compared with optical based measurement. In this research, a gapped cantilever structure is proposed to potentially increase the sensitivity by orders of magnitude. In order to guide the design, an advanced analytical model is developed, and the increased strain sensitivity is theoretically demonstrated. In addition, optimizations with this model interestingly reveal that the gapped cantilever is much more efficient than conventional cantilever from energy perspective as well. Applications of gapped cantilever structure including piezoresistive accelerometer, vibration energy harvester and resonant mass sensor are carefully investigated in this work. Multiple prototypes of these applications both in meso-scale and micro-scale are designed, manufactured and characterized. The testing results show good agreement with theoretical expectation, and demonstrate a good potential of gapped cantilever structure for the enhancement of strain sensitivity and energy efficiency.

AUTOBIOGRAPHICAL STATEMENT

QINGLONG ZHENG

Education

- Sep. 2006 ~ Dec. 2012, **Ph.D.**, Department of Electrical and Computer Engineering, Wayne State University, Detroit, MI, USA

- Sep. 2001 ~ Jul. 2005, **B.S.**, Department of Precision Instruments and Mechanology, Tsinghua University, Beijing, P.R. China

Research and Working Experience

- Sep. 2006 ~ Apr. 2011, **Research assistant**, Department of Electrical and Computer Engineering, Wayne State University, Detroit, MI, USA

- Sep. 2008 ~ Apr. 2011, **Teaching assistant**, Department of Electrical and Computer Engineering, Wayne State University, Detroit, MI, USA

- Sep. 20011 ~ Feb. 2012, **Post-Doctoral Fellow**, The Institute for Complex Engineered Systems, Carnegie Mellon University, Pittsburgh, PA, USA

Selected Publications & Presentations

- Y. F. Li, **Q. Zheng**, Y. Hu and Y. Xu, "*Micromachined Piezoresistive Accelerometers Based on an Asymmetrically-Gapped Cantilever*", IEEE/ASME Journal of Microelectromechanical Systems, in press.

- **Q. Zheng** and Y. Xu, "*Design and optimization of parylene nanomechanical cantilevers with integrated piezoresistors for surface-stress based biochemical sensing*", Microsystem Technologies, accepted.

- **Q. Zheng** and Y. Xu, "*Asymmetric air-spaced cantilevers for vibration energy harvesting*", Smart Materials and Structures, 17 (2008) 055009 (6pp).

- **Q. Zheng**, Z. Wang, and Y. Xu, "*Symmetric air-spaced cantilevers for strain sensing*", Sensors & Actuators: A. Physical, vol 147 pp. 142–149, 2008.

- **Q. Zheng**, Y. Zhang, Y. Lei, J. Song and Y. Xu, "*Haircell-inspired Capacitive Accelerometer with Both High Sensitivity and Broad Dynamic Range*", IEEE Sensors 2010, Waikoloa, HI, USA, Nov. 1~4 2010.

- **Q. Zheng**, H. Tu, A. Agee and Y. Xu, "*Vibration energy harvesting device based on asymmetric air-spaced cantilevers for tire pressure monitoring system*", Power MEMS 2009, Washington DC, USA, Dec. 1~4, 2009.

- **Q. Zheng**, Z. Wang, and Y. Xu, "*Design and optimization of parylene nanomechanical cantilevers with integrated piezoresistors for surface-stress based biochemical sensing*", IEEE-NEMS 2009 (4th), Jan 5-8, Shenzhen, China.